REVIEW OF RAILGUN MODELING TECHNIQUES:
THE COMPUTATION OF RAILGUN FORCE AND OTHER KEY FACTORS

by

NATHAN JAMES ECKERT

A thesis submitted to the

Faculty of the Graduate School of the

University of Colorado in partial fulfillment

of the requirement for the degree of

Master of Science

Department of Aerospace Engineering

2017

This thesis entitled:
Review of Railgun Modeling Techniques:
Computation of Railgun Force and Other Key Factors
written by Nathan James Eckert
has been approved for the Department of Aerospace Engineering

_____
Dr. Kurt Maute, Chair

_____
Dr. Alireza Doostan

Date_____

The final copy of this thesis has been examined by the signatories, and we find that both the content and the form meet acceptable presentation standards of scholarly work in the above mentioned discipline.

Eckert, Nathan James (M.S., Aerospace Engineering)

Review of Railgun Modeling Techniques: Computation of Railgun Force and Other Key Factors

Thesis directed by Professor Kurt Maute

Currently, railgun force modeling either uses the simple "railgun force equation" or finite element methods. It is proposed here that a middle ground exists that does not require the solution of partial differential equations, is more readily implemented than finite element methods, and is more accurate than the traditional force equation. To develop this method, it is necessary to examine the core railgun factors: power supply mechanisms, the distribution of current in the rails and in the projectile which slides between them (called the armature), the magnetic field created by the current flowing through these rails, the inductance gradient (a key factor in simplifying railgun analysis, referred to as L'), the resultant Lorentz force, and the heating which accompanies this action. Common power supply technologies are investigated, and the shape of their current pulses are modeled. The main causes of current concentration are described, and a rudimentary method for computing current distribution in solid rails and a rectangular armature is shown to have promising accuracy with respect to outside finite element results. The magnetic field is modeled with two methods using the Biot-Savart law, and generally good agreement is obtained with respect to finite element methods (5.8% error on average). To get this agreement, a factor of 2 is added to the original formulation after seeing a reliable offset with FEM results. Three inductance gradient calculations are assessed, and though all agree with FEM results, the Kerrisk method and a regression analysis method developed by Murugan et al. (referred to as the LRM here) perform the best. Six railgun force computation methods are investigated, including the traditional railgun force equation, an equation produced by Waindok and Piekielny, and four methods inspired by the work of Xu et al. Overall, good agreement between the models and outside data is found, but each model's accuracy varies significantly between comparisons. Lastly, an approximation of the temperature profile in railgun rails originally presented by McCorkle and Bahder is replicated. In total, this work describes railgun technology and moderately complex railgun modeling methods, but is inconclusive about the presence of a middle-ground modeling method.

Acknowledgments

This work would not have been possible without the input and support provided to me by members of the faculty at the University of Colorado at Boulder. Though the role of the University as a whole is significant, there are some specific people who deserve thanks.

First, I would like to thank my advisor, Professor Kurt Maute for allowing me to pursue this research, and supporting my efforts along the way. The focus of this research is outside the expertise of much of the department, and Dr. Maute very well could have told me to examine something more traditional, or chose not to spend his valuable time supporting this work. I very much appreciate the opportunity he has afforded me to develop this thesis.

Special thanks goes out to Assistant Professor Robert Marshall and Associate Professor Alireza Doostan who have also been instrumental in this work by taking their time to assess this work. In particular, Dr. Marshall has given multiple hours of his time in meetings with me that have undoubtedly improved the quality of this work.

Next I want to thank Professor Hanspeter Schaub, who allowed me to share the use of his ANSYS Maxwell license and improved the quality of the work I was able to perform. Dr Schaub could have easily denied access to ensure his would not have any issues, and I appreciate that he trusted I would work to impose as little as possible on his team's work.

Lastly, I want to thank Dr. Paul Ibanez, my boss and more, for being understanding throughout this research, and providing me with a flexible work environment. Dr. Ibanez also spent a significant amount of his valuable time meeting with me to discuss the finer points of railgun modeling.

Contents

List of Tables

List of Figures

Nomenclature

x, y, z = position of point outside the rail
x', y', z' = position of point inside the rail
l = armature position $[m]$
m = armature mass [kg]
w = rail width $[m]$
h = rail height $[m]$
s = rail separation $[m]$
θ = rail opening angle for circular rails $[m]$
t_h = rail thickness for circular rails $[m]$
w_a = armature width $[m]$
h_a = armature height $[m]$
t_a = armature thickness (size in z direction) $[m]$
I = current $[A]$
I_P = peak current $[A]$
I_t = total current $[A]$
F = Lorentz force on armature $[N]$
V = armature velocity $[m/s]$
t = time [s]
t_1 = current profile rise time $[s]$
t_2 = current profile decline time $[s]$
t_3 = current profile total time $[s]$
t_{rr} = rise time of current in the rails $[s]$
t_{ra} = rise time of current in the armature $[s]$
t_x = time since current began flowing into the conductor $[s]$
f = frequency of a sign wave corresponding to the current rise time in the rail $[Hz]$
f_a = frequency of a sign wave corresponding to the current rise time in the armature $[Hz]$
ω = frequency = $2 \cdot \pi \cdot f$ $[rad]$
τ = capacitor time constant $[s]$
μ = material magnetic permeability $[H/m]$
μ_r = material relative permeability [~]
μ_0 = magnetic permeability of free space = $4\pi \text{x} 10^{-7}$ $[H/m]$
e = material permittivity of the dielectric $[F/m]$
e_0 = permittivity of free space = $8.854 \text{x} 10^{-12}$ $[F/m]$
e_r = material relative permittivity [~]
H = magnetic field intensity $[A/m]$
J = current density $[A/m^2]$
J_0 = current density in the conductor surface
D = electric flux density $[C/m^2]$
E = electric field intensity $[V/m]$
B = magnetic flux density $[Wb/m^2]$
A = magnetic vector potential $[Wb/m]$
Υ = electric scalar potential (voltage) $[V]$
ρ_v = volumetric charge density $[C/m^3]$
σ = material electric conductivity $[S/m]$
k = thermal conductivity $[W/(m \cdot K)]$
c_p = material specific heat
a = distance from current flow to point of interest (r to r') $[m]$
K_e = sawtooth wave to sine wave comparability index, set to 1 [~]
δ_V = skin depth considering VSE $[m]$
δ_{AC} = skin depth of alternating current $[m]$
ρ_r = material resistivity = $1.77 \text{x} 10^{-8}$ $[\Omega \cdot m]$
T = temperature $[K]$
T_0 = initial temperature $[K]$
T_{melt} = material melting temperature $[K]$
(#) = equation number [~]

Chapter 1: Railgun Background

Railguns utilize a pair of conducting rails and a sliding armature, which connects the two rails, to exploit the Lorentz force. Current is sent down one rail, through the armature, and back through the other rail. The current flowing through the parallel rails creates a magnetic field around each rail, and this magnetic field interacts with the current flowing through the armature to create a Lorentz force as shown in Figure 1.

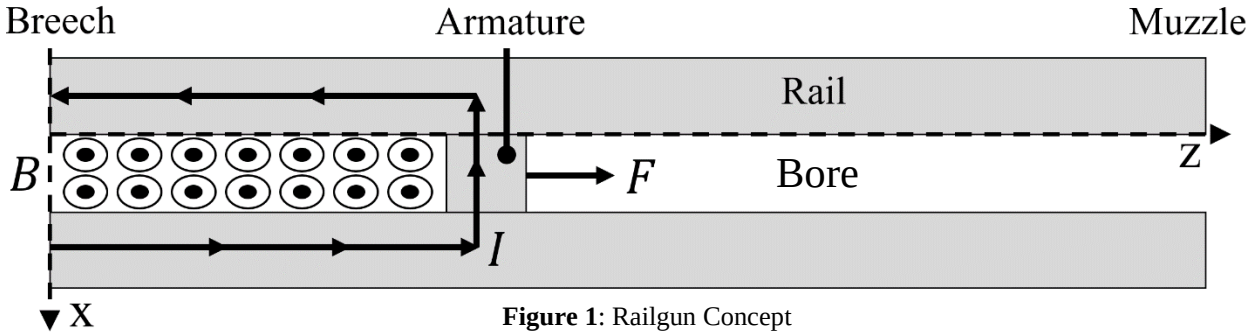

Figure 1: Railgun Concept

Electromagnetic launchers, specifically railguns, are an increasingly popular topic of interest from both military and scientific communities for their ability to accelerate projectiles to high speeds (> 5 km/s) (Poniaev et al. 2016) (Meinel 2007). After being first investigated and constructed in the early 1900's by Kristian Birkeland (Coffo 2011) (Rice et al. 1982), railgun research was declared unlikely to be successful by US Air Force scientists in 1957. However, research was reinvigorated following work by Richard Marshall in 1977, who accelerated a 3g projectile to 5.9 km/s using a 5 m long railgun and a 550 MJ homopolar generator (Meinel 2007). After Marshall's experiment, railguns have been studied by the United States military since before 1984 (D'Aoust et al. 1984), and as a means for space launch by NASA since at least 1982 (Rice et al. 1982) (Turman and Lipinski 1996). Today (since at least 2003) the US Navy has been researching railguns as a shipboard weapon (Lynn et al. 2011) (McFarland and McNab 2003), and interest in railguns as a means for space launch continues (McNab 2003) (Lehmann et al. 2007). In 2005 James Brady examined the use of railguns as infantry weapons. In 2008, and again in 2009, Ian McNab reviewed the work being done by the University of Texas, University of Minnesota, University of New

Orleans, and Texas Tech University on launching a space-bound payload from a high-altitude aircraft. In 2008, NASA examined the use of an electromagnetic launcher to accelerate a scramjet to operating velocity (around Mach 4, or 1.4 km/s at sea level). The scramjet would take a payload to the upper atmosphere, where a small rocket would then launch the payload off of the scramjet, and into orbit (Jayawant 2008). This launcher discussed by NASA is not a railgun, but rather a form of magnetic levitation powered by linear induction motors. Railguns, in their most common form, can produce accelerations in excess of 10,000 gees (Meger et al. 2013) (McFarland and McNab 2003), and it is speculated that because humans and delicate hardware cannot survive this, NASA has selected a less strenuous approach for launch.

For military applications, railguns represent an accurate, low cost, long range weapon that introduces less vulnerability than traditional long range cannons (McFarland and McNab 2003), and have been proposed as shore-barrage cannons and as anti-missile defense weapons. A comparison of conventional guns and proposed European and US shipboard railguns is presented in Table 1 using data from Hudertmark and Lancelle (European) in 2015 and McFarland and McNab (USA) in 2003.

	Proposed USA Railgun	Proposed European Railgun	Modele 68 (French)	Oto-Melara (German)
Range [km]	300 - 500	up to 500	< 17	20-30
Muzzle Velocity [m/s]	2000	2500	870	925
Projectile Mass [kg]	16.4	5	13	5-6
Round Mass [kg]	21.9	8	23	12
Projectile-to-Round Ratio	74.9%	62.5%	56.5%	41.7% - 50%
Rate of Fire [rds/min]	12	~	78	80
Round Cost [$1000]	5-10	~	~	~
Barrel Length [m]	8.77	6.4	5.5	4.72
Bore Size [mm]	146	100	100	76

Table 1: Railgun Performance vs. Conventional Gun Performance (Modele 68 and Oto-Melara) where the USA railgun data comes from McFarland and McNab (2003) and other data comes from Hudertmark and Lancelle (2015)

As shown here, railgun ranges far exceed those of traditional guns due to the vast difference in muzzle velocity. Long range missiles can exceed the listed railgun ranges, but are more expensive. The destructive energy of a railgun round comes from the kinetic impact of a 1-2.5 km/s projectile (McFarland and McNab 2003), instead of an explosive charge, resulting in a cheaper round. The high velocity of a railgun round also reduces travel time, increasing accuracy. In addition, because there is no longer need for

chemical propellant, non-projectile mass and volume can be reduced, though a railgun will require a large power supply. The removal of explosives also makes ships less vulnerable because there is much less explosive material held onboard (McFarland and McNab 2003) (Meger et al. 2013).

With regard to space launch, only the most rigid payloads would be able to survive the launch loads in current railguns. But for these payloads, railguns offer improved predictability, improved efficiency, and reduced cost over rocket launch systems, and would not require the use of environmentally harmful rocket fuel. Rocket performance is inherently reliant on the complex burning of solid fuel, and the complex flow of heated propellant. The complexity of the constitutive processes involved in rocket engine operation, and the number of parts involved, necessitate extensive testing (Freeman 2015). This not only results in high monetary costs, but significantly extends the time needed to provide new rockets. Additionally, rockets are required to lift all needed propellant, meaning much of the energy expended in rocket launch is only needed to lift more fuel. Railguns could be more affordable, as they would require less testing (once developed), and would not need to launch nearly as much non-payload mass. For example, sending 1 kg to low Earth orbit cost around $22,000 with the space shuttle (McNab 2003), $2700 with the more recent Falcon 9, and the expected cost with the Falcon Heavy is $1,700 per kg (SpaceX 2017). Railgun designs have suggested prices could be reduced to around $600 per kg (McNab 2003), and railguns would not require the same large scale that brings down the price per kg in the Falcon Heavy.

Military railguns have very specific size and power requirements, as they are intended to be mounted on ships (Lynn et al. 2011). Research railguns are generally similar, with less focus on size. However, in order to use railguns as a means for space launch, significant changes must be made to standard designs. Primarily, space launch payloads are much more massive (hundreds of kg compared to < 5 kg) and, to achieve ballistic launch into orbit, payloads must accelerate to very high velocities (~7.5 km/s). To keep accelerations reasonably low (~2000 gees) for rigid payloads, the rails would need to be extended from less than 10 m (Hudertmark and Lancelle 2015) (Lehmann 2003) in current railguns to 1500 m or greater (McNab 2003). The transport of humans or other delicate hardware is much more difficult, as

acceleration would need to reduce to ~3 gees, meaning the minimum rail length needed to accelerate to 7.5 km/s is 937.5 km.

Inspired by the active interest in the field of electromagnetic launchers, this work examines the presence of railgun modeling methods which are reasonably accurate but do not require the solution of partial differential equations or the use of finite element methods. Such methods would assist in simpler computation of medium-fidelity models, and design space exploration. Simple, reasonably accurate methods of computing current profiles and inductance gradient values already exist, and are applied and examined here. No readily applicable method of defining current distribution has been found, so the principles of current flow are defined, and a rudimentary method is proposed. A method for defining the magnetic field in the armature has been mentioned by Xu and Geng (2010) but has not been explored at length, so two versions of this method are compared to finite element results to determine accuracy. Two readily applicable force equations exist: the traditional "railgun force equation", and one defined by Waindok and Piekielny (2016). This examination looks at the accuracy of these methods by comparing them to four versions of a force equation defined by Xu and Geng (2010), finite element methods, and experimental methods to determine if accuracy improvements can be obtained by a more detailed analysis. Lastly, a method for computing temperature in the rails proposed by McCorkle and Bahder (2010) is replicated to confirm its operation. In these models, only solid, rectangular armatures are considered, so significant adjustments may be necessary to account for plasma or brush armatures and different rail / armature geometries. The examination of these methods informs decisions on their accuracy, and assists in preliminary railgun modeling. Using methods which do not require the solution of partial differential equations (and are all implemented with MATLAB here) opens the door for analysis by investigators with little railgun experience. Also aiding in this goal is an overview of the main factors important to railgun operation, and an introduction to the analysis of these factors presented here.

Chapter 2: Power Supply Mechanisms

To model nearly all railgun factors, it is necessary to know the applied excitation current. For transient analyses, the time dependence of this current must be defined. This section focuses on this definition, and presents a commonly used model for approximating current profiles. Though most railgun power supplies provide similar current pulses, railgun power supply technologies are also described here to provide background.

Railgun power supplies must be able to provide pulses of high current over a few ms (around 1 to 15 ms) (Chengxue et al. 2014) (Waindok and Piekielny 2016) (Stefani et al. 2007) (Coffo 2011) (D'Aoust et al. 1984) (Murugan, Kumar, and Raj 2016). Many pulsed power systems exist, though the most popular for this application are Pulse Forming Networks (PFN's) with capacitors and rotating machines (pulsed homopolar generators, rectified pulsed alternators, and compulsators) (McNab 1997) (Lynn et al. 2011) (McNab 2003) (McFarland and McNab 2003) (D'Aoust et al. 1984) (Meger et al. 2013). As discussed by McNab (2014), other possible techniques include flux compressors (Goldman et al. 1999) (Li et al. 2004), magnetohydrodynamic (MHD) generators (Ying et al. 2004), and pulsed inductors (Sitzman et al. 2006) (Liang et al. 2016) (Meger et al. 2013). Despite the many options for pulsed power, Richard Marshall (the head of the team responsible for reinvigorating railgun research in the late 1970's) said in a 2001 article that power supplies constitute the most concerning barrier to further railgun development.

The simplest railgun power source would be a single large capacitor, as capacitors are inherently good at providing large current pulses over short periods of time. However, even if a very large single capacitor (or single capacitor bank) is used, current is only supplied for a very short amount of time without further power conditioning, and the amount of force provided would be too small. For example, a hypothetical capacitor capable of supplying 300 kA with a time constant (τ) of 0.5 ms would only produce current above 270 kA for 0.2 ms (obtained with the traditional discharging capacitor equation). To obtain more time at high current, and somewhat decrease the need for exceptionally high current pulses, networks of energy storage devices are used, where the storage devices are linked with inductors in a Pulse Forming

Network (PFN) to spread out the current pulse. Though the most common storage devices are capacitors, other forms of energy storage can be used such as transmission lines, inductors (Haddad and Warne 2004), or rotating machines (Lynn et al. 2011). An example of a relatively simple PFN using capacitors can be seen in Figure 2 from Gully et al. who sought to minimize PFN weight (Gully et al. 1993).

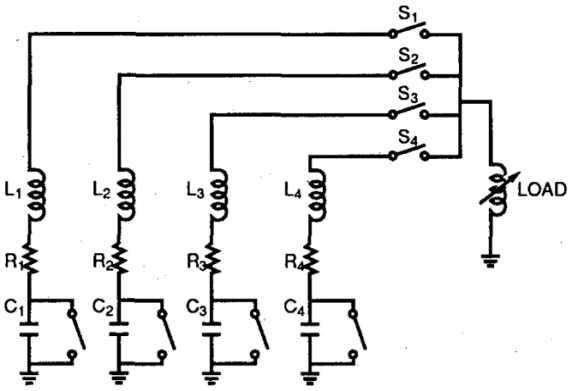

Figure 2: Pulse forming network schematic (Gully et al. 1993)

Despite the various available options for railgun power supplies, a common current profile is used in the literature. Generally, the current profile is defined by a rapid rise – constant – slow set behavior (Xu and Geng 2010), though it is not uncommon for researchers to simply assume constant current (McCorkle and Bahder 2010), as most current (and thus force) flows in the "constant" section.

The current rise is sometimes modeled with a linear increase (Chengxue et al. 2014) (Jin et al. 2015) (Murugan, Kumar, and Raj 2016), but is more accurately modeled as the first quarter of a sign wave, as described by (1) where the harmonic frequency (ω) is defined by the rise time (t_1), as shown in) (Xu and Geng 2010). This rapid increase mirrors the description of AC current profiles, and becomes responsible for skin effects present in the rails, as discussed more in the current distribution chapter. The second, "constant" section is simply described by (2), and the last "slow set" section is described by an exponential decay in (3).

(1) $$I = I_0 \cdot sin(\omega \cdot t) = I_0 \cdot sin\left(\frac{\pi}{2\,t_1} \cdot t\right) \qquad (0 \le t \le t_1)$$

(2) $$I \approx I_0 \qquad (t_1 \le t \le t_2)$$

(3) $$I = I_0 \cdot e^{-t/\tau} \qquad (t_2 \le t \le t_3)$$

(4) $$\omega = 2\pi \cdot f \quad where \quad f = \frac{1}{4\,t_1} \rightarrow \omega = \frac{\pi}{2\,t_1}$$

Profiles using (1) and (3) which do not assume a constant current section are shown in Figure 3 and Figure 4 to demonstrate the benefits of PFNs. The definitions of t_1, t_2 and t_3 are also shown in Figure 3 (b).

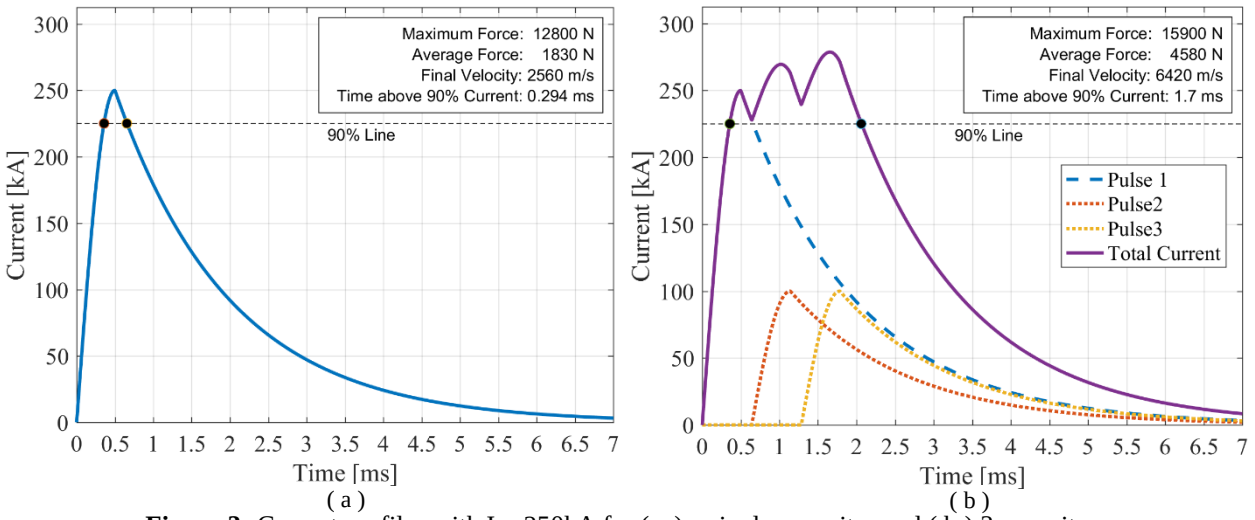

(a) (b)

Figure 3: Current profiles with I = 250kA for (a) a single capacitor and (b) 3 capacitors

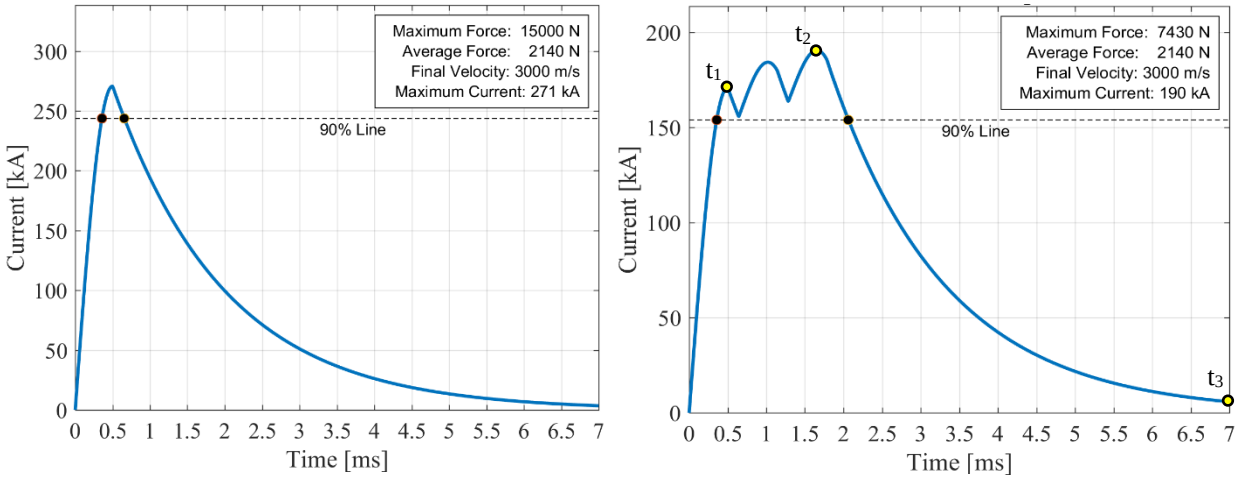

(a) (b)

Figure 4: Current profiles of railguns that will accelerate projectiles to 3 km/s with (a) a single capacitor and (b) 3 capacitors

As shown in with Figure 3 and Figure 4, it takes a larger single capacitor to provide the necessary force, and the peak current is much higher. Figure 3 shows the current profile for a single pulse (a), and 3 sequenced pulses (b). It can be seen that the velocity, and the time at high current is substantially increased in the profile with multiple pulses.

The force and velocity for each profile is found using the railgun force equation (5) and assumes a maximum current of 250 kA, an L' of 0.41 μH/m, and a projectile mass of 5 g.

(5) $$\mathrm{F} = \frac{L' \cdot I(t)^2}{2}$$

The "90% line" is found by comparing the provided current with the maximum current of the first, larger capacitor. In the hypothetical group of sequenced capacitors used here, the first capacitor provides 250 kA and the latter ones provide 100 kA. It is not surprising that more capacitors yield more velocity, but the particular advantage of a PFN can be seen with Figure 3. In the first profile (a) a projectile is accelerated to 3 km/s with a single capacitor using a peak current of 270.6 kA. In (b) the projectile is accelerated to 3 km/s with 3 capacitors using currents of 170.9 kA, 68.36 kA, and 68.36 kA. Therefore, a single capacitor needs to reach a much higher current to accelerate its projectile to 3000 m/s. Higher current spikes mean more issues with temperature rise, and this short acceleration time means the payload is subject to much higher launch loads. Additionally, the temperature increases that come with higher current spikes cause the railgun resistance to increase as well, meaning the disparity between PFN's and individual capacitors would be greater if this effect was considered, and the single capacitor profile would be less efficient.

Three experimental current profiles are provided in Figure 5 on the following page for qualitative comparison (Meger et al. 2013) (Lehmann et al. 2007) (Schneider et al. 2009 pt.2) (Stefani et al. 2007). It can be seen that the average current in the "constant" section is relatively constant in (a), (b), and (d), but there are still significant departures from constant current in (b) and (c). The assumption of constant current remains an idealization, but it does have empirical backing.

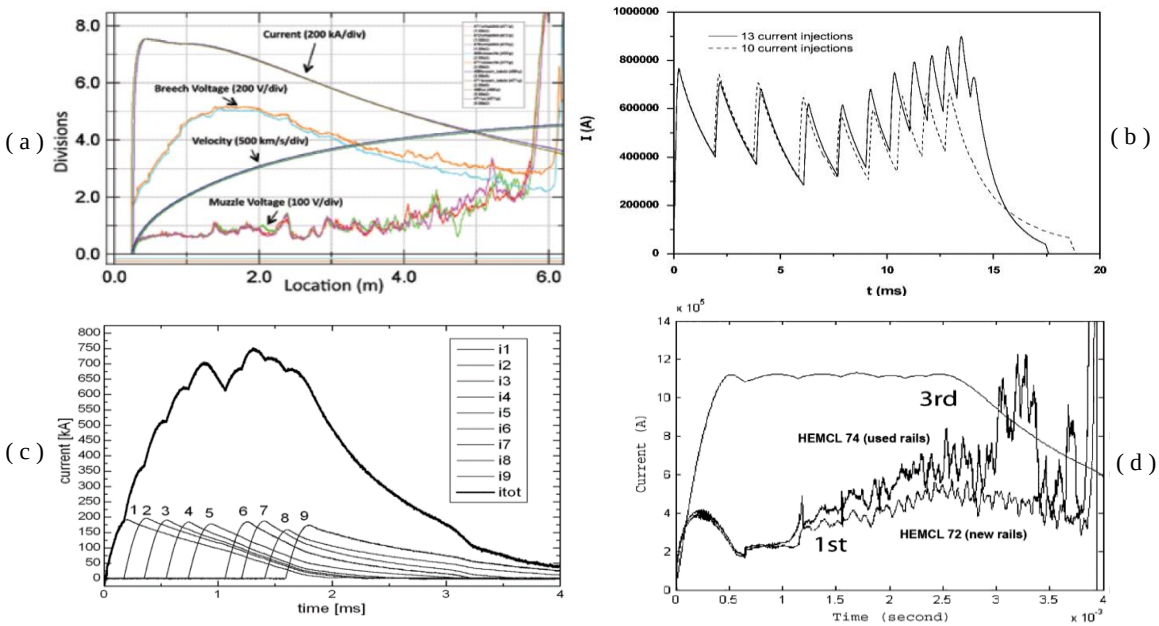

Figure 5: Experimental current profiles supplied by (a) power supplied to the railgun at MTF using 22 capacitor banks with 500kJ capacity each (Meger et al. 2013) (b) power supplied to the PEGASUS railgun at ISL using a capacitor bank of 200 modules with a capacity of 50kJ each (Lehmann et al. 2007) (c) power supplied to the RAFIRA railgun at ISL using 9 of 20 available capacitor banks (Schneider et al. 2009 pt.2) (d) power supplied to the HEMCL railgun at IAT, power supply consists of 18 banks of 24 capacitors each (Stefani et al. 2007) (Watt 2011)

2.1 Capacitor Banks

Capacitor banks have been the most common railgun power source, as the technology is well developed, reliable, and relatively simple (Meinel 2007) (McNab 1997) (Lynn et al. 2011) (McNab 2003) (McFarland and McNab 2003) (D'Aoust et al. 1984) (Meger et al. 2013) (Lehmann et al. 2007). The PFN that powers the PEGASUS railgun installed at the Institute of Saint-Louis (ISL) utilizes capacitor banks to provide a current pulse around 600 kA for nearly 15 ms (Figure 5 (b) and Figure 6) (Lehmann et al. 2007) (Spahn and Buderer 1999). Individually, simple capacitor banks still provide relatively short current pulses. It is only with the addition of power conditioning through inductors and crowbar diodes that these extended pulses can be obtained.

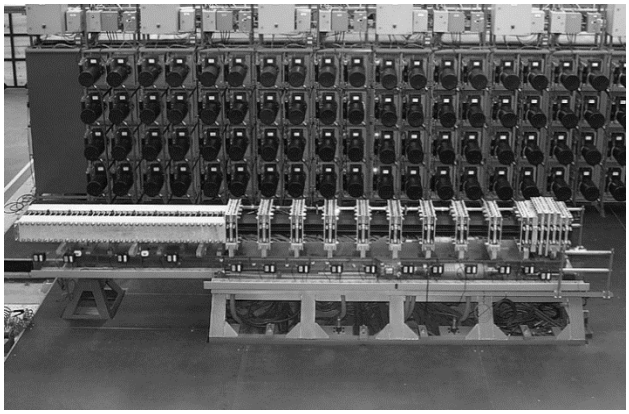

Figure 6: The PEGASUS railgun at ISL and part of the capacitor bank that powers it (Lehmann et al. 2007)

Capacitor banks can be modular (Baker et al. 1989), and therefore allow for relatively simple maintenance when needed. But the ability to adjust their operation without adding or replacing components is very limited in comparison to other systems (Gao et al. 2015). Due to the number of relatively large physical components needed to network capacitors, banks are generally heavy and physically large (low energy density) compared to other energy storage methods, though work to reduce capacitor bank size is ongoing (Liu et al. 2011). This is the main reason capacitor banks are not the favored choice for military shipboard systems, despite the fact that they are static and thus do not produce large torques like rotating machines (McFarland and McNab 2003)**.** However, mass and volume are less of a concern for research laboratories and prospective space launch systems, making capacitor banks the preferred choice for many stationary railgun systems.

2.2 Rotating Machines

In early railguns, the rotating machines used were homopolar generators (HPGs) (Marshall 2001). HPGs, once started with an excitation current (usually provided by an inductor), rotate a conductive disk in a magnetic field, producing a Lorentz force pointed toward the edge of the spinning disk. The current produced from the rotating disk is collected withh brushes (sliding contact) around the disk edge. This method allows large currents to be generated for short periods. However, according to McNab (2014) HPGs have inherent issues with:

- Wear and maintenance due to a reliance on sliding contacts
- Providing for multiple shot operation due to switching difficulties
- Obtaining high energy density due to tip speed limits from the use of ferromagnetic materials

Attention then switched in the 1990s and 2000s to rectified pulsed alternators, especially for military applications (McFarland and McNab 2003) (Gao et al. 2015) (Meger et al. 2013) (Walls et al. 1997). Pulsed alternators use excited rotor windings on the face of the rotating mass to excite stator windings, which then deliver output power. The alternator pulse width is small compared to that needed by railguns, so multiple

smaller pulses are delivered, resulting in a similar current profile to PFNs using capacitors (Figure 7). A variant of pulsed alternators uses winding compensation to reduce impedance and increase output current. These are commonly referred to as compulsators, and have been under ongoing research for over 30 years (Gao et al. 2015) (Pratap et al. 1984) (Gully 1991) (Pratap and Driga 1999) (Marshall 2001). The main advantage of pulsed alternators is that they operate with lower current, allowing multiple windings and thus multiple poles, which enables higher voltage power than HPG's. Other advantages include a freedom from sliding contacts, the ability to store and deliver energy for multiple shots, and a deep history of research due to the similarity to synchronous AC generators used by utility companies. A list given by McNab (2014) describes the remaining issues with pulsed alternators as being:

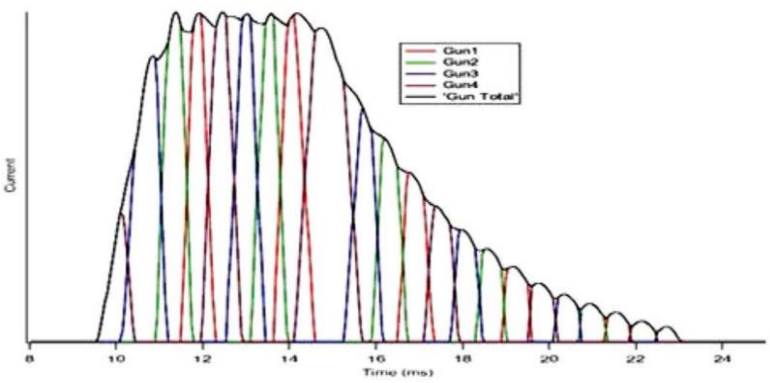

Figure 7: Compulsator current profile (McNab 2014)

- manufacturing complexity introduced by the need for tight tolerances
- thermal management in the rotor windings
- output pulse rectification due to their inherent AC nature
- the size and capacity of switching and control devices
- multimachine synchronization
- efficiency
- cost

Additionally, as reported by Pratap et al, electrical forces in compulsator rotor windings attempt to peel the winding from the rotor surface, adding to the structural and material demands on the rotor (Pratap and Driga 1999). Even though issues with cost and efficiency are likely not specific to pulsed alternators, a suggestion

by McNab, and recent research by Engel et al. suggests that interest may be returning to HPG research (Marshall 2001) (Pratap and Driga 1999) (McNab 2014).

Advantages with rotating machines in general, in addition to their previously mentioned energy density, consist of flexibility (Gao et al. 2015) and longer life expectancies (Hebner et al. 2006). General disadvantages with rotating machines are that they produce an external torque when discharging, meaning they must be used in pairs on ship-board railguns and they are much more mechanically complex than capacitor systems. If maintenance is required, the whole generator has to be shut down or replaced, unlike capacitor systems. Lastly, the usage of kinetic energy storage (large flywheels spinning at thousands of RPM) introduces some risk for ship-based systems in the event of attack.

Chapter 3: Current Distribution

With the supply current defined, it is then necessary to examine how current distributes in the rail and armature. This is important as current concentrations create excessive heating and the current distribution partially dictates the railgun force. Heating is problematic since it increases electrical resistance and causes rail damage. The Lorentz force depends on the interaction of current and magnetic field, so maximizing force relies on regions of high current coinciding with regions of high magnetic field. The work in this chapter describes the main principles of current distribution relevant to railguns, and presents a rudimentary method to estimate it for railguns with solid rails and rectangular armatures.

Current distribution is one of the most complex analyses necessary for describing railgun operation since it is entirely dependent on the solution of partial differential equations. The relevant equations for this analysis are Maxwell's equations (6) → (8) along with the charge continuity equation (10), five constitutive equations (11) → (15), and the relations of (16) and (17) (Zhao et al. 2014). As shown by Zhao et al. (2014), current density can be described by (18) → (20) where (19) and (20) must be solved simultaneously.

(6) $\nabla\times\mathbf{H} = \mathbf{J} + \frac{\partial \mathbf{D}}{\partial \mathrm{t}}$

(7) $\nabla\times\mathbf{E} = -\frac{\partial \mathbf{B}}{\partial \mathrm{t}}$

(8) $\nabla \cdot \boldsymbol{D} = \rho_V$

(9) $\nabla \cdot \boldsymbol{B} = 0$

(10) $\nabla \cdot \boldsymbol{J} = -\frac{\partial \rho_V}{\partial t}$

(11) $\boldsymbol{B} = \mu \boldsymbol{H}$

(12) $\boldsymbol{D} = \varepsilon \boldsymbol{E}$

(13) $\boldsymbol{J} = \sigma \boldsymbol{E}$

(14) $\mu = \mu_0 \mu_r$

(15) $\varepsilon = \varepsilon_0 \varepsilon_r$

(16) $\boldsymbol{E} = -\nabla\Upsilon - \frac{\partial \boldsymbol{A}}{\partial \mathrm{t}}$

(17) $\boldsymbol{B} = \nabla \times \boldsymbol{A}$

(18) $\boldsymbol{J} = \sigma\left(-\nabla\Upsilon - \frac{\partial \boldsymbol{A}}{\partial \mathrm{t}}\right)$

(19) $\sigma\frac{\partial \boldsymbol{A}}{\partial \mathrm{t}} + \frac{1}{\mu_0}[\nabla\times(\nabla\times\mathbf{A})\,] + \sigma\nabla\Upsilon = 0$

(20) $\nabla \cdot (\sigma\nabla\Upsilon) = 0$

(21) $\nabla \cdot \left(\sigma\nabla\Upsilon + \sigma\frac{\partial \boldsymbol{A}}{\partial \mathrm{t}}\right) = 0$

The formulation used by Zhao et al. assumes the following:

- All materials are isotropic and non-ferromagnetic
    - As a result, the relative magnetic permeability (μ_R) for all materials is 1. This assumption is reasonable because most railguns are composed mainly of copper rails and an aluminum armature, both of which have a relative permeability close to 1.
- Quasi-static operation
    - This allows the displacement current term $\left(\frac{\partial \boldsymbol{D}}{\partial t}\right)$ to be neglected in (6), as has been done before in railgun analysis (Kerrisk 1982)
- The change in magnetic vector potential $\left(\frac{\partial \boldsymbol{A}}{\partial \mathrm{t}}\right)$ from (16) is 0 when deriving (20**)**.
    - If this assumption is not made, (13) and (16) can be combined with a finding by Zhao et al. that $\frac{\partial \rho_V}{\partial \mathrm{t}} = 0$ can be written, giving $\nabla \cdot \mathbf{J} = 0$. In this case, (20**)** would look like (21).

Equations (18) → (20) were defined utilizing these assumptions. It is now necessary to explore the nuances and consequences of rail current distribution.

Areas of high current density are of particular interest in railgun design, as these areas are prone to excessive Joule heating and dictate the magnetic field shape. In simple railgun operation, the vast majority of the current flows through a thin layer near the rail surface. This is due to five main factors. Of these, the skin effect of alternating current and proximity effect are commonly present in stationary conductors with AC power. Much of the following description is compiled from the work of Lv et al. (2014) from the Chinese Shijiazhuang Mechanical Engineering College.

- Clustering Near Small Source of Constant Current (CNSS) (Lv et al. 2014)
- Clustering Along Short Path of Constant Current (CASP) (Lv et al. 2014)
- Proximity Effect (Lou et al. 2016)
- Skin Effect of Alternating Current (SAC) (Lv et al. 2014)
- Velocity Skin Effect (VSE) (Lv et al. 2014) (Lou et al. 2016)

These factors are described below, as many railguns use the "simple railgun" design with solid rails. However, much of the concern with current distribution in rails has been solved by using laminated rails, which use thin strips of rail material separated by dielectric. Using thin strips reduces the impact of the skin effect, since the whole strip cross-section is essentially "skin". This means that approximating the current distribution as uniform is reasonably accurate for laminated rails (Xu and Geng 2010) (Xing et al. 2015). Thus, the bulk of this analysis assumes a uniform current distribution in the rails, though it is true that near the armature, current will still concentrate along the rail inner face.

3.1 Clustering Near Small Source (CNSS)

The first of these (CNSS) simply acknowledges that, when a current spot source / spot sink exists, current concentrates around this point. The relationship of current density ($\boldsymbol{J}$) to position around this spot is described by (22), whereas the relationship around a line-like source is described by (23):

(22) $$J(r) \propto \frac{J_0}{r^2}$$ (23) $$J(r) \propto \frac{J_0}{r}$$

Here, r is the distance from the spot, and J_0 is the current density in the spot source or sink. This effect is most relevant to the current density in the armature and rail along the contact surface. On a large and medium scale, the rail can be thought of as a line-source, and the vertical trailing edge of the armature can be thought of as a line-sink (due to CASP). On a small scale, regions of actual contact between rail and armature can be thought of as spot sources (Figure 8). The presence of these current concentrations serve to exacerbate issues of armature heating, rail wear, and transition.

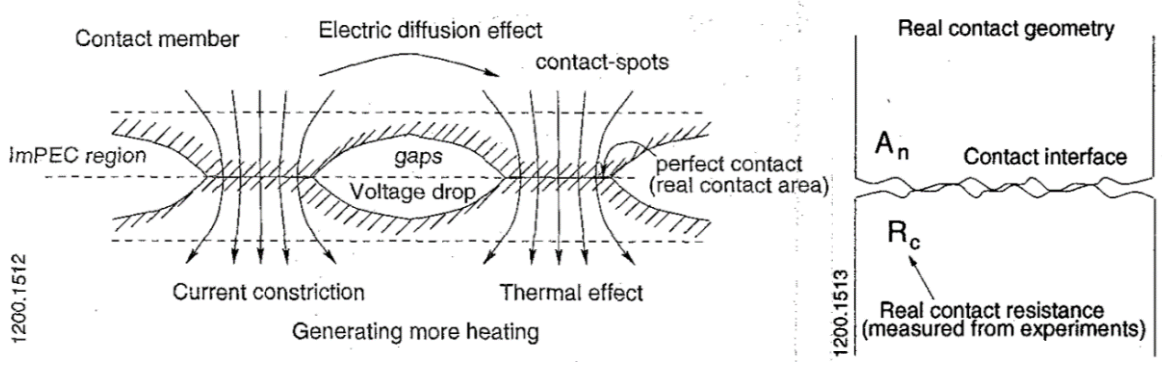

Figure 8: Current flow through imperfect electrical contact (Kim, Hsieh, and Bostick 1999)

3.2 Clustering Along Short Path (CASP)

The second effect (CASP) describes the fact that current will concentrate along the shortest path between high and low voltage locations. This effect can be recognized easily with (24), where a reduction in path length ($\int dl$) will result in an increase in current density ($\boldsymbol{J}$) for a given voltage.

(24) $$\Upsilon = \int \rho \cdot \boldsymbol{J} \; dl$$

It should be noted that, in a railgun application, (24) will use different densities to account for the different material in rail and armature. In the simple railgun, this effect causes the current to concentrate along planes 2, 4, and 6, as shown in Figure 9.

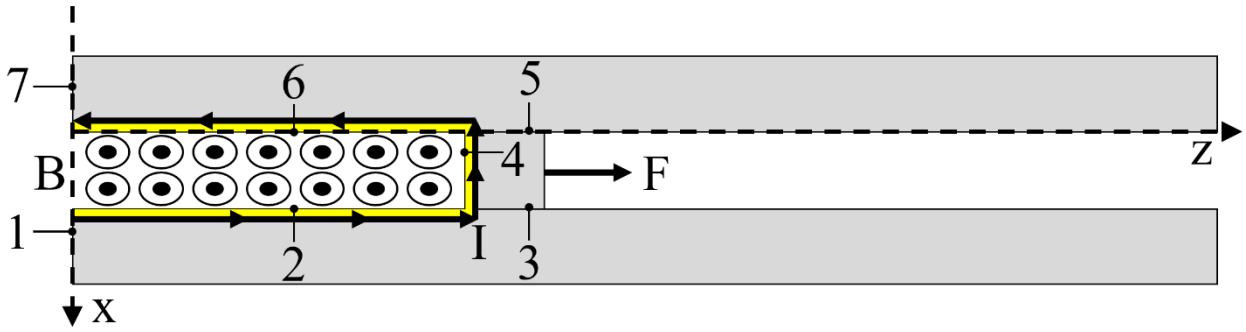

Figure 9: Railgun concept considering CASP with planes 1 → 7 defined for reference

3.3 Proximity Effect

The proximity effect, as described by Pagnetti et al., is generated by current-carrying conductors being nearby (within distances that are on the order of the conductor radius). A conductor in this case will induce eddy currents that alter the internal impedance of nearby conductors, resulting in current concentration on the side of the responsible conductor. (Pagnetti et al. 2011) The proximity effect was studied in railguns in 2016 by Lou et al. and, like the skin effect, depends on frequency (rise speed). The proximity effect (as its name suggests) is dependent on the rail separation (s). A decrease in s will increase the effect, and an increase in s will make the effect fall off. The proximity effect was shown to be invariant with changes in current amplitude. There is not yet any simplified analytical method to quantify this effect, but analysis with the partial differential equations listed above will inherently consider it. (Lou et al. 2016) The result of these findings is an additional motivation to keep railgun rails at a healthy distance from each

other, as this will reduce current concentration. Increasing rail separation also yields improvements in L', resistance, and rail stress (Lou et al. 2016) (Keshtkar 2005) (Xu and Geng 2010).

3.4 Skin Effect of Alternating Current (SAC)

The fourth effect, commonly called the skin effect, becomes significant when rapidly changing current (usually in alternating current applications) is applied to a conductor. In such cases, the current concentrates around the conductor surface (Thomas and Meadows 1985). Though railguns operate on DC power, the rapid rise of the current pulse (from $t = 0$ to $t = t_1$ in Figure 3 (b)) induces the same effect. In fact, Lv et al. argue that the amount of current in the rail center is negligible, and therefore use an equivalent hollow rail to perform their analysis (Lv et al. 2014) to model the skin effect without using a transient finite element solution.

The current distribution in a large conducting plane is described by (25), which can be broadly simplified to (26). Both equations depend on the AC skin depth, which has many equivalent definitions. Three of these are shown in (27).

(25) $$J = J_0 \cdot e^{\left(\frac{-x'}{\delta_{AC}}\right)} \cdot e^{J \cdot \left(\frac{x'}{\delta_{AC}} - \omega \cdot t_{rr}\right)}$$

(26) $$J = J_0 \cdot e^{\left(\frac{-x'}{\delta_{AC}}\right)}$$

(27) $$\delta_{AC} = \sqrt{\frac{2 \cdot \rho_r}{\omega \cdot \mu}} = \sqrt{\frac{\rho_r}{\pi \cdot f_r \cdot \mu}} = \sqrt{\frac{4 \cdot t_x}{\sigma \cdot \mu_0}}$$

$where\ x' = 0\ at\ the\ conductor\ surface\ here\ and$

$e^{J \cdot \left(\frac{x'}{\delta_{AC}} - \omega \cdot t\right)}$ = electromagnetic fluctuation coefficient

$e^{\left(\frac{-x'}{\delta_{AC}}\right)}$ = damping coefficient

Each of these equations assume that the current flows through a good conductor, which applies for copper and aluminum. This skin effect is responsible for a significant amount of the current concentration that produces melting in the armature and solid rails. It also seems to be responsible for the greatest current concentration being at the top and bottom of the rail inner surface (shown in Figure 10 and Figure 11), as the shortest path for the current flowing along the top, bottom, and outer surfaces is through these corners.

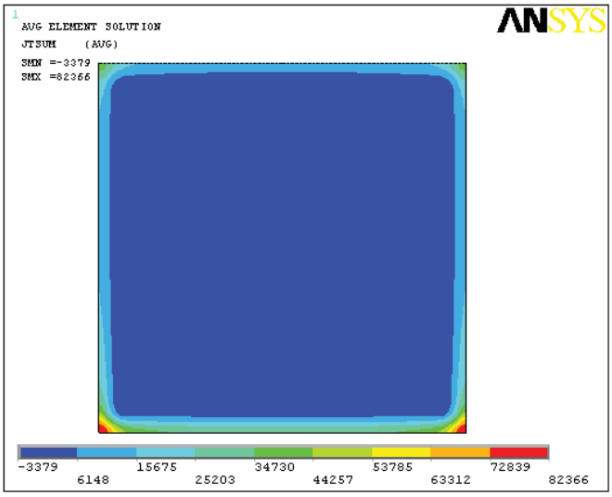

Figure 10: Current distribution in rail (armature-rail interface shown on bottom) as computed by Bayati et al. (2013)

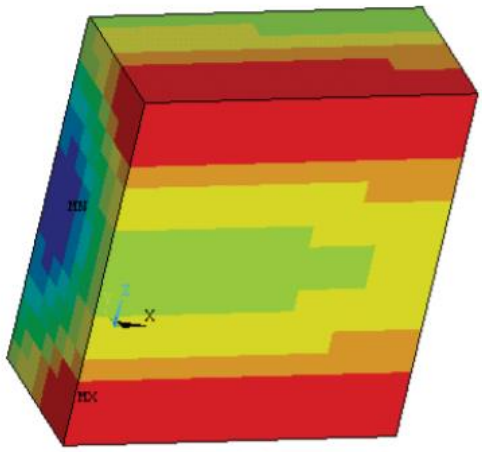

Figure 11: Current distribution in rail (armature-rail interface shown in front, armature travel direction shown as left to right) as computed by Zuo et al. (2013)

3.5 Velocity Skin Effect (VSE)

The velocity skin effect is well described by simulation results from Long et al. (Long and Weldon 1989), shown in Figure 12, where the contour lines shown describe the percentage of total system current.

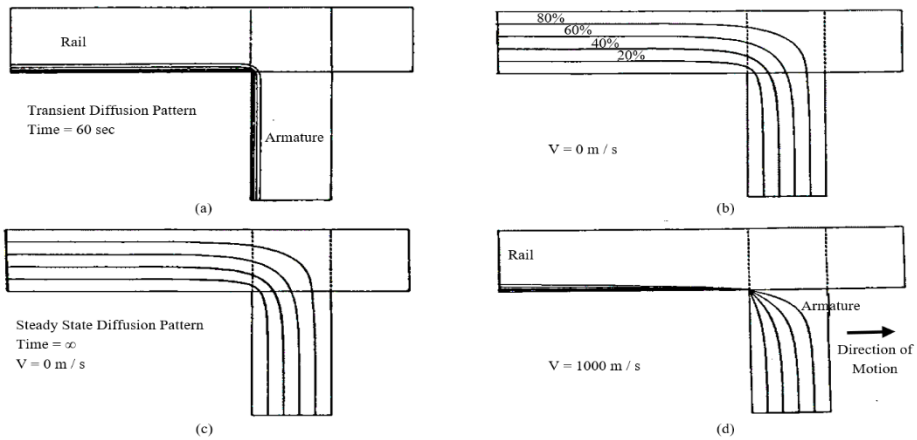

Figure 12: Current concentration due to velocity skin effect (Long and Weldon 1989) contour lines describe percentage of total current

It can be seen from (a) and (c) that, if the armature is held in position, the current will eventually diffuse throughout the conductors. The time necessary for this to happen is directly dependent on the material's magnetic permeability, electrical conductivity, and the length of the diffusion distance (Long and Weldon 1989). As the armature begins to travel, current is passing through sections of rail that have not been exposed to current flow. This means that current does not have time to diffuse into a new arbitrary rail section, and current then concentrates on the surface of the rail at the trailing edge of the armature, as shown in (d).

Even if the velocity had no impact, a railgun shot lasts far less than a second, (commonly ~5 ms) and the current would not have enough time to diffuse throughout the rail as shown in Figure 12 (a). Regardless, this effect remains significant in railguns because current concentrates more highly in faster railguns, and concentrates less in slower ones (Lv et al. 2014).

An analytical description of this effect can be obtained by modifying (25) → (27) used for assessing skin effect. At the base of the rails (planes 1 and 7 from Figure 9), the frequency (f_a) can be found by considering the rise time (t_1) as one fourth of the period, giving $f_a = \frac{1}{4*t_0}$. In an arbitrary rail section, the frequency has been described by the same general formula, but with the time given by $\Delta t = \frac{t_a}{V}$ where t_a is the length (or thickness) of the armature contact interface (planes 3 and 5) and V is the armature velocity. The equation for time is obtained with the knowledge that the current density in an arbitrary rail section increases from 0 to J_{max} in the time it takes the armature to pass the rail section (Lv et al. 2014). In reality, because of CASP, most of the current flows through the trailing armature face (plane 4), so the majority of this increase from 0 to J_{max} happens when the last portion of the armature passes the rail section. Thus, a more accurate computation of frequency would come from defining an equivalent rise time that accounts for this exponential behavior. This computation is not performed here, but a factor of $\frac{1}{2}$ is applied because it is safe to say that the vast majority of the current flows through the trailing half of the armature.

The final Δt and f_a equations are therefore given by (28) and (29), and the velocity skin depth (the depth into the conductor that current flows) is given by (30).

(28) $$\Delta t = \frac{L_a}{2 \cdot V}$$

(29) $$f_a = \frac{1}{4 \cdot \Delta t} = \frac{V}{2 \cdot L_a}$$

(30) $$\delta_V = k_e \cdot \sqrt{\frac{4 \cdot \rho_r \cdot t_{ra}}{\pi \cdot \mu \cdot V}} = k_e \cdot \sqrt{\frac{2 \cdot \rho_r}{\pi \cdot \mu \cdot f_a}}$$

An additional approximation made by Lv et al. assumes the period resulting from a linear increase (equivalent to one quarter of a sawtooth wave period) can approximate the period of a sine wave. A comparability index (k_e) is used to describe this, but is set to unity. It can be seen from (30) and (27) that if the current rises faster, the skin depth will decrease, meaning the current is more concentrated, and thus produces more local Joule heating.

3.6 Current Distribution Approximation (CStSM)

For this analysis, current distribution in the rails is assumed to be uniform due to the advent of laminated rails. Regardless, a rudimentary method for computing current distribution in solid rails and the armature is presented. This approximation is obtained by computing a distribution that is shaped roughly correctly, then scaled to represent the correct quantity of current. This method will be called the CStSM (Current Shape then Scale Method) for the purposes of this paper.

The shape is defined using the skin depth and current density equations ((26), (27), and (30)) at each point in the rail or armature. In the rails, this results in (31)**.**

(31) $$\boldsymbol{J}_{i\,j} = e^{\left(\frac{-x_i'}{\delta_{AC}}\right)} + e^{\left(\frac{-y_j'}{\delta_{AC}}\right)}$$

J_0 is defined as 1 here because the magnitude will be defined later when the result is scaled.

In the armature, the current will only concentrate along the rear face (as dictated by CASP), and thus the shape is defined by (32).

(32) $$\boldsymbol{J}_{j\,k} = e^{\left(\frac{-(z_k - l)}{\delta_{AC}}\right)}$$

Now that the shape is defined (in a 2D matrix for the rail, and a 3D matrix that is uniform in the x and y directions for the armature), the scaling factor (S) must be computed. This is done with the knowledge that some total amount of current (I_t) is flowing through any given area of interest, and the current density must reflect this. First, the total amount of current predicted initially (I_{in}) must be found with (33) for the rail or (34) for the armature, then the ratio of the total current to the initially predicted current $\left({}^{I_t}/_{I_i}\right)$ defines the scaling factor.

(33) $$I_{in} = \sum_{i=1}^{m} \sum_{j=1}^{n} \left(\boldsymbol{J}_{i\,j} \cdot dx \cdot dy \right)$$

(34) $$I_{in} = \sum_{j=1}^{n} \sum_{k=1}^{p} \left(\boldsymbol{J}_{j\,k} \cdot dy' \cdot dz' \right)$$

Where $dx, dy,$ and dz are the rail grid element width, height, and depth respectively, and dx', dy', dz' are the armature grid sizes and x and y are 0 at the conductor surface.

The final current distribution is found by simply multiplying the current density by this scaling factor. In these equations, the indices i, j, and k correspond to the x, y, and z directions. Similarly, the total number of points in the x, y, and z directions are m, n, and p.

(35) $$S = \frac{I_t}{I_{in}}$$

3.7 CStSM Comparison

This method was applied to the case used by Lv et al. (2014) to assess its accuracy. The details of this comparison case are shown in Table 2:

Physical Parameters	Symbol	Value	Value	Symbol	Electrical Parameters
Rail Length [m]	L	~	500	I_P	**Peak Current [kA]**
Rail Separation [m]	s	0.04	0.05	t_1	**Current Profile Rise Time [ms]**
Rail Width [m]	w	0.01	0.05	t_2	**Current Profile Decline Time [ms]**
Rail Height [m]	h	0.04	0.1	t_3	**Current Profile Total Time [ms]**
Inductance Gradient [μH/m]	L'	0.5279	Value	Symbol	Material Parameters
Armature Width [m]	w_a	0.04	Cu	~	**Rail Material [~]**
Armature Height [m]	h_a	0.03	Al	~	**Armature Material [~]**
Armature Thickness [m]	t_a	0.02	$4 E^{-8}$	ρ_r	**Armature Resistivity [Ω·m]**
Armature Velocity [m/s]	V	400	$1.77E^{-8}$	ρ_r	**Rail Resistivity [Ω·m]**

Table 2: Railgun parameters used by Lv et al. (Lv et al. 2014). L' was calculated, not sourced directly

Lv et al. performed their analysis using ANSYS Maxwell 14.0 and a mesh with a maximum element dimension of 2 mm. Two comparisons are made; one for the armature and one for the rail current density.

The armature comparison shows reasonably good agreement between the two results, with some obvious caveats. The approximation made here does not consider any variation in current density along the armature height. This has two consequences. First, the CStSM results do not show higher current density along the top and bottom edges like the ANSYS results do. Second, the peaks at the top and bottom corners are not replicated since the density is not compounded by concentration at multiple edges. This also means the maximum J in the ANSYS result is higher than in the CStSM result. Regardless, the average current density along the armature rear face (left of Figure 13 (b) and Figure 14 (b) on the following page) is ~$1.2\text{x}10^{10}\left[{}^{A}/_{m^2}\right]$ in the ANSYS result and ~$1\text{x}10^{10}\left[{}^{A}/_{m^2}\right]$ in the CStSM result, giving the CStSM an error of about -16.67% relative to ANSYS. The falloff looks to happen slightly more quickly with the CStSM than ANSYS.

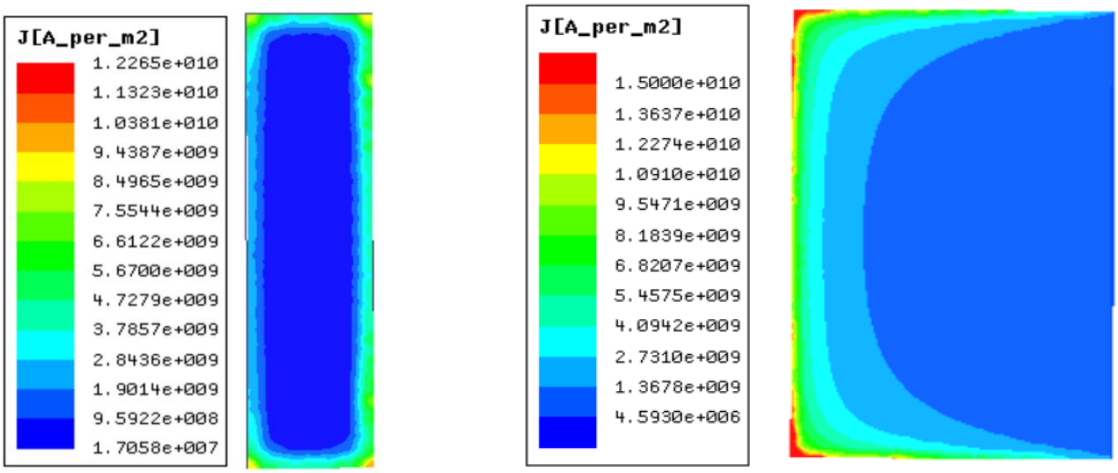

(a) (b)

Figure 13: Current distribution in (a) – rail x-y cross-section (bore to the right of the rail section) and (b) – armature-rail interface y-z cross-section (trailing edge of armature on the left) (Lv et al. 2014)

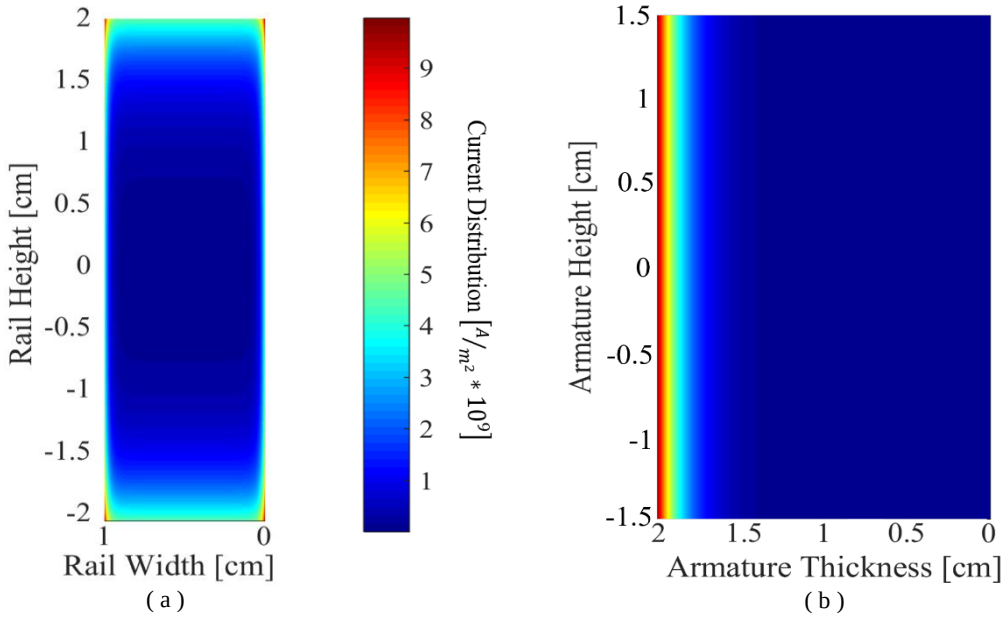

(a) (b)

Figure 14: Current distribution in the (a) – rail x-y cross-section (bore to the right of the rail section) and (b) – armature-rail interface y-z cross-section (trailing edge of armature on the left) computed by the CStSM in MATLAB. The colorbar scale applies to both plots.

The rail comparison is similar, but the overall shape matches the ANSYS result better. The shape of the CStSM result does seem to have a thinner region of high current density, though the colormap on the CStSM result does drop to its darkest level a $1\text{x}10^9$, as opposed to $1.7\text{x}10^7$ in the ANSYS result. Both computations predict higher current density along the rail inner face (on the right side in both plots), though

this is more pronounced in the ANSYS result. Both results predict a current density of about $3\text{x}10^9 \left[{}^{A}/_{m^2}\right]$ along the top and bottom of the rail. The maximum current density in both plots is at the top and bottom corners along the rail inner face, though this maximum is higher in the ANSYS result at $\sim 1.2\text{x}10^{10} \left[{}^{A}/_{m^2}\right]$ compared to $\sim 1\text{x}10^{10}$.

This chapter has described the main principles behind current distribution in railguns, proposed a method to approximate this distribution, and investigated its accuracy. In the force computation, two methods (called F3 and F4) use the CStSM to find the current distribution in the armature. The rest of this paper (with the exception of some finite element B field computations) assumes the use of laminated rails, so the CStSM is not used to compute current distribution in the rails. Regardless, the accuracy of this method demonstrated here coupled with its ease of use compared to finite element solutions means it has promise for use in medium-fidelity analyses and implementation in software packages like MATLAB.

Chapter 4: Magnetic Field

The magnetic field surrounding railgun rails has particular importance due to the role it plays in the Lorentz force. The magnetic field strength inside the armature is of most interest, since this is where it will interact with the crossing current and propel the armature. But the magnetic field strength in the bore is also important, as the fields from each rail repel each other, stressing the rails. To define a readily applicable railgun force model, and because magnetic field can be defined without Maxwell's equations, this computation is done alongside the force computation in MATLAB.

This full solution depends on the computation of the current density, shown in the current distribution chapter. Once $\boldsymbol{A}$ has been computed with the current density, (37) and (39) can be used to find the B field (Zhao et al. 2014) (Zhao et al. 2008) (Keshtkar 2005) (Bayati et al. 2013).

(36) $$\boldsymbol{J} = \sigma\left(-\nabla\Upsilon - \frac{\partial \boldsymbol{A}}{\partial \mathrm{t}}\right)$$

(37) $$\sigma\frac{\partial \boldsymbol{A}}{\partial \mathrm{t}} + \frac{1}{\mu_0}[\nabla\times(\nabla\times\mathbf{A})\,] + \sigma\nabla\Upsilon = 0$$

(38) $$\nabla\cdot(\sigma\nabla\Upsilon) = 0$$

(39) $$\boldsymbol{B} = \nabla\times\boldsymbol{A}$$

Alternatively, the magnetic field can be computed more readily using the Biot-Savart Law. With this method, the rails can either be modeled as individual thin wires at the rail centers, or discretized into a grid of wires equivalent to the full rail. The rail current distribution is assumed to be uniform due to the ability to use laminated rails to avoid skin concentration (described in the Current Distribution Section).

As presented by Xu and Geng (2010) the magnetic field produced by one rail can be evaluated with (41) or (42).

(40) $$G = \frac{(\mathrm{x}+x')}{(\mathrm{y}-\mathrm{y}')^2+(\mathrm{x}+\mathrm{x}')^2}\cdot\left[\frac{\mathrm{z}}{\sqrt{(\mathrm{y}-\mathrm{y}')^2+(\mathrm{x}+\mathrm{x}')^2+z^2}} - \frac{\mathrm{z}-\mathrm{l}}{\sqrt{(\mathrm{y}-\mathrm{y}')^2+(\mathrm{x}+\mathrm{x}')^2+(\mathrm{z}-\mathrm{l})^2}}\right]$$

(41) $$\mathrm{B_y} = \frac{\mu_0\cdot\mathrm{I(t)}}{4\cdot\pi\cdot\mathrm{h}\cdot\mathrm{w}}\int_0^{\mathrm{w}}\int_{-\frac{\mathrm{h}}{2}}^{\frac{\mathrm{h}}{2}} G\ \mathrm{dy}'\cdot\mathrm{dx}'$$

(42) $$dB_y(x,y,z,t) = \frac{\mu_0\cdot\mathrm{I(t)}}{4\cdot\pi}\cdot G\cdot\frac{\mathrm{dy}\cdot\mathrm{dx}}{h\cdot w}$$

These equations can be derived from the Biot-Savart Law for line conductors (43) which can be simplified to (42) for a finite wire, where θ_1 and θ_2 are defined in Figure 15, and r and r' are defined in Figure 16, (Liao et al. 2004).

(43) $$B = \frac{\mu_0}{4 \cdot \pi} \cdot \iiint_V \left(\frac{\boldsymbol{J}(\boldsymbol{r}') \times (\boldsymbol{r} - \boldsymbol{r}')}{|\boldsymbol{r} - \boldsymbol{r}'|^2} \right) dV$$

(44) $$C_1 = \frac{\mu_0 \cdot \mathrm{I(t)}}{4 \cdot \pi \cdot a \cdot \frac{w}{2}}$$

(45) $$B = C_1 \cdot \int_{-\theta_1}^{\theta_2} \sin(\theta)\ d\theta = \frac{\mu_0 \cdot \mathrm{I(t)}}{4 \cdot \pi \cdot b} \cdot (\cos(\theta_2) + \cos(\theta_1))$$

$$where\ b = a + \frac{w}{2}$$

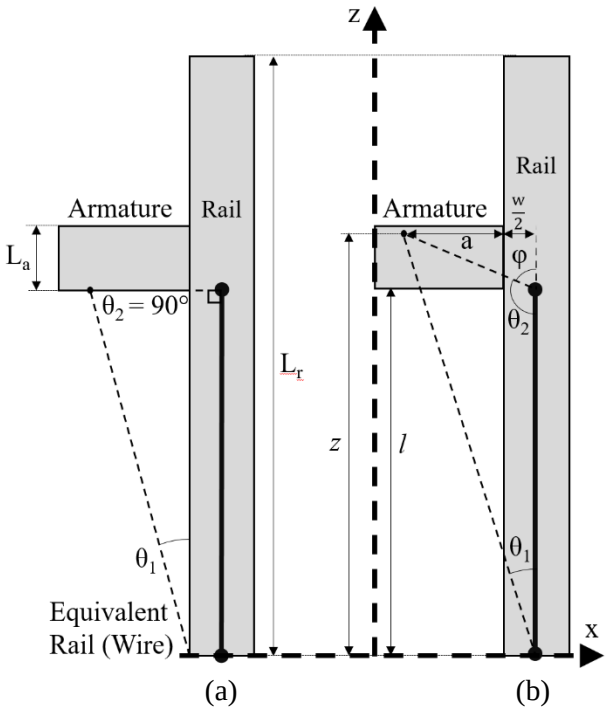

Figure 16: Biot-Savart variable definitions for both thin-rail cases

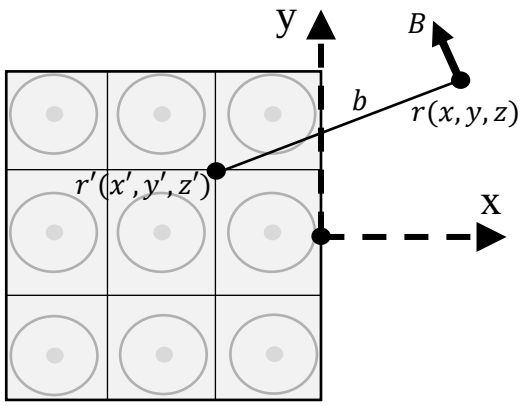

Figure 15: Rear view of the left rail, current at r' produces magnetic field at r

The second angle, θ_2 can be set to 90°, as was done by Waindok Piekielny (2016), if it is assumed that:

- The rails are thin
- Magnetic field is negligible in the z and y directions
    - B_z can be neglected since railguns are long in the z direction, and because end effects are not of particular interest
    - B_x can also be neglected, especially if the armature is smaller than the rails in the y dimension. However, near the top and bottom of the rails, the B field will begin to turn in the x direction, as shown in Figure 36.
- The B field created by current in the armature is negligible, as it will not produce a Lorentz force
- The current does not diffuse into the armature
- The current only flows straight across the armature rear face
- The armature is a simple rectangular shape

These assumptions lead to (46) using the geometry defined in Figure 15 (a). This list of assumptions can be reduced to only the first three by instead using the geometry of Figure 15 (b), meaning B can be computed in the x-z plane, not only along the centerline of the armature rear face with (47).

(46) $$B = C_1 \cdot \cos(\theta_1) = C_1 \cdot \cos\left(\tan^{-1}\left(\frac{b}{l}\right)\right) = C_1 \cdot \left(\frac{l}{\sqrt{l^2+b^2}}\right)$$

(47) $$B = C_1 \cdot (-\cos(\varphi) + \cos(\theta_1)) = C_1 \cdot \left(-\frac{z-l}{\sqrt{(z-l)^2+b^2}} + \frac{z}{\sqrt{z^2+b^2}}\right)$$

(48) $$B = C_1 \cdot \left(-\frac{z-l}{\sqrt{(z-l)^2+x^2+y^2}} + \frac{z}{\sqrt{z^2+x^2+y^2}}\right)$$

In order to arrive at a 3D solution, the y direction is taken into account like the x and z directions were accounted for above, conveniently yielding (48). The next step is to discretize the rail in the x and y directions, as shown Figure 16. This redefines the distance from the wire to the point of interest as the distance between points r and r'. Point r is outside the rail, and represents the location where magnetic field strength is being solved. Point r' is a point inside the rail where current is flowing. This expansion yields (41) also obtained by Xu and Geng (2010)

Two models based on these equations have been developed in MATLAB. One which uses the thin rail assumption and (48), and another which uses (41) fully and the "integral2" MATLAB function. A model using the thin rail assumption is kept because (41) requires the computation of a double integral at each point inside the armature and at each time step, which can become time consuming. Results from both models are shown below, and compared to finite element models in ANSYS Maxwell and the 2D open-source electromagnetics software FEMM (Meeker 2015). FEMM solves low frequency electromagnetic problems with Maxwell's equations by neglecting displacement currents. Due to its straightforward exporting system, results can be (and are) compared directly to MATLAB.

Two cases have been compared here, one based on the railgun presented by Chen et al., described in Table 3, and another based on the railgun presented by Waindok and Piekielny, described in Table 5. The comparison to the Chen et al. railgun compares MATLAB to FEMM results. This case also looks at the difference in B field between rails with uniform and non-uniform current distribution (solid and laminated rails). The comparison to the Waindok and Piekielny railgun includes MATLAB, FEMM, and ANSYS Maxwell results, and examines a range of scaling factors to determine the impact of size.

4.1 Comparison to Chen et al.

Physical Parameters	Symbol	Value	Value	Symbol	Electrical Parameters
Rail Length [m]	L	2	140	I_P	**Peak Current [kA]**
Rail Separation [m]	s	0.02	1.2	t_1	**Current Profile Rise Time [ms]**
Rail Width [m]	w	0.02	4.25	t_2	**Current Profile Decline Time [ms]**
Rail Height [m]	h	0.02	4.25	t_3	**Current Profile Total Time [ms]**
Inductance Gradient [µH/m]	L'	0.454	Value	Symbol	Material Parameters
Armature Width [m]	w_a	0.02	Cu	~	**Rail Material [~]**
Armature Height [m]	h_a	0.02	Al	~	**Armature Material [~]**
Armature Thickness [m]	t_a	0.005	$4 E^{-8}$	ρ	**Armature Resistivity [Ω·m]**
Armature Mass [kg]	m	0.0192			
Initial Velocity [m/s]	V_0	0			

Table 3: Parameters for the Chen et al. railgun (Chen et al. 2015)

The first pair of plots from the MATLAB models (Figure 17 and Figure 18) show the magnetic field of the armature at a range of thicknesses, each represented by a different surface.

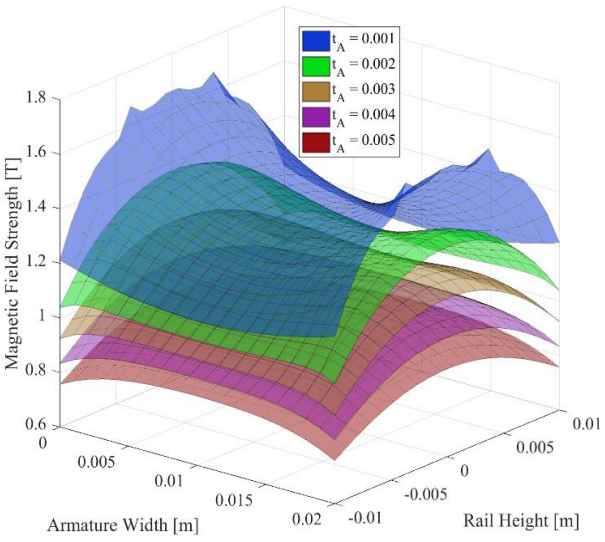

Figure 18: Magnetic field strength in armature for five thickness values of the Chen et al. railgun (Table 3) - computed with (41) and a 1 mm x 1 mm x 1 mm mesh

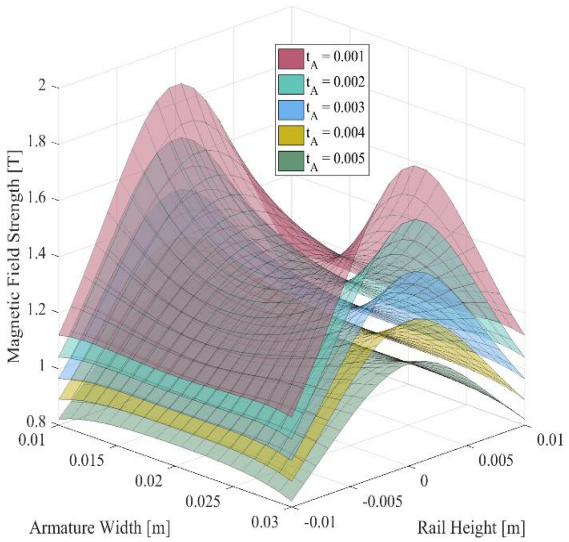

Figure 17: Magnetic field strength in armature for five thickness values of the Chen et al. railgun (Table 3) - computed with (48) (thin rail assumption) and a 1 mm x 1 mm x 1 mm mesh

These solutions are obtained using the values shown from Chen et al., with an armature position of l = 1.995 m. The mesh used in the armature was a 20 x 20 x 5 division grid in the w_a x h_a x t_a dimensions, giving an "element" size of 1 mm x 1mm x 1mm. The rail is only divided in x and y, and used a similar 1 mm x 1mm element size.

It can be seen that the magnetic field is largest when closest to the rails and armature rear face (t_A = 0). This is expected since the vertical edges of the rear face are nearest to the active rails. The shape also changes with distance from the rear face, where peaks along the rail inner face disappear with distance. This corresponds to the magnetic field forming around the end of the active rail. Some roughness can be observed at the armature vertical edges in Figure 17. This seems to stem from errors in the numeric integration, despite very tight error tolerances ($< 1x10^{-15}$) and the absence of asymptotes or singularities. One objective of future work would be to discover the source of this roughness and remove it, though the roughness is not severe, and it should not alter the overall computed force by any more than 0.1%. The two MATLAB methods shown provide fairly similar results, but the thin rail assumption leads to more dramatic

peaks, since all the current is concentrated along a line. This means the thin rail model gives a maximum that is 11.76% larger (in this case) than the thick rail model, though the average B field value is only 4.65% larger (1.1843 T in the thin rail model, 1.1317 T in the thick rail model). Another difference between the two is the shape of the falloff with distance from the armature rear face. The thin rail model falls off more slowly, and retains the peaks at the armature edges. For example, the bottom left corner of the two surface plots shows that the thick rail model drops over 0.4 T between the largest and smallest thickness values. The same point in the thin rail model drops less than 0.3 T.

These differences can also be seen in Figure 19, where the thick rail model drops to the minimum value earlier than the thin rail model. Regardless, since the result of the two models is similar overall, and the thin rail model is computationally much quicker, both models are carried forward.

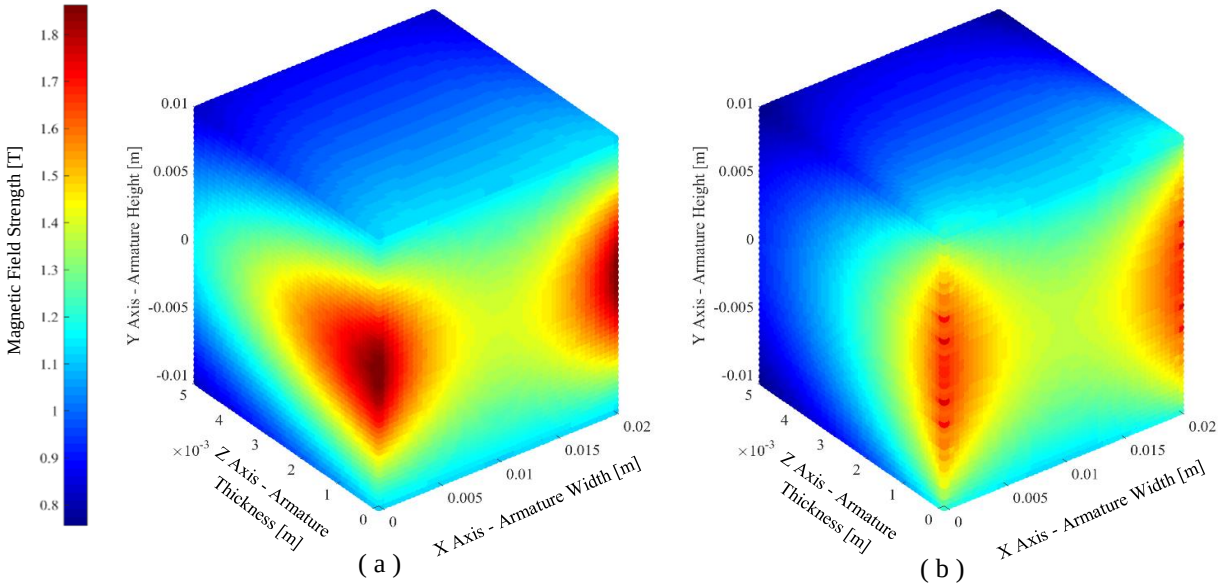

Figure 19: Magnetic field strength in armature for the Chen et al. railgun (Table 3), oriented as shown in Figure 20 (a) - Thin Rail Model (b) - Thick Rail Model (both computed with a 0.4 mm x 0.4 mm x 0.1 mm mesh)

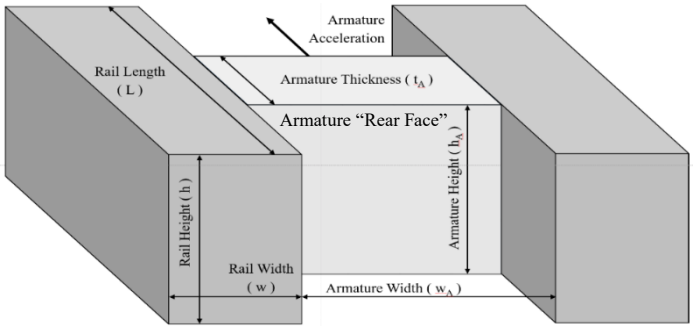

Figure 20: Orientation of Figure 19 armature magnetic field plots

The FEMM setup and results for the Chen et al. railgun comparison are shown in Figure 22 and Figure 21. The simulation considered the rails to be copper and the armature to be Aluminum 6061-T6. The rails and armature are surrounded by a region of air 0.109 m in diameter with a $B = 0$ boundary applied around its circumference. The excitation current is applied to each rail separately, so the right rail receives an input of 140 kA and the left rail produces an outlet current of -140 kA. The elements are planar first-order triangular elements with edges about 0.0014 m long (Meeker 2015). This result validates the shape of the B field between the rails shown in Figure 17, Figure 18, and Figure 19, where the field is largest at the center of the rail inner face, and falls off with distance from this point. It also shows a more gradual falloff like that shown by the thick rail model, giving some justification for the extra computational time. However, the values produced by the MATLAB models are approximately ½ the magnitude of the FEMM results. This discrepancy is explored more in the next comparison.

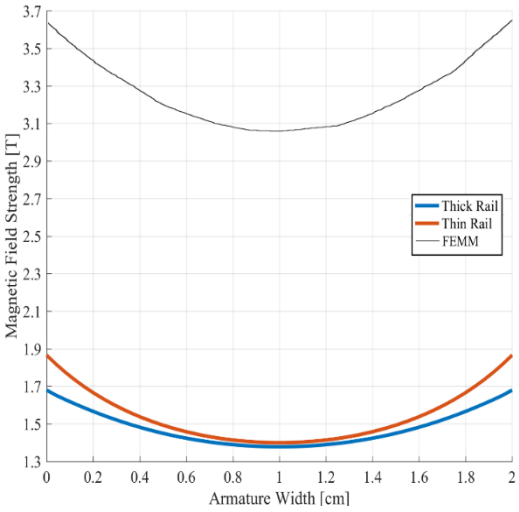

Figure 21: Comparison of MATLAB models vs. FEMM results along the armature centerline (shown in Figure 22) for the Chen et al. railgun (Table 3)

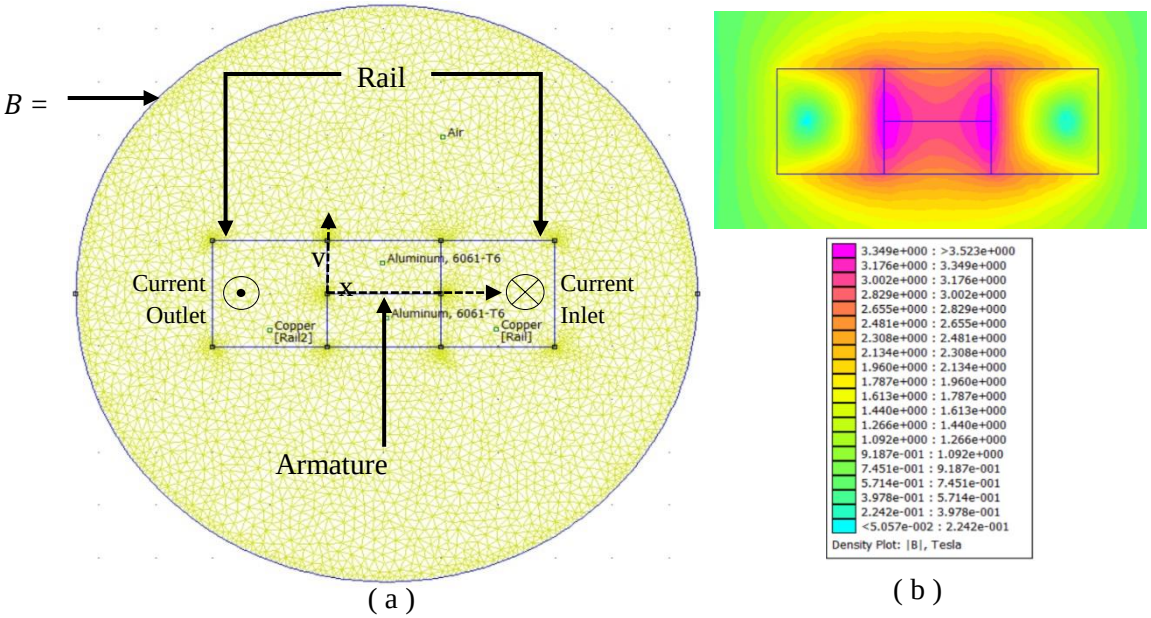

Figure 22: FEMM setup (a) and results (b) for the Chen et al. railgun (Table 3) mesh: 4704 Nodes 9046

Though it is generally assumed here that current distribution in the rails is uniform, a comparison was done to look at the differences in magnetic field between uniformly distributed (laminated) rails, and solid rails. This was done using a method demonstrated by Lv et al. (2014) which uses a hollow rail to force a static finite element solver to consider skin effects. Since a negligible amount of current flows through the center of solid rails, this conductor material can be removed in the simulation. Figure 23 and Figure 24 show the *B* field in the armature as computed by FEMM and ANSYS Maxwell respectively.

		B Field [T]	
		Max	Min
Solid Rail	**FEMM**	3.62286	2.6184
	ANSYS	5.5573	4.81
	Error	-34.81%	-45.56%
Hollow Rail	**FEMM**	3.51901	2.60614
	ANSYS	6.2344	4.85
	Error	-43.55%	-46.27%

Table 4: Comparison of ANSYS and FEMM results for the Chen et al. case

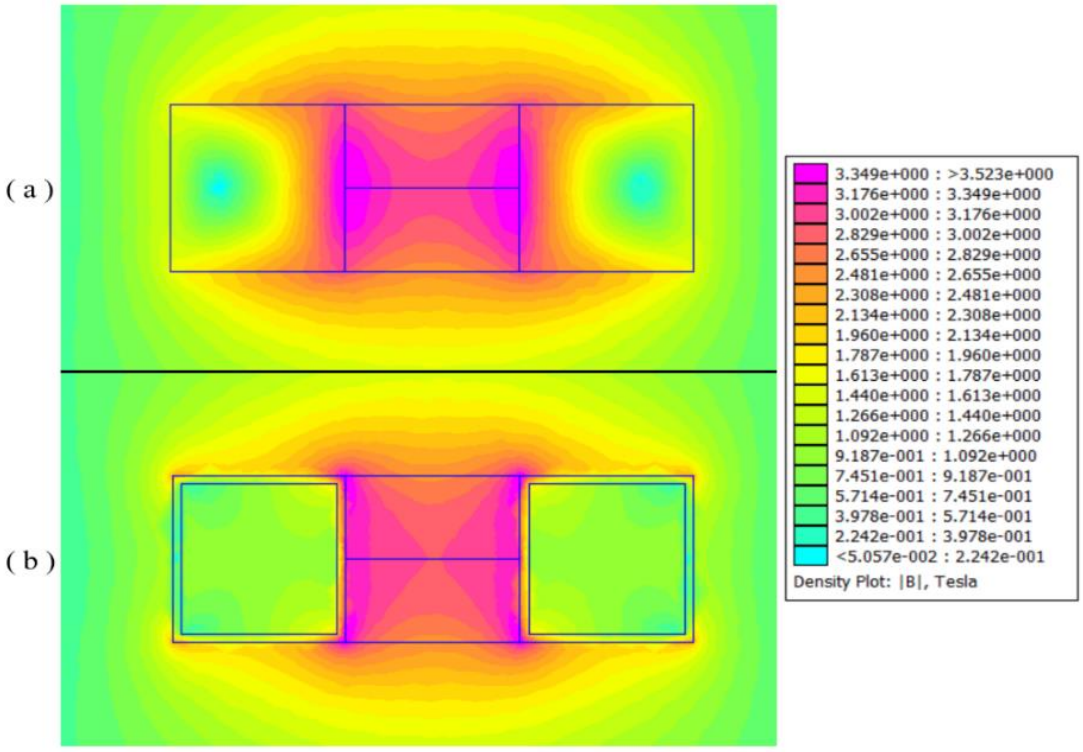

Figure 23: FEMM *B* field results for the Chen et al. case (Table 3) (a) – laminated rail / uniform current distribution (b) – solid rail / current concentrated along edges from AC skin effect

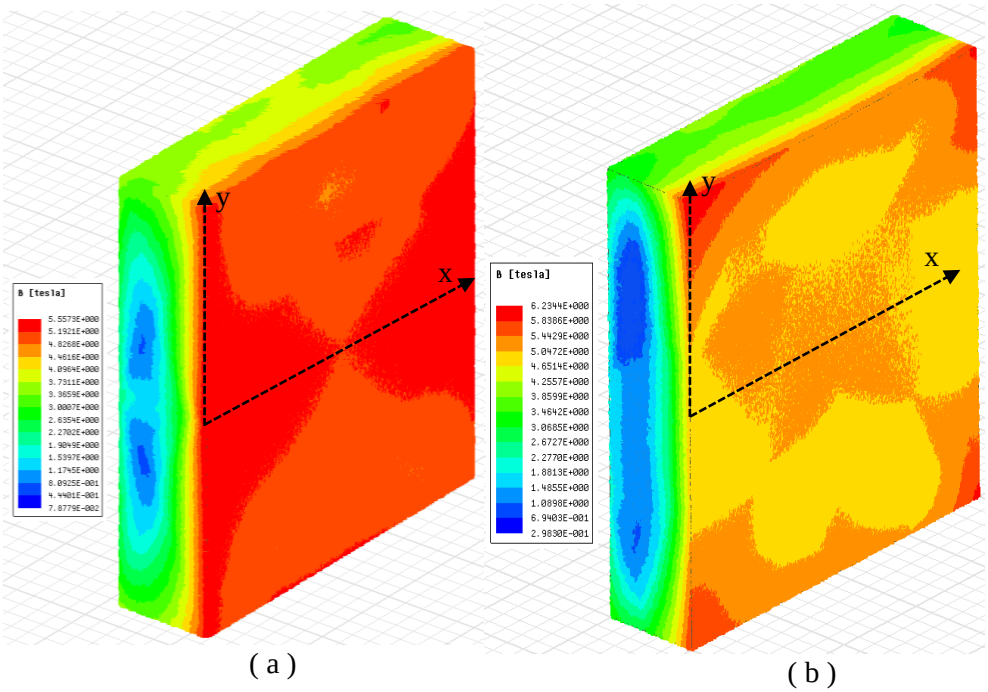

Figure 24: ANSYS Maxwell *B* field results for the Chen et al. case (Table 3) (a) – laminated rail / uniform current distribution (b) – solid rail / current concentrated along edges from AC skin effect

The models generally agree on shape, with the solid rail (modeled with a hollow rail) having maximum magnetic field at the center of the rails, and the laminated rail (modeled with a solid rail) having maximum magnetic field at the top and bottom of the rails. The ANSYS laminated rail result does show a strange increase in magnetic field near the center of the armature. This difference could be from the ANSYS simulation considering current flowing through the armature, when the FEMM simulation does not. However, the current flows through the whole armature rear face, and should not produce more magnetic field near the center. Additionally, while the comparison provided here is largely qualitative, it should be noted that the FEMM and ANSYS results disagree on the magnitude of the *B* field between the rails, with an overall discrepancy of about 45% between the two. Regardless, the overall shape of both simulations agree, and show that a uniform current distribution produces a larger overall magnetic field along the armature rear face, while the solid rail produces a magnetic field with higher peaks, but lower overall magnitude.

4.2 Comparison to Waindok and Piekielny

Physical Parameters	Symbol	Value	Value	Symbol	Electrical Parameters
Rail Length [m]	L	0.2	1→20	I_P	**Peak Current [kA]**
Rail Separation [m]	s	0.012	~	t_1	**Current Profile Rise Time [ms]**
Rail Width [m]	w	0.01	~	t_2	**Current Profile Decline Time [ms]**
Rail Height [m]	h	0.01	~	t_3	**Current Profile Total Time [ms]**
Inductance Gradient [μH/m]	L'	0.50	Value	Symbol	Material Parameters
Armature Width [m]	w_a	0.012	Cu	~	**Rail Material [~]**
Armature Height [m]	h_a	0.0058	Al	~	**Armature Material [~]**
Armature Thickness [m]	t_a	0.0296	$4 E^{-8}$	ρ	**Armature Resistivity [Ω·m]**
Armature Mass [kg]	m	0.0056			
Initial Velocity [m/s]	V_0	0			

Table 5: Railgun parameters used throughout this paper, used by Waindok and Piekielny (2016) (CC1)

The MATLAB and FEMM results for the Waindok and Piekielny comparison look very similar to those of the previous comparison, so plots resembling Figure 17, Figure 18, and Figure 23 are not presented here. As can be seen in Table 6, the magnitude of the *B* field in the base Waindok and Piekielny railgun is a little more than ¼ of that in the previous case. While this case is about ½ the size of the previous one geometrically (which would suggest it should have a stronger magnetic field), it uses only $^1/_7$ of the excitation current, so the smaller *B* field is consistent with expectations. The same 20 x 20 x 5 division is used in this case, meaning the element size is now 0.6 mm x 0.5 mm x 5.92 mm.

	Thick Model Error	Thin Model Error	Average *B* Field on Armature Centerline		
			Thick Model	Thin Model	FEMM
x0.1 @ 20kA	-49.9%	-48.1%	3.926	4.077	7.833
x0.25 @ 20kA	-50.6%	-48.8%	1.571	1.631	3.177
x0.5 @ 20kA	-51.8%	-50.0%	0.785	0.815	1.628
x0.75 @ 20kA	-53.3%	-51.6%	0.524	0.544	1.120
x1 @ 1kA	-55.2%	-53.6%	0.020	0.020	0.044
x1 @ 10kA	-55.2%	-53.6%	0.196	0.204	0.438
x1 @ 20kA	-55.2%	-53.6%	0.393	0.408	0.877
x1 @ 50kA	-55.2%	-53.6%	0.982	1.019	2.192
x1 @ 100kA	-55.2%	-53.6%	1.963	2.039	4.383
x2 @ 20kA	-55.9%	-54.3%	0.196	0.204	0.445
x5 @ 20kA	-55.6%	-51.7%	0.079	0.082	0.177
x10 @ 20kA	-51.5%	-49.8%	0.039	0.041	0.081

Table 6: Comparison of MATLAB models vs. FEMM for the Waindok and Piekielny railgun (Table 5) – errors computed by finding the error between the at each data point and averaging over the – uses a mesh with elements of 0.6 mm x 0.5 mm x 5.92 mm

The factor of ~2 discrepancy between the MATLAB models and finite element solutions also exists in this comparison. To further investigate this, the change in B field with a range of geometric scales and excitation currents is examined to see how consistent this difference is. The geometric scaling is done by simply increasing each geometric value listed in Table 5 by a specified factor. Thus, the rails in the x2 case are 2 cm x 2 cm rather than 1 cm x 1 cm.

To perform this examination, the B field along the centerline of the armature (shown in Figure 21) is plotted for both MATLAB methods and the FEMM results on the next page (Figure 25). The errors for each method relative to the FEMM results are listed in Table 6, and show both MATLAB models to be reliably about ½ of the FEMM value. The source of this consistent error is unknown, and future work would focus on this. Ignoring the z component of the B field should not impact this, as the B field is only vertical along the center of the rail face. Assuming the current that flows the armature does not contribute to the B field should not be responsible for this error since the FEMM simulation also does not consider current flow in the armature. Furthermore, the ANSYS simulation (which does model current in the armature) gets results similar to the FEMM model (a difference of 9.8% between maximum values) so this assumption would not be responsible for a 50% error. It should be noted that, while the FEMM and ANSYS results for the Chen et al. case disagreed significantly, their results for this case were consistently within 10%.

In addition to geometric scaling (which uses the 20 x 20 x 5 division scheme for each model), the impact of mesh refinement was examined by reducing the element size to 0.06 mm x 0.05 mm x 0.296 mm for the 20 kA original geometry case. This result had no discernable difference from the larger element size for either the thick or thin rail case, so it is unlikely that mesh size plays a significant role in model accuracy.

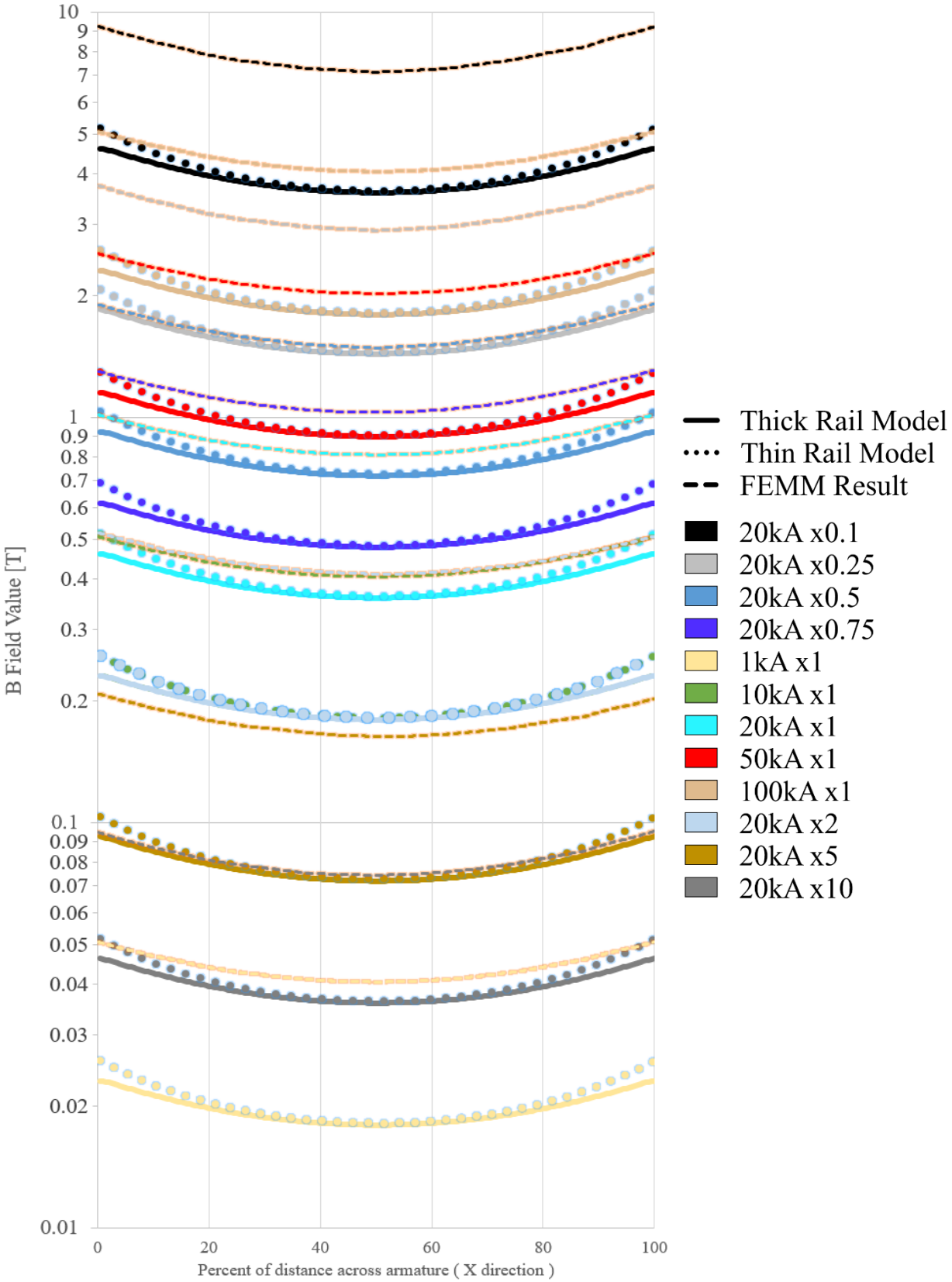

Figure 25: Comparison of MATLAB models vs. FEMM results for varying scales with the Waindok and Piekielny railgun case (Table 5)

Lastly, different rail aspect ratios were examined by changing the Waindok and Piekielny railgun to use rails that are 2 cm wide by 1 cm tall and 1 cm wide by 2 cm tall. When compared to FEMM results, the thick rail model maintained this factor of ~ ½ relationship. The thin rail model also maintained this relationship for the 2 cm x 1 cm rail, but the 1 cm x 2 cm rail exacerbates the peak-shape of the thin rail model since there is more room for the field to fall off above and below the "wire" that represents the rail. This means that the field is predicted to be larger than the thick rail model and departs from ½ of the FEMM result (the thin rail model predicts a maximum of 0.512 T vs. the thick rail result of 0.329 T vs. the FEMM result of 0.697 T). But the peak-like nature of this model means that the B field at the top and bottom of the armature is significantly underpredicted, so the average value along the armature rear face is 0.30 T for the thin rail model compared to 0.279 T for the thick rail model. It is predicted that these issues will be worse for lower $^{w}/_{h}$ ratio rails, and railguns with wider armatures / more rail separation. However, since this error is consistent for the thick rail model, and still fairly consistent for the thin rail model, a correction factor of 2 is applied to the B field equations of (41) and (48) to correct the MATLAB results to match those from finite element solutions. Even though the discrepancy is not *exactly* double, and it is unlikely that a direct factor of two is missing, the application of this factor reduces the average error for all the cases in Table 6 from -52.9% to -5.8%. This improved accuracy lends greater credence to the final force model, which depends on these methods.

Also of note is that error for the thin rail model decreases significantly near the armature edges (rail faces) as shown in Figure 26. This corresponds to the more dramatic peaks seen at the rail faces in the thin rail model. While the error is decreasing, it does not seem to be due to an actual increase in accuracy. Instead the erroneous peak in the thin rail model partially cancels out the larger

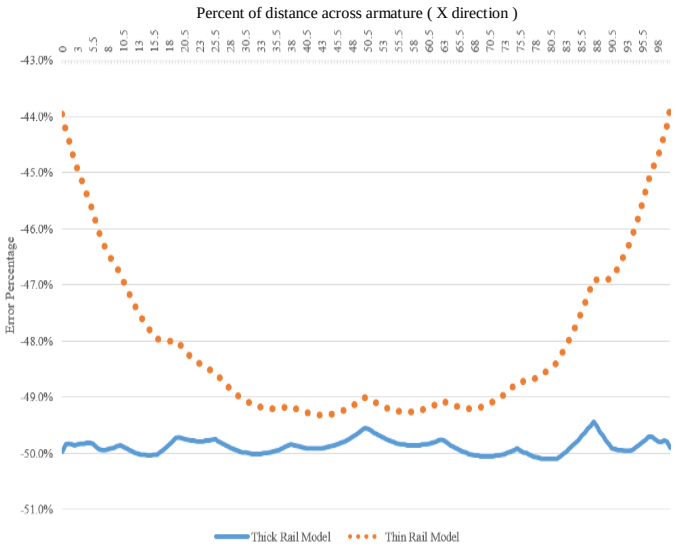

Figure 26: Comparison of thick and thin rail model errors vs. FEMM for the x0.1 scale Waindok and Piekielny railgun case (Table 5)

factor of ~ ½. Since the thick rail model does replicate the shape of the FEMM results more accurately, it should still be seen as the more accurate model, despite the fact that the thin rail model has lower average error values.

The shape of the thick rail model seems to be validated in the x–y plane by comparing the MATLAB and FEMM results in Figure 19 and Figure 21, and the MATLAB and FEM results in Figure 27 and Figure 28. The shape in the z direction can only be assessed by examining the ANSYS Maxwell result. The rate at which the B field falls off with distance from the armature rear face is nearly equal between the MATLAB and FEM results, when accounting for the magnitude difference between the two. However, the convex shape (as seen from the armature rear face) of the decreasing field shown in Figure 28 is not replicated by the MATLAB models. The exact cause of this discrepancy is not known, but it should have little impact on the computed force, as the current flowing through the front of the armature is quite small, and the B field drops to levels that are similarly small between the MATLAB and FEM results.

This chapter has presented two methods to compute the magnetic field in the armature, and compared them to finite element solutions in FEMM and ANSYS Maxwell. Overall, once the correction factor has been introduced, both of these methods agree well with finite element results, and lend themselves to use in computing force in MATLAB and similar software packages. While the thick rail model is more accurate than the thin rail model, it is yet to be seen if the extra computational effort required for the thick rail model is justified. This will be determined in the force computation chapter.

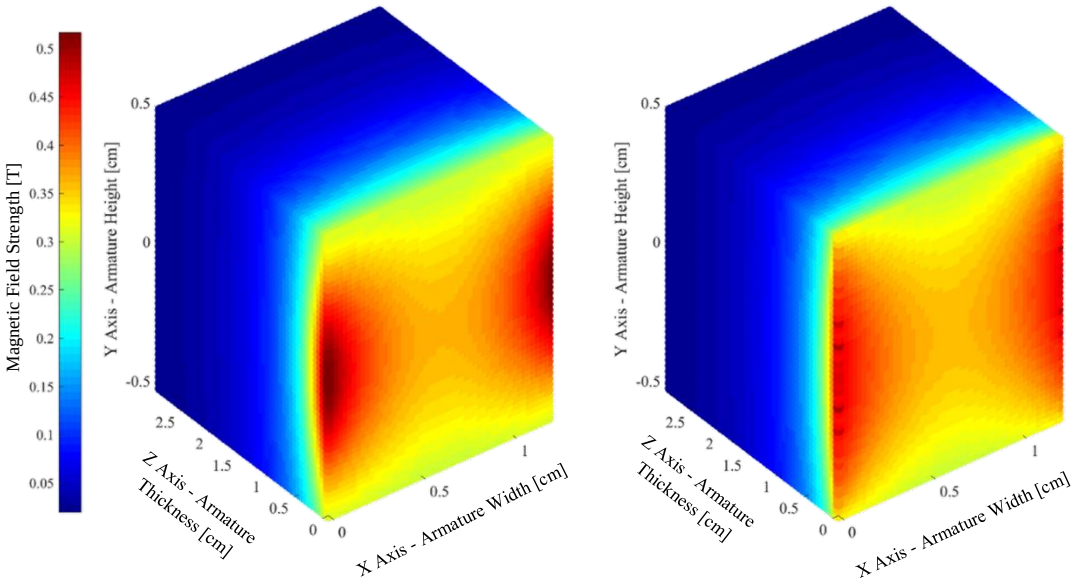

Figure 27: Magnetic field strength in armature for the Waindok and Piekielny railgun (Table 5), orientation shown in Figure 20 (a) - Thin Rail Model (b) - Thick Rail Model

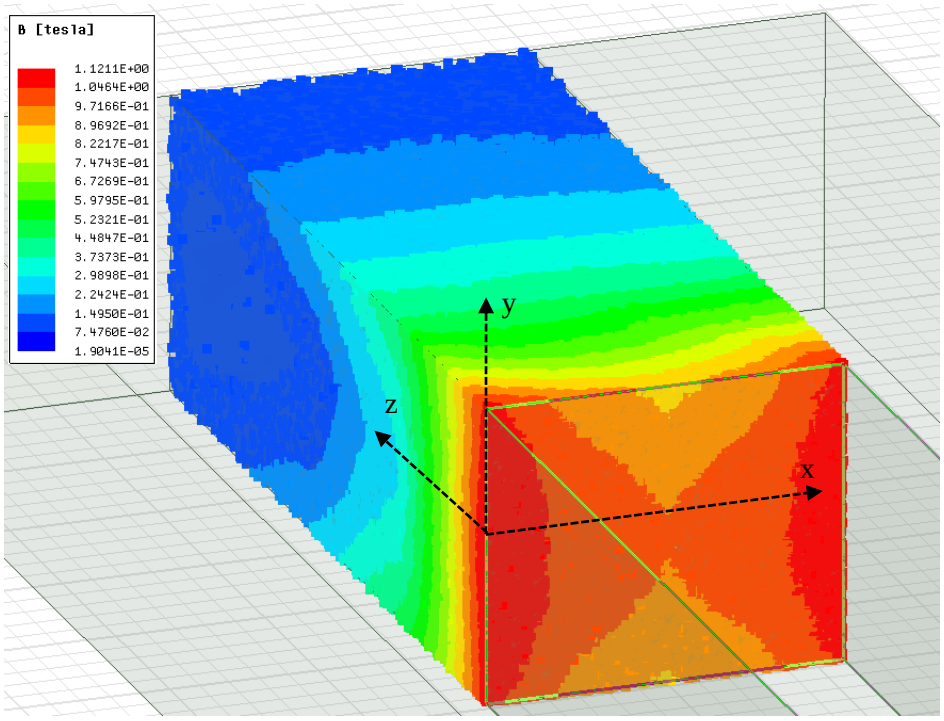

Figure 28: ANSYS Maxwell result for the Waindok and Piekielny railgun (Table 5). The origin has been shifted to stay on the armature rear face in this figure for readability, but all computations are done considering $z = 0$ to be at the breech.

Chapter 5: Inductance Gradient

Many equations describing railgun operation, such as those for current distribution, force, and efficiency can be greatly simplified using the inductance gradient (L') (Bayati et al. 2011) (Murugan et al. 2016) (McCorkle and Bahder 2010). L' is measured in microhenries per meter (μH/m), and is a function of rail geometry, rail separation (s), rail material, and current distribution as a function of time (Keshtkar 2005) (Keshtkar et al. 2009) (Huerta and Nearing 1991). Since railguns operate on DC current, dependence on transient current distribution is normally neglected (Keshtkar et al. 2009), though the skin effect (which is due to transience, as described in the current distribution section) is frequently considered. Thus, for the simple case of a railgun with rectangular copper rails, L' is considered to be dependent only on rail separation (s), rail width (w), and rail height (h) as shown in Figure 29.

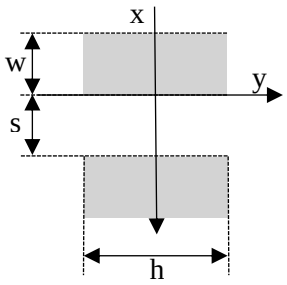

Figure 29: Dimension description for rectangular rails

Usually, it is necessary for researchers to use a finite element or finite difference approach to compute L'. While this is more accurate, it is time consuming, and pushes railgun designers to depend on tables like the ones provided by Keshtkar et al. (2009) and others. For convenience, a compilation of the tables located during this investigation is provided in Appendix A. Due to the effort required to calculate L' via FEA, multiple approximation methods have been developed using only geometric values. This simplicity comes at a cost though, as it generally limits the application of these methods to rectangular rails (as shown in Figure 29). The derivation of many of these approximation methods rely on the fact that, in railguns with solid rails, significant current only flows through a thin layer on the rail surface. The depth of the current distribution is called “skin depth” (Keshtkar 2005) (Huerta and Nearing 1989) (Keshtkar, Bayati, and Keshtkar 2009).

5.1 Kerrisk Method

A common approach called the Kerrisk method was developed for rectangular conductors by J. F. Kerrisk in 1981 at the Los Alamos National Laboratory (Kerrisk 1982) (Jin et al. 2012). In developing this method, Crandall's method was used to compute the current distribution in the rails. The inductance and magnetic flux of the circuit were then found, eventually leading to L' by integrating the magnetic field strength over the conductor area. This process yielded (51), and values shown in Table 7 were found by performing a least squares fit of this equation to the obtained L' results.

	Value	Standard Deviation
A [μH/m]	0.4406410	0.0032
B [μH/m]	-0.0777133	0.0014
K_{a1}	3.397143	0.146
K_{a2}	-0.0660307	0.0069
K_{b1}	1.007719	0.0089
K_{b2}	2.743651	0.0581
K_{b3}	0.0220931	0.0036
K_{b4}	0.2637392	0.0368

Table 7: Kerrisk method coefficients

(49) $$F_1 = 1 + K_{a1} \times \left(\frac{w}{h}\right) + K_{a2} \times \frac{w}{h} \times \frac{s}{h}$$

(50) $$F_2 = K_{b1} + K_{b2} \times \frac{s}{h} + K_{b3} \times \frac{w}{h} + K_{b4} \times \frac{s}{h} \times \frac{w}{h}$$

(51) $$L' = [\, A \, + B \times \ln(F_1) \,] \times \ln(F_2)$$

This finally produces a relatively easy-to-use equation (52). (Kerrisk 1982)

(52) $$L' = \left[A + B \times \ln\left(1 + K_{a1} \times \left(\frac{w}{h}\right) + K_{a2} \times \frac{w}{h} \times \frac{s}{h}\right)\right] \ldots$$
$$\ldots \times \ln\left(K_{b1} + K_{b2} \times \frac{s}{h} + K_{b3} \times \frac{w}{h} + K_{b4} \times \frac{s}{h} \times \frac{w}{h}\right)$$

In this process, the following assumptions were made:

- The conductors (rails) are very long in the z direction (into the page in Figure 29)
- Current only flows in the z direction
- Current only flows on the conductor surface
- The conductor corners are rounded (current density would become infinite for square corners)
- The circuit is symmetric about the x-axis

This equation was implemented, and a replication of Kerrisk's results showing very good agreement is shown in Figure 56, Figure 57, and Figure 58 of Appendix B. These were made by superimposing Kerrisk's results on the MATLAB results computed here.

5.2 Huerta Conformal Mapping Method

Another approximation method was developed for rectangular rails by Huerta et al. in 1991. To develop this method, conformal mapping and the Schwartz-Christoffel transformation were used to map the rail boundaries. In doing this, Huerta et al. assumed the following:

- The rail dimensions are much larger than the skin depth
- The current travels only on the rail surface
- There is no magnetic field inside the rails

It is interesting to note that the singularity presented by sharp corners is not an issue here, as this method does not require a numeric computation of current distribution. The equations used to find L' with this method are provided as Equations (53) → (56), including the complete elliptic integral (K) (Gradshteyn and Ryzhik 2007).

(53) $$L' = \mu_0 \times \frac{K(k')}{K(k)}$$

(54) $$k' = \sqrt{u_N} = \sqrt{1 - k^2}$$

(55) $$k = \sqrt{1 - u_N}$$

(56) $$K = complete\ elliptic\ integral = K(k) = \int_0^{\pi/2} \frac{1}{\sqrt{1 - k^2 * \sin(x)^2}}\, dx$$

This approach is less simple than others, and requires that Equations (57) → (61) on the next page be root-solved for the unknowns u_N, u_O, and u_P. A table of solved values from this method can be found in Figure 52 of Appendix A: Inductance Gradient Tables (Huerta and Nearing 1991).

(57) $$G(a,b,c,d,e) = \int_a^b \left|\frac{(u-c)*(u-d)}{u*(u-e)*(1-u)}\right|^{1/2} du$$

(58) $$\frac{s}{2} = \alpha \times G(0, u_N; u_O, u_P, u_N)$$

(59) $$\frac{h}{2} = \alpha \times G(u_N, u_O; u_O, u_P, u_N)$$

(60) $$\frac{h}{2} = \alpha \times G(u_P, 1; u_O, u_P, u_N)$$

(61) $$w = \alpha \times G(u_O, u_P; u_O, u_P, u_N)$$

5.3 Intelligent Estimation Method (IEM)

In 2009, Keshtkar, Bayati, and Keshtkar developed an equation for the L' of rectangular rails using the Intelligent Estimation Method (IEM). IEM consists of the compilation of significant variables, a breakdown into analytically known physical components, a linear combination of these components using weighting coefficients, and finally a comparison to experimental results. If the error is not negligibly small, the weighting coefficients are recalculated, and this process is repeated until errors become small. In applying this to the computation of L', Keshtkar et al. assumed that:

- Current only flows on the outer surface of rectangular conductors
- These outer faces can be separated into 4 distinct pairs of plates (one pair being the top surface of each rail, the second being the right surface of each rail, and so on)
- The current that flows into one plate on the first rail flows out of the corresponding plate on the second rail

Using these assumptions and the IEM, Keshtkar, Bayati, and Keshtkar found the L' of each pair of plates. These were then linearly combined, as shown in (62).

(62) $$\frac{1}{L'} = A_1 \times \frac{h}{s} + A_2 \times \frac{h}{s+2\times w} + A_3 \times \frac{1}{ln\left(\frac{4\times(s+w)}{w}\right)} + A_4 \times \frac{1}{ln\left(\frac{4\times(s+w)}{w}\right)}$$

The coefficients were computed by comparing initial values to FEA results, and correcting until the error became sufficiently small. The resulting L' equation is shown as (63). This method will be referred to as the IEM method in the rest of this paper (Keshtkar, Bayati, and Keshtkar 2009).

$$L' = \frac{10^{-6}}{0.5986\times\frac{h}{s} + 0.9683\times\frac{h}{(s+2\times w)} + 4.3157\times\frac{1}{\ln\left(\frac{4\times(s+w)}{w}\right)} - 0.7831} \quad (63)$$

Similar to the Kerrisk method description, this method was implemented, and a replication of the results produced by Keshtkar et al. showing very good agreement is shown in Figure 59**,** Figure 60, and Figure 61 of Appendix B. These were again made by superimposing the results of Keshtkar, Bayati, and Keshtkar on the MATLAB results computed here.

5.4 L' Regression Method (LRM)

The most recent approximation method was developed by Murugan et al. and was published in 2016. This method uses regression analysis with the Oakdale Data Fit Engineering software program to approximate L' from FEM results obtained using ANSOFT. The software program computes 254 equations to describe L', and the best of these were chosen, with regression values $R_a \rightarrow R_j$ provided in Table 8**:** LRM regression values. This method will be referred to as the Inductance Gradient Regression Method (LRM) in this report.

	Rectangular	Circular (θ=40º)	Circular (θ=10º)
$\mathbf{R_a}$	0.45173	0.28119	0.11373491
$\mathbf{R_b}$	0.25006	-0.088383	-0.03997613
$\mathbf{R_c}$	-0.06491813	0.540073	0.13263606
$\mathbf{R_d}$	0.04216090	0.00476755	0.016023852
$\mathbf{R_e}$	-0.00454295	-1.9731854	-0.29597112
$\mathbf{R_f}$	-0.03898298	-0.048983	-0.062019418
$\mathbf{R_g}$	0.000974821891	0.0028816	0.00425462548
$\mathbf{R_h}$	0.0018307804	2.780857	0.39459707
$\mathbf{R_i}$	-0.00416014722	-0.012536	0.0337784518
$\mathbf{R_j}$	-0.00581360388	-0.0199827	-0.00645150442

Table 8: LRM regression values

Unlike the other methods listed, this approximation also considers circular rails. However, analytical limitations arise because the geometry of circular rails is described by two units (length and angle) instead of one (length). The geometry of this sort of rail is shown as Figure 30, and can be described by thickness (t), separation (s), and opening angle (θ). This means that instead of one equation that can be used for all geometric configurations, circular rails require one value to be held constant. Murugan et al. decided to hold opening angle constant, and compute equations for rails with θ values of 10 and 40 degrees. These both use (65), but use different regression values from Table 8. (Murugan et al. 2016)

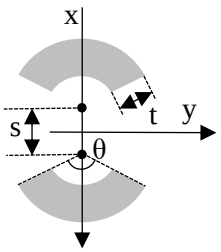

Figure 30: Dimension description for circular rails

(64) $$L'_{rectangular} = R_a + R_b \times \ln\left(\frac{s}{h}\right) + R_c \times \ln\left(\frac{w}{h}\right) + R_d \times \ln\left(\frac{s}{h}\right)^2 \ldots$$
$$\ldots + R_e \times \ln\left(\frac{w}{h}\right)^2 + R_f \times \ln\left(\frac{s}{h}\right) \times \ln\left(\frac{w}{h}\right) \ldots$$
$$\ldots + R_g \times \ln\left(\frac{s}{h}\right)^3 + R_h \times \ln\left(\frac{w}{h}\right)^3 \ldots$$
$$\ldots + R_i \ln\left(\frac{s}{h}\right) \times \ln\left(\frac{w}{h}\right)^2 + R_j \times \ln\left(\frac{s}{h}\right)^2 \times \ln\left(\frac{w}{h}\right)$$

(65) $$L'_{circular} = R_a + R_b \times ln\left(\frac{t}{s}\right) + R_c \times \left(\frac{1}{s}\right) + R_d \times \ln\left(\frac{t}{s}\right)^2 + R_e \times \left(\frac{1}{s}\right)^2 \ldots$$
$$\ldots + R_f \times \frac{\ln\left(\frac{t}{s}\right)}{s} + R_g \times \ln\left(\frac{t}{s}\right)^3 + R_h \times \left(\frac{1}{s}\right)^3 + R_i \times \left(\frac{\ln\left(\frac{t}{s}\right)}{s}\right)^2 \ldots$$
$$\ldots + R_j \times \left(\frac{\ln\left(\frac{t}{s}\right)^2}{s}\right)$$

5.5 Comparison of L' Methods

Inductance gradient values have been found using the Kerrisk, IEM, and LRM methods, and a comparison has been performed. Previous investigations (Kerrisk 1982) (Murugan et al. 2016) have compared the results from these methods to finite element or finite difference results using various separation-to-height and width-to-height ratio values. One method uses the following four cases to compare results for rectangular rails:

Case 1: high $\frac{s}{h}$ and high $\frac{w}{h}$ **Case 2:** low $\frac{s}{h}$ and low $\frac{w}{h}$

Case 3: high $\frac{s}{h}$ and low $\frac{w}{h}$ **Case 4:** low $\frac{s}{h}$ and high $\frac{w}{h}$

The results of this comparison can be seen in Figure 31. These plots show reasonable agreement between the methods, with the exception of the IEM in Case 3, which departs significantly from the other methods. The IEM is generally the outlier in this comparison, and is the least accurate when compared to FEM results in Case 2. The FEM values used here come from the article by Murugan et al. in which the LRM is introduced (Murugan et al. 2016). FEM values were not available for comparison in the other cases.

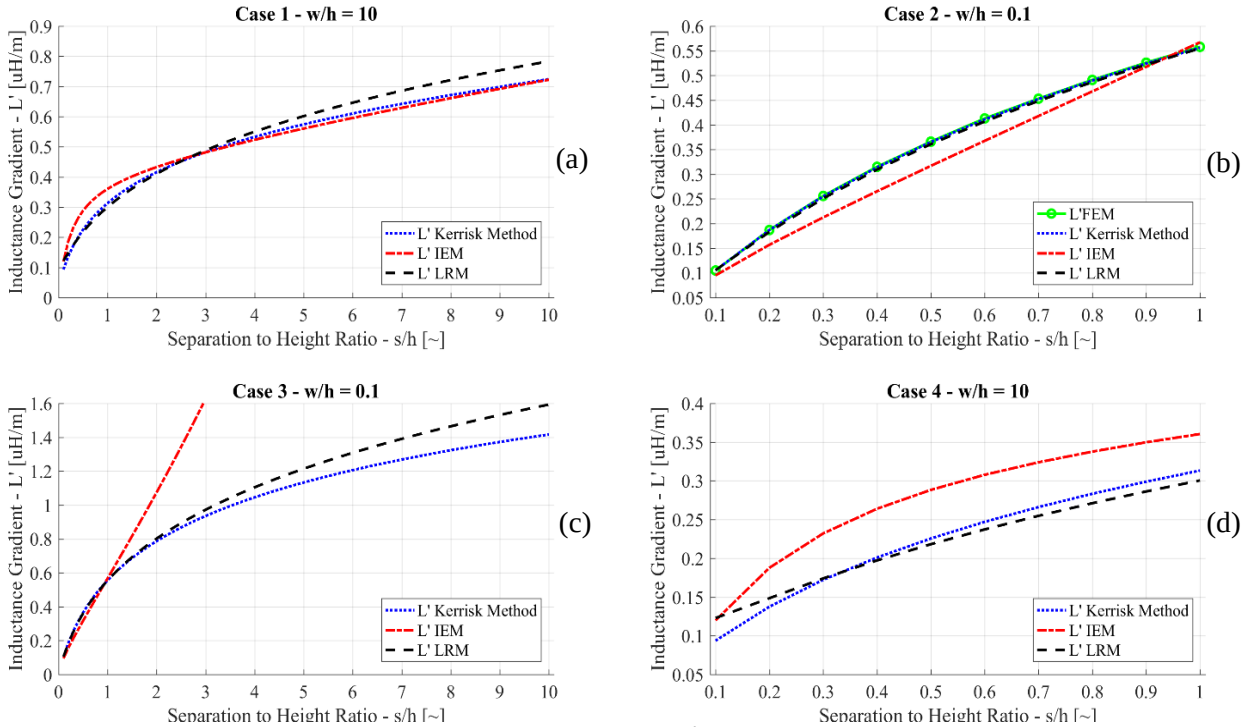

Figure 31: 4-Case Comparison of $L^{'}$ Computation Methods

Because Murugan et al. present FEM results over the range of s/h and w/h from 0.1 to 1, a surface plot is presented in Figure 32 on the next page. This shows a similar agreement between the methods, with the IEM showing the most disagreement. The error of each method is plotted in Figure 33, and quantified in Table 9 also on the next page. The LRM has the smallest error, but this does not necessarily mean it is the most accurate, as it was developed using the FEM values used here.

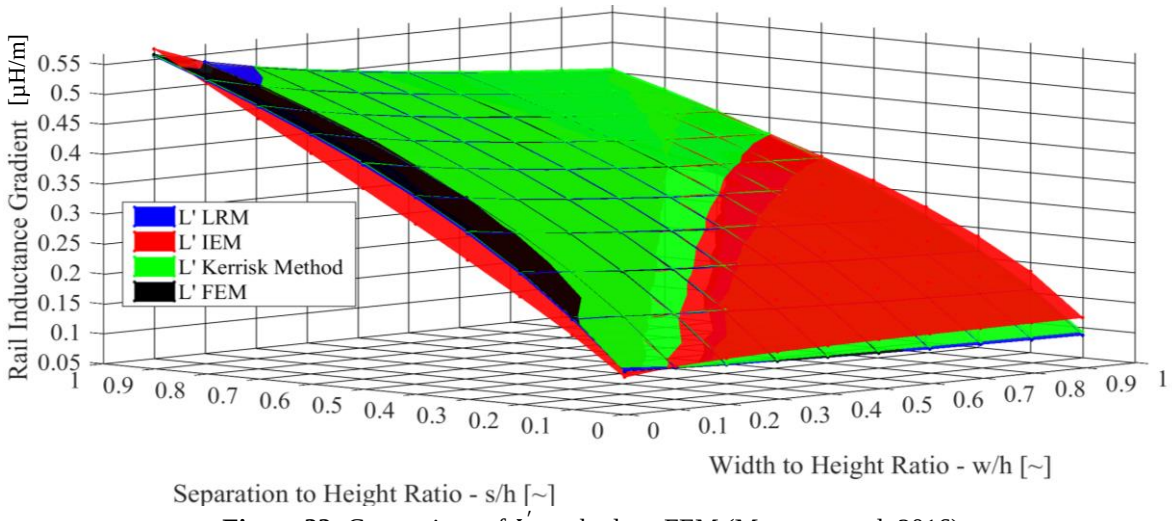

Figure 32: Comparison of $L^{'}$ methods to FEM (Murugan et al. 2016)

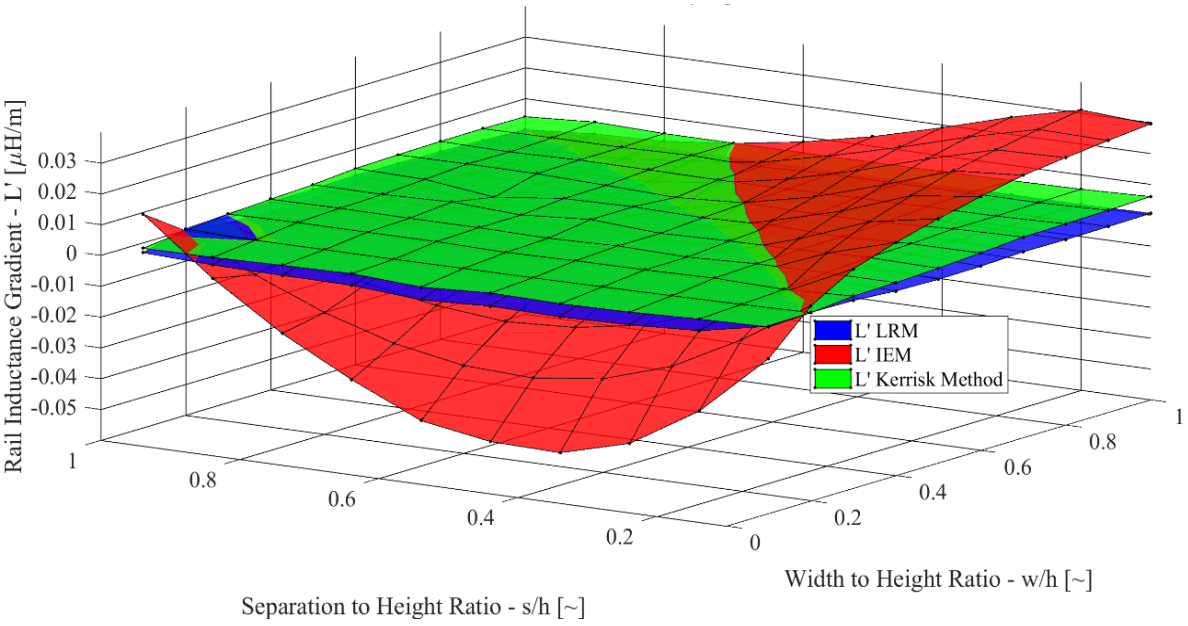

Figure 33: $L^{'}$ analytical method error vs. FEM (Murugan et al. 2016)

	LRM	IEM	Kerrisk Method
Average Error	0.276 %	3.068 %	0.718 %

Table 9: $L^{'}$ analytical method errors vs. FEM (Murugan et al. 2016)

A look at a broader range of s/h and w/h ratios is shown in Figure 34 and Figure 35. This shows some disagreement between the models, mainly at large s/h and low w/h, where the LRM gives a result of 1.59 μH/m, the Kerrisk method gives 1.41 μH/m, and IEM gives 11.0 μH/m.

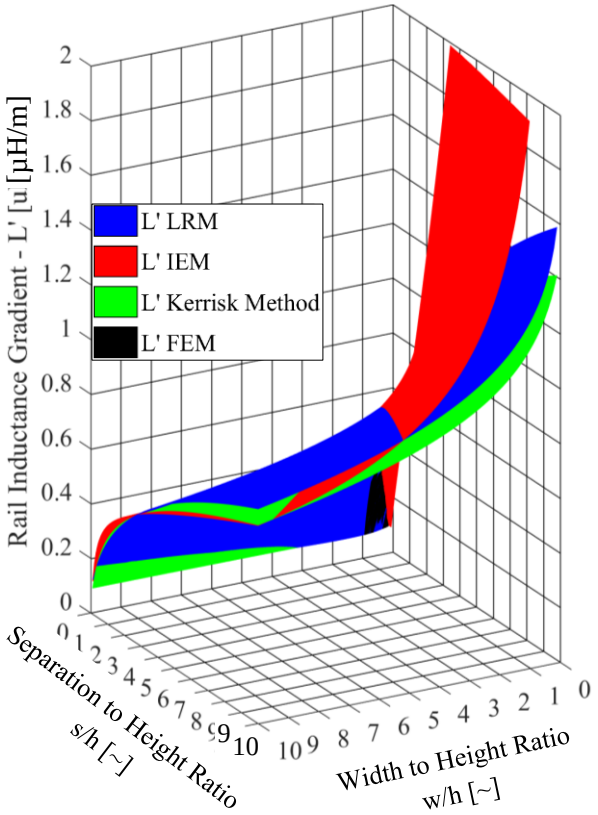

Figure 34: Broad comparison of L' methods

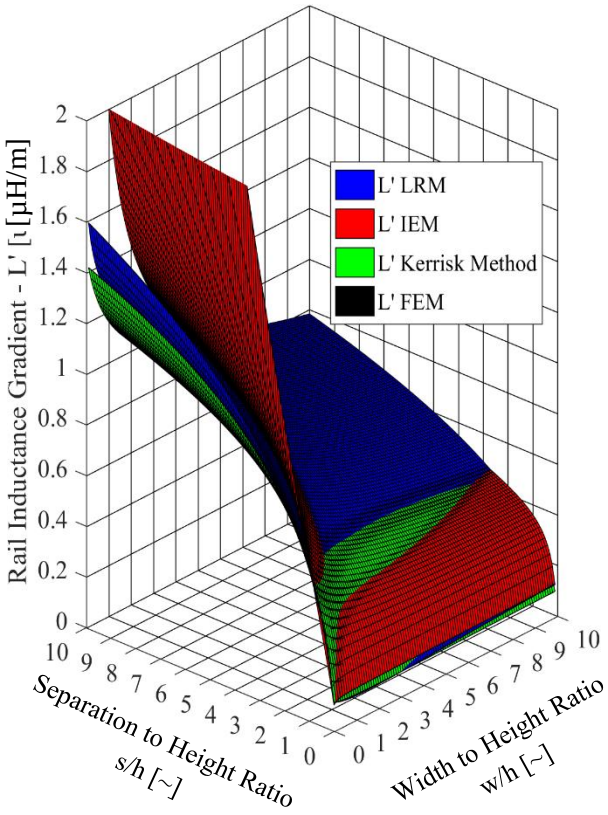

Figure 35: Broad comparison of L' methods

Overall, the IEM agrees well with both finite difference and LRM results when s/h and w/h are both high or both low. But when s/h is high and w/h is low, or when s/h is low and w/h is high there is significant disagreement between IEM and other methods. For these cases both LRM and the Kerrisk method agree well with finite element methods.

No other analytic method of computing L' for circular rails was found, so no comparison to other estimation methods is presented, though Murugan et al. do compare their results to their own FEM values. Other sources of L' values computed with FEM techniques were almost as scarce. In fact, only one data point was found (Bayati et al. 2012) which could be compared to (65). There do exist tabulated L' values

computed with FEM (shown in Figure 55 of Appendix B), but none could be found which used an opening angle of 10 or 40 degrees besides the values that the LRM equation was developed from. Thus, because simulating L' is outside of the scope of this investigation, no assessment of accuracy is provided here. Regardless, (65) represents an easy-to-use method of computing L' values without the need for a finite element model. This method has been compared to FEM values by its creators, and a very similar method was used to define the LRM for rectangular rails.

The obvious shortcoming of all these methods is that they are only valid for predetermined geometries, and while this is better than relying on tabulated values, designers interested in more complex geometries or more nuanced railgun methods will need to run their own simulations to compute L'.

This chapter presents four different methods of computing L' which have already been defined in readily applicable forms. Three of these methods are replicated (the Kerrisk method, IEM, and LRM), and compared to each other and finite element values. It has been determined that two of these methods (the Kerrisk method and the LRM) are more accurate than the other. Thus, when L' is calculated throughout this paper, it is done by averaging the Kerrisk and LRM results for a given geometry.

Chapter 6: Force Computation

The fundamental force behind railguns, and the main focus of this investigation, is the Lorentz force. It is suggested here that a method which computes force by directly approximating current distribution and magnetic field in the armature can provide more accurate force values than the traditional railgun force equation, while being more readily applicable than finite element computations. This hypothesis is tested by comparing the railgun force equation to five other approximations of railgun force with three finite element solutions from the literature, one set of experimental values from the literature, and one finite element solution defined here. A mesh refinement of this mid-complexity model is also presented. Regardless of which solution is more accurate, this review also inherently presents a brief look at the consistency of railgun force modeling.

The Lorentz force is generated by charge moving through a magnetic field, and its equation is shown here as (66). As is the case for all railgun parameters, the complete solution of (66) requires the computation of simultaneous partial differential equations to compute the current distribution (***J***) and magnetic field (***B***).

(66) $$F = \iiint_V \boldsymbol{J} \times \boldsymbol{B}\, \boldsymbol{dV}$$

Approximations have been made by Waindok and Piekielny (2016) in equations (67) and (68) and Xu and Geng (2010) in equation (70) on the following page which use the Biot-Savart law to compute magnetic field. The traditional railgun force equation is presented in (71).

(67) $$F = \int_0^{w_A} I(t) \cdot B\, dx = \int_0^{w_A} \frac{\mu_0 \cdot \mathrm{I(t)}^2}{4 \cdot \pi \cdot \mathrm{x}} \cdot \left(\frac{l}{\sqrt{l^2 + x^2}}\right) dx$$

(68) $$F = \frac{\mu_0 \cdot \mathrm{I(t)}^2}{4 \cdot \pi} \cdot \left(-2 \cdot ln\left(\frac{l+\sqrt{l^2+d^2}}{d}\right) + ln\left(\frac{l+\sqrt{l^2+\frac{w^2}{4}}}{\frac{w}{2}}\right) + ln\left(\frac{l+\sqrt{l^2+{w_A}^2}}{w_A}\right)\right)$$

$$where\ d = w_A + \frac{w}{2}$$

(69) $$G = 2 \cdot \frac{(\mathrm{x}+x')}{(\mathrm{y}-\mathrm{y}')^2+(\mathrm{x}+\mathrm{x}')^2} \cdot \left[\frac{\mathrm{z}}{\sqrt{(\mathrm{y}-\mathrm{y}')^2+(\mathrm{x}+\mathrm{x}')^2+z^2}} - \frac{\mathrm{z}-\mathrm{l}}{\sqrt{(\mathrm{y}-\mathrm{y}')^2+(\mathrm{x}+\mathrm{x}')^2+(\mathrm{z}-\mathrm{l})^2}}\right]$$

(70) $$\mathrm{F} = \frac{\mu_0}{2 \cdot \pi \cdot \mathrm{h}^2 \cdot \mathrm{w} \cdot \mathrm{t}_a} \int_{l}^{l+t_A} \int_{-\frac{h_A}{2}}^{\frac{h_A}{2}} \int_{0}^{w_A} \left(\int_{0}^{\mathrm{w}} \int_{-\frac{\mathrm{h}}{2}}^{\frac{\mathrm{h}}{2}} G \cdot \mathrm{I}(\mathrm{x},\mathrm{y},\mathrm{z},\mathrm{t})^2 \, \mathrm{dy}' \cdot \mathrm{dx}' \right) \cdot dx \cdot dy \cdot dz$$

(71) $$\mathrm{F} = \frac{L' \cdot I(t)^2}{2}$$

These approximations make the following assumptions:

- The current is distributed uniformly in the rails
    - This is a significant approximation for solid rails, as the B field between the rails is higher but becomes reasonably accurate for laminated rails (Xu and Geng 2010) (Xing et al. 2015).
- Force is only produced by the $\boldsymbol{B_y}$ component of the magnetic field
    - This assumption is reasonably accurate since the dominant component of the magnetic field between the rails points in the y direction (shown in Figure 36), though the Bx component is visibly non-zero near the top and bottom of the bore.

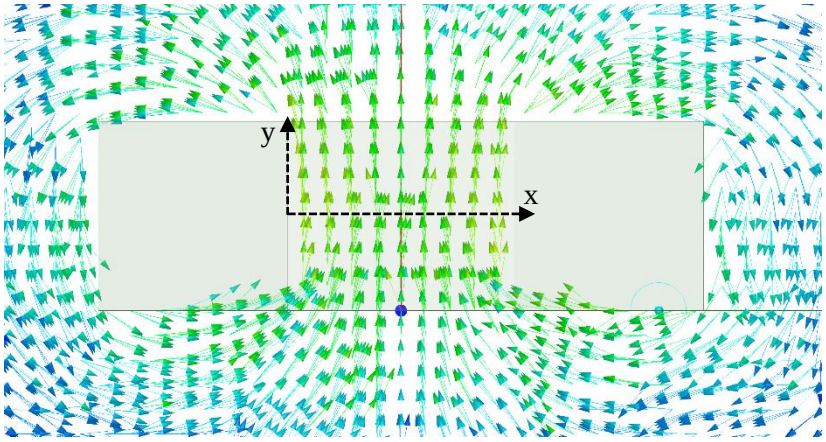

Figure 36: Magnetic field around rails as computed by ANSYS Maxwell 17.2

- The current moves perpendicular to the rail inner face at all points in the armature (similar to Figure 1 and Figure 9)
    - This assumption is fairly accurate for rectangular armatures (which is the only geometry modeled here) but falls apart for "C shaped" armatures (shown in Figure 38 and Figure 41). Even in rectangular armatures, the current does not turn instantly, as shown by Figure 37.

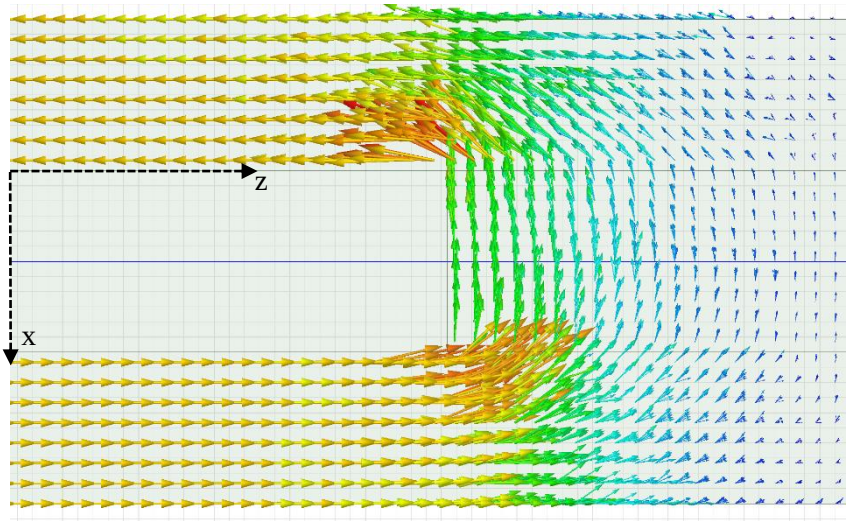

Figure 37: Current flow in rails and armature as computed by ANSYS Maxwell 17.2

The complexity of (66) → (70) comes from defining the magnetic field in the armature and accounting for the discretization of the armature and rail. Further explanation of the equations for magnetic field is presented in the magnetic field section. It should be restated that, as described in the magnetic field section, a factor of 2 was added to the magnetic field calculation to better match the B field with finite element results. This is shown in (70), where the denominator of the leading coefficient contains a factor of 2, rather than a factor of 4, as shown in (41). Further approximations have been made to produce the widely used and very simple "railgun force equation" (71) by utilizing the induction gradient (L') (Coffo 2011) (Behrens et al. 2003) (Ya-Dong et al. 2012) (Keshtkar 2005) (Keshtkar et al. 2009) (Murugan et al. 2016) (Keshtkar 2005) (Moghaddam et al. 2004) (Xu et al. 2014) (Schneider et al. 2009 pt.1) (Schneider et al. 2009 pt.2) (McCorkle and Bahder 2010) (He et al. 2010) (Chen et al. 2015). All of the methods presented here neglect aerodynamic drag.

The time dependent current is computed by (1) → (4) in the power supply section, and assumes that most railgun current profiles can be approximated by a sinusoidal rise, a constant maximum, and an exponential decay.

The frictional force used here is shown in (72), and relies on an approximate sliding friction coefficient computed experimentally by Chen et al of $\mu_f = 0.11$ (Chen et al. 2014) (Chen et al. 2015).

(72) $$F_f = \mu_f \cdot F_c = 0.11 \cdot (0.01 \cdot I) = 0.0011 \cdot I$$

Obviously in application this coefficient is dependent on the specific materials, surface smoothness, and surface treatments or lubricant used. The normal force is computed by assuming the "gram per amp" rule is followed as is done by Jin et al. (Jin et al. 2012) This rule, developed by Richard Marshall, specifies that one gram of mechanical preload (normal force from the armature on the rail) should be applied per amp of excitation current to maintain good electrical contact throughout launch, though this remains an area of active research (Brady 2005) (Chen et al. 2014). In the fourth comparison case considered below, a different formulation for F_C presented by Chen et al (2015) is used (73).

(73) $$F_C = \frac{L' \cdot I^2 \cdot d \cdot \theta_{ca}}{w_a}$$

This formulation is developed for a very specific armature shape (Figure 38), so it is not generally applicable, though it could be used to approximate F_C for C-shaped armatures. This would only be an approximation because most C armatures contact the rail along the whole length of the "legs", while the special armature considered below only contact the rail at the very end of the legs.

These force equations were solved and numerically integrated using an RK4 integration scheme in MATLAB. In this integration, the initial position of the armature must be set to some positive value to avoid numeric issues at l = 0. As stated before, the double integral over the rail cross-section (inside the parentheses in (70)) is computed using the "integral2" MATLAB function. The integral over the armature volume (outside the parentheses in (70)) is computed with the "trapz" MATLAB function.

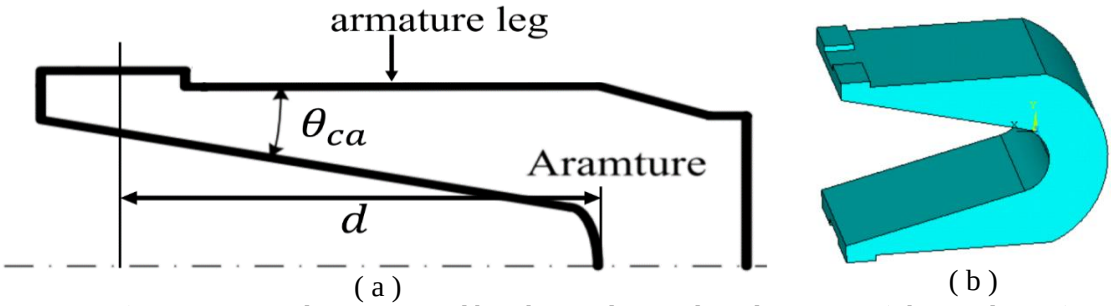

Figure 38: Special armature used by Chen et al. to study melt wear rate (Chen et al. 2015)

Six different solution methods examined in this chapter, and are described in Table 10. These models have been compared to experimental results and other models from the literature, including finite element solutions.

Method	Symbol	Description
Railgun Force	S1	Classical railgun force equation (71)
Waindok and Piekielny Force	S2	Direct force equation defined by Waindok and Piekielny (68)
Uniform Current Thick Rail	F1	Magnetic field computed in armature with thick rail method and multiplied by current density at each point. Current density is assumed uniform.
Uniform Current Thin Rail	F2	Magnetic field computed in armature with thin rail method and multiplied by current density at each point. Current density is assumed uniform.
Non-Uniform Current Thick Rail	F3	Magnetic field computed in armature with thick rail method and multiplied by current density at each point. Current density in armature takes skin effects into consideration. Current density in rail assumed uniform.
Non-Uniform Current Thin Rail	F4	Magnetic field computed in armature with thin rail method and multiplied by current density at each point. Current density in armature takes AC skin effects into consideration. Current density in rail assumed uniform.

Table 10: Description of force computation methods

Each comparison consists of a description of the initial method and findings, a description of the values used to attempt to replicate the results, a display of the results, and a discussion of the comparison. The first comparison (CC1) also includes ANSYS results made in this investigation and a rudimentary mesh refinement study of the F3 and F4 methods. The properties of each compared railgun will be presented in a table. Some of these comparisons required assumptions, and these are highlighted in grey. The inductance gradient in these tables has been computed by averaging the Kerrisk and LRM methods, this and other computed values are highlighted in yellow. Frictional effects are only considered when comparing to

experimental results, or other models which consider friction, as it is commonly neglected. When determining the current density in the armature, the SAC is used to find the skin depth (δ) and the CStSM is used to determine density (32).

6.1 Comparison Case 1 (CC1) : Waindok and Piekielny (2016) and ANSYS Maxwell

Waindok and Piekielny compare railguns with and without iron cores and permanent magnets to determine their improved efficacy. Their research also defines an analytic equation for simple railgun force (method S2), and compare this to a numerical solution obtained using ANSYS Maxwell. Both of these results for the three simple railgun cases presented by Waindok and Piekielny are compared to the models used here (Table 10). The values used for this railgun are shown in Table 5. The source article does not consider friction, so it is also neglected in the comparison analysis. The armature height had to be found by using the given mass, and assuming the armature is rectangular and made of aluminum $\left(2700\ \frac{kg}{m^3}\right)$. The source material only shows the force on the armature for certain applied excitation currents. Thus, the methods used here are only compared to these force values at specific currents, and no time-histories are presented. Essentially three different comparisons are made here, one between the methods developed here and the results from Waindok and Piekielny, one between these methods and an ANSYS Maxwell 17.2 model, and one between these methods computed with various mesh sizes. The results for the first two comparisons are shown in Table 12, and mesh refinement results are shown in Table 13.

Excitation Current [kA]	Force [N]	
	Analytic Equation **(Waindok and Piekielny 2016)**	ANSYS Maxwell **(Waindok and Piekielny 2016)**
20	110.75	130.6
10	27.7	32.65
1	0.28	0.33

Table 11: Results produced by Waindok and Piekielny for CC1 (Table 5)

Geometric Scale	Excitation Current [kA]	Force [N]						
		S1	S2	F1	F2	F3	F4	ANSYS
x0.1	**20**	100.04	97.721	49.567	52.620	49.003	52.046	90.281
x0.25	**20**	100.04	97.721	49.567	52.620	58.663	62.288	89.77
x0.5	**20**	100.04	97.721	49.567	52.620	71.788	76.057	89.755
x0.75	**20**	100.04	97.721	49.567	52.620	80.254	84.749	90.981
x1	**1**	0.25	0.24	0.12	0.13	0.21	0.22	0.2249
x1	**10**	25.01	24.43	12.39	13.15	21.28	22.39	22.44
x1	**20**	100.04	97.72	49.57	52.62	85.12	89.57	89.953
x1	**50**	625.27	610.76	309.79	328.87	532.02	559.80	562.21
x1	**100**	2501.1	2443.0	1239.2	1315.5	2128.1	2239.2	2248.8
x2	**20**	100.04	97.721	49.567	52.620	89.904	93.399	90.694
x3	**20**	100.04	97.721	49.567	52.620	89.265	92.002	89.436
x4	**20**	100.04	97.721	49.567	52.620	88.455	90.777	88.286
x5	**20**	100.04	97.721	49.567	52.620	87.963	90.075	85.23
x10	**20**	100.04	97.721	49.567	52.620	87.465	89.382	87.479
Average Error	**vs. Analytic**	-23.70%	-25.90%	-62.60%	-60.00%	-35.30%	-32.10%	-19.15%
	vs. ANSYS	-10.00%	-12.60%	-55.90%	-52.90%	-23.80%	-19.90%	-31.42%
	vs. ANSYS	11.94%	9.21%	-44.66%	-41.17%	-9.84%	-5.87%	~

Table 12: CC1 Results found at l = 0.1704 m with grid elements 0.6 mm x 0.5 mm x 2.96 mm large (h_a x w_a x t_a) at the x1 scale. Green highlights are compared to the Waindok and Piekielny (2016) results.

Geometric Scale	Excitation Current [kA]	Force [N] for different numbers of armature divisions (w_a x h_a x t_a)						ANSYS
		40 x 40 x 20		60 x 60 x 30		80 x 80 x 40		
		F3	F4	F3	F4	F3	F4	
x0.1	**20**	52.268	55.757	53.516	57.132	54.170	57.845	90.281
x0.25	**20**	62.698	66.938	64.311	68.729	65.168	69.667	89.77
x0.5	**20**	77.808	83.039	80.360	85.879	81.743	87.397	89.755
x0.75	**20**	88.595	94.398	92.321	98.539	94.378	100.795	90.981
x1	**1**	0.239	0.254	0.251	0.268	0.258	0.275	0.22488
x1	**10**	23.890	25.400	25.120	26.764	25.813	27.523	22.44
x1	**20**	95.561	101.599	100.481	107.057	103.253	110.090	89.953
x1	**50**	597.254	634.993	628.007	669.104	645.330	688.065	562.21
x1	**100**	2389.016	2539.971	2512.028	2676.417	2581.320	2752.262	2248.8
x2	**20**	104.426	109.985	112.964	119.396	118.203	125.092	90.694
x3	**20**	103.418	108.069	113.661	119.314	120.513	126.731	89.436
x4	**20**	100.669	104.561	111.312	116.217	119.065	124.582	88.286
x5	**20**	98.000	101.328	108.265	112.551	116.392	121.301	85.23
x10	**20**	91.363	93.540	96.951	99.620	103.364	106.494	87.479
Average Error	**vs. Analytic**	-14.05%	-8.62%	-9.62%	-3.71%	-7.13%	-0.98%	-19.15%
	vs. ANSYS	-27.09%	-22.48%	-23.33%	-18.32%	-21.22%	-16.00%	-31.42%
	vs. ANSYS	0.53%	6.00%	6.88%	12.98%	11.16%	17.63%	~

Table 13: Mesh refinement assessment done at l = 0.1704 m with grid element sizes varying from 0.3 mm x 0.25 mm x 1.48 mm to 0.15 mm x 0.125 mm x 0.74 mm. Green highlights are compared to the Waindok and Piekielny (2016) results.

The comparison to the Waindok and Piekielny results was surprising, since the model pulled from this paper (S2) did not match up with their analytic results. In the source article, the FEM results show that the armature force does not vary significantly (if at all) with armature position. However, it can be seen just by inspection of (68) that changes in l will impact the armature force with method S2. This may be responsible for some of this variation, since the armature position is not stated in the source material (using l = 0.1704 depends on an assumption that the armature is about to leave the rails). But force increases with armature position using method S2, and even with the armature at the rail end (l = 0.2 m) the 20 kA force would be 97.90 N, not 110.75 N. Regardless of the agreement between the two results, it is concluded that the significant position dependent variation in force suggested by this formulation is erroneous, since the ANSYS results from Waindok and Piekielny, and the LS-DYNA results from Jin et al. (in CC3 below) show very little change with position. It should be mentioned that this does not only occur in the S2 formulation. In fact all of the methods presented here besides the simple railgun force equation (S1) show some of this behavior mainly visible in Figure 43 (b).

Another possible explanation of the disagreement could be that the armature and rail heights used here are different than the original analysis. However, armature and rail height do not show up in the S2 force equation (68) so any incorrect assumption of these values should not impact this specific result. Lastly, the ANSYS Maxwell 17.2 results calculated in this assessment match models S1-S4 much better than the ANSYS Maxwell 14.0 results from the source article. This further suggests some yet unconsidered difference between the two models, as one would expect the two finite element models to produce results that have less than ~30% error.

The quantitative results of this comparison are shown in the rows highlighted in green in Table 12. The average errors for S1→F4 are relative to the results shown in Table 11 and Table 12, and only use the values corresponding to the cases shown in Table 11 (scale of x1 and excitation current of 20, 10, and 1kA).

The ANSYS results referenced in Table 12 and Table 13 are computed using the model setup shown in Figure 39 with the magnetostatic solver in ANSYS Maxwell 17.2. The current excitation is applied in a way similar to the FEMM model in Figure 21, where an inlet and outlet current is specified at the rear face of each rail. A B = 0 boundary is applied along the walls of a cylindrical region around the rails. This region is coincident with the rail rear and front faces. The model uses an adaptive mesh of tetrahedral elements with an average edge length of ~ 0.15 mm. The values used in these tables are the F_y force components, which are by far dominant over the other two (the F_x components are ~ 0.2% of F_y, and the F_z components are ~ 0.02% of F_y).

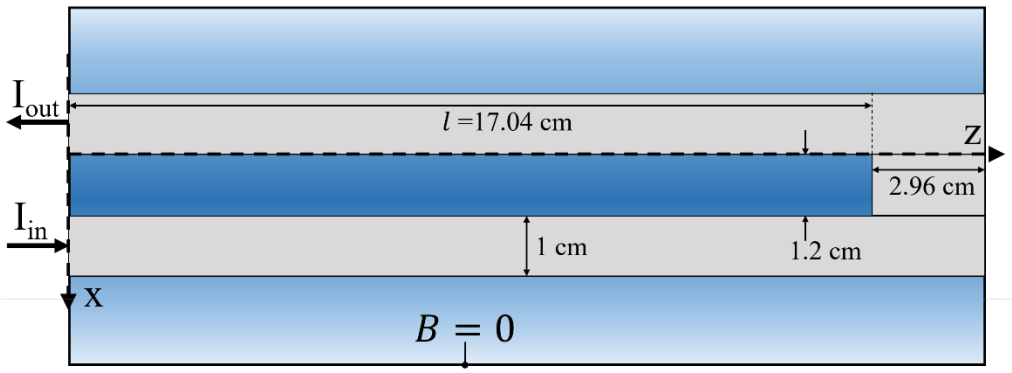

Figure 39: Setup for the ANSYS Maxwell 17.2 Lorentz force model

Models S1, S2, F3, and F4 show good agreement with the ANSYS Maxwell 17.2 results. The F1 and F2 results significantly underestimate the force. This makes sense because these cases do not consider the high current density along the armature rear face, meaning much of the current is considered to flow through a region which has small B field, and thus creates less force than other methods. It is worth noting that the simple methods (S1 and S2) perform similarly to the more complex ones (F3 and F4). These simpler methods do not change with geometric scale, which is not inaccurate as the ANSYS results are fairly constant with scale change as well. The more complex models mirror this for larger scales, but suffer some issues with smaller geometries. This could not be readily explained, and is the reason a mesh refinement study was done on these two models (Table 13). The F4 model, despite relying on the thin rail assumption has a smaller average error than the F3 model which uses the more accurate thick rail method of finding B. It seems that this is due to a general underestimate by both methods, and the thin rail model

happens to find larger overall values than the thick rail model. This is not always the case, as F4 overestimates the ANSYS results in the x2 to x10 scale models.

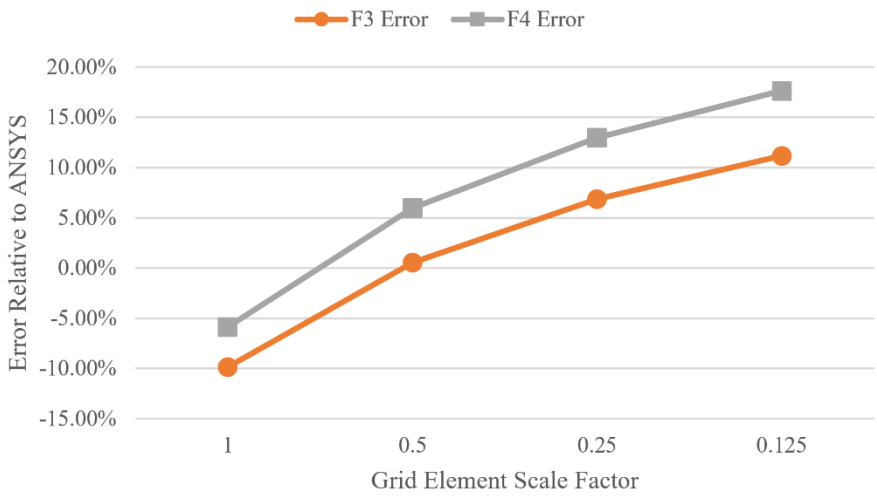

Figure 40: Method F3 and F4 error relative to the ANSYS Maxwell 17.2 results for grid element sizes varying from 0.3 mm x 0.25 mm x 1.48 mm to 0.15 mm x 0.125 mm x 0.74 mm

This mesh refinement assessment reveals an alarming relationship between number of grid elements and computed force where more grid elements (smaller grid element size) corresponds to higher force. For the size of elements considered here, no leveling off of this effect can be seen (Figure 40).

Though the total amount of current (computed with (34)) remains equal to the excitation current regardless of element size, the average current density increases with the number of elements. Some further investigation showed the decrease in element size in the z direction to be responsible for most of this increase, with x direction size making up the rest of the increase. This seems to suggest numeric issues related to the concentration of current density points along the armature rear face, though the exact mechanism of this could not be determined. Resolving this issue represents the most significant objective of any future work. The first steps in this would be to compare element size to the armature skin depth, and further reduce the mesh size. As Figure 40 shows, the error does seem to curve, and may level off for even smaller meshes. It should be mentioned that run times get prohibitively long for F3 using such meshes. The run time for this analysis was 4.3 s and 0.24 s for F3 and F4 respectively with a grid element scale factor of 1 and 291 s and 0.290 s for F3 and F4 respectively with a scale factor of 0.125. This demonstrates the

computational load that accompanies the "integral2" computation. However, if the worst case is true (that the force result is simply arbitrary relative to the number of elements used) then it is unlikely that these equations will produce reliably accurate results across multiple cases. This provides further motivation for the following force comparison cases.

6.2 Comparison Case 2 (CC2) : Chengxue et al. (2014)

Physical Parameters	Symbol	Value	Value	Symbol	Electrical Parameters
Rail Length [m]	L	1	1→5	I_P	**Peak Current [100,000 A]**
Rail Separation [m]	s	0.02	0.5	t_1	**Current Profile Rise Time [ms]**
Rail Width [m]	w	0.006	1.7	t_2	**Current Profile Decline Time [ms]**
Rail Height [m]	h	0.02	3.0	t_3	**Current Profile Total Time [ms]**
Inductance Gradient [μH/m]	L'	0.52	Value	Symbol	Material Parameters
Armature Width [m]	w_a	0.02	Cu	~	**Rail Material [~]**
Armature Height [m]	h_a	0.02	Al	~	**Armature Material [~]**
Armature Thickness [m]	t_a	0.01	$4\ E^{-8}$	ρ	**Armature Resistivity [Ω·m]**
Armature Mass [kg]	m	0.2599			
Initial Velocity [m/s]	V_0	0			

Table 14: Railgun parameters for comparison case 2 (CC2) (Chengxue et al. 2014)

Chengxue et al. also utilize ANSYS to perform a FEM simulation of railgun armature force and heating. While a current profile is shown, no mention of final velocity is provided in this source material. Railgun armature force is instead provided for different excitation currents again, so a comparison similar to that of CC1 is provided here. Chengxue et al. use a popular C armature geometry (shown in Figure 41) which is not supported by the models used here. It is approximated by a rectangular armature which has its edges delineated by the contact patch of the C armature with the rails. The railgun properties used here are shown in Table 14. The original article ignores the frictional force, and so does this comparison. The armature mass was obtained using the volume of the C armature and the density of aluminum $\left(2700\ \frac{kg}{m^3}\right)$.

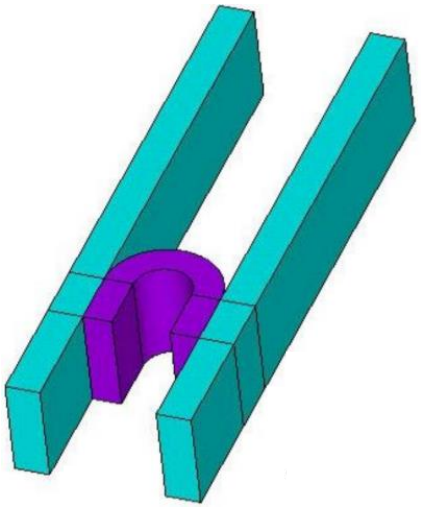

Figure 41: C armature illustration (Chengxue et al. 2014)

Results from this comparison are shown in Table 15, and favor the simpler S2 method.

Excitation Current [kA]	Force [kN]						
	ANSYS (Chengxue et al. 2014)	S1	S2	F1	F2	F3	F4
500	171.9	65.016	101.837	78.977	86.836	77.703	85.739
400	69.2	41.61	65.175	50.545	55.575	49.731	54.873
300	26.7	23.406	36.661	28.432	31.261	27.973	30.866
200	12.62	10.402	16.294	12.636	13.894	12.433	13.718
100	7.12	2.601	4.074	3.159	3.473	3.108	3.429
Average Error		-39.09%	-4.59%	-26.01%	-18.64%	-27.20%	-19.67%

Table 15: CC2 Results computed at l = 0.99 m with grid elements 1 mm x 1 mm x 0.5 mm in size

The other methods stay reasonably close, but do underestimate force in this scenario. Part of this could be due to the C shaped armature, which can obtain higher force than rectangular armatures by extending the active magnetic space between the rails by taking advantage of the current flowing through the armature "legs". A study by Bayati et al. (2015) on the specifics of this C shape have determined that longer legs produce more force at the cost of higher maximum current density (and thus more ohmic heating).

The difference between considering uniform current distribution in the armature and not (F1 and F2 vs. F3 and F4) is much less significant in this comparison than CC1. The last comparison used a very thick armature compared to this one, meaning a uniform current distribution would pull much more current away from the high B field area of the armature. Since this case uses a significantly thinner armature, a uniform distribution is less consequential.

6.3 Comparison Case 3 (CC3) : Jin et al. (2015)

Physical Parameters	Symbol	Value	Value	Symbol	Electrical Parameters
Rail Length [m]	L	0.3	700	I_P	**Peak Current [kA]**
Rail Separation [m]	s	0.05	0.1	t_1	**Current Profile Rise Time [ms]**
Rail Width [m]	w	0.01	0.4	t_2	**Current Profile Decline Time [ms]**
Rail Height [m]	h	0.04	0.8	t_3	**Current Profile Total Time [ms]**
Inductance Gradient [μH/m]	L'	0.5956	Value	Symbol	Material Parameters
Armature Width [m]	w_a	0.05	Cu	~	**Rail Material [~]**
Armature Height [m]	h_a	0.02	Al	~	**Armature Material [~]**
Armature Thickness [m]	t_a	0.03	$4\ E^{-8}$	ρ_a	**Armature Resistivity [Ω·m]**
Armature Mass [g]	m	50.134	$1.77\ E^{-8}$	ρ_r	**Rail Resistivity [Ω·m]**
Initial Velocity [m/s]	V_0	0			

Table 16: Railgun parameters for comparison case 3 (CC3) (Jin et al. 2015)

Jin et al. assessed how changing the curvature of the rail inner face would impact the phenomena of critical velocity. Critical velocity is the armature velocity which will excite resonance in the rails, causing significant stress and strain in them, and potentially causing damage. It was concluded that increasing the rail moment of inertia (by changing the curvature of the rail inner face) produces only limited improvements, increasing critical velocity in one case from 937 m/s to 1005 and 1004 m/s depending on if the rail was convex or concave. Flat rails had the highest L' (and thus highest efficiency), followed by convex then concave rails. Convex rails showed improvement (decrease) in current density on the rail surface, but higher current density along the armature contact, particularly at the armature trailing edge. Jin et al. provide the first time-history that could be compared against using LS-DYNA. The current profile used in their analysis (Figure 42) is, followed exactly due to its linear nature. A good number of the geometric properties needed to be assumed because they were not directly presented in the source article. A "cross-sectional dimension" of 40mm x 50mm is referenced, and this is taken to mean the rail height is 40 mm (as stated elsewhere) and the rail separation is 50 mm. Figures are also shown which visually make this seem reasonable but it could not be confirmed.

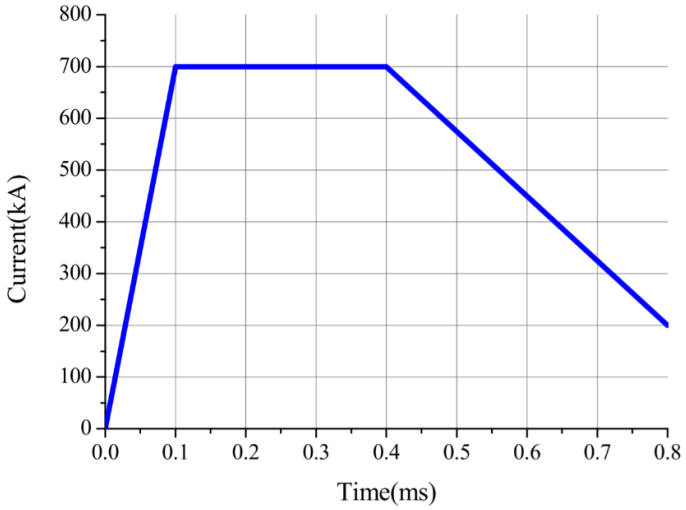

Figure 42: CC3 current profile (Jin et al. 2015)

These figures are the only source of information on the armature height. The time-integrated results of methods S1→F4 have been overlaid on the source acceleration, velocity, and position time-histories, and are shown in Figure 43.

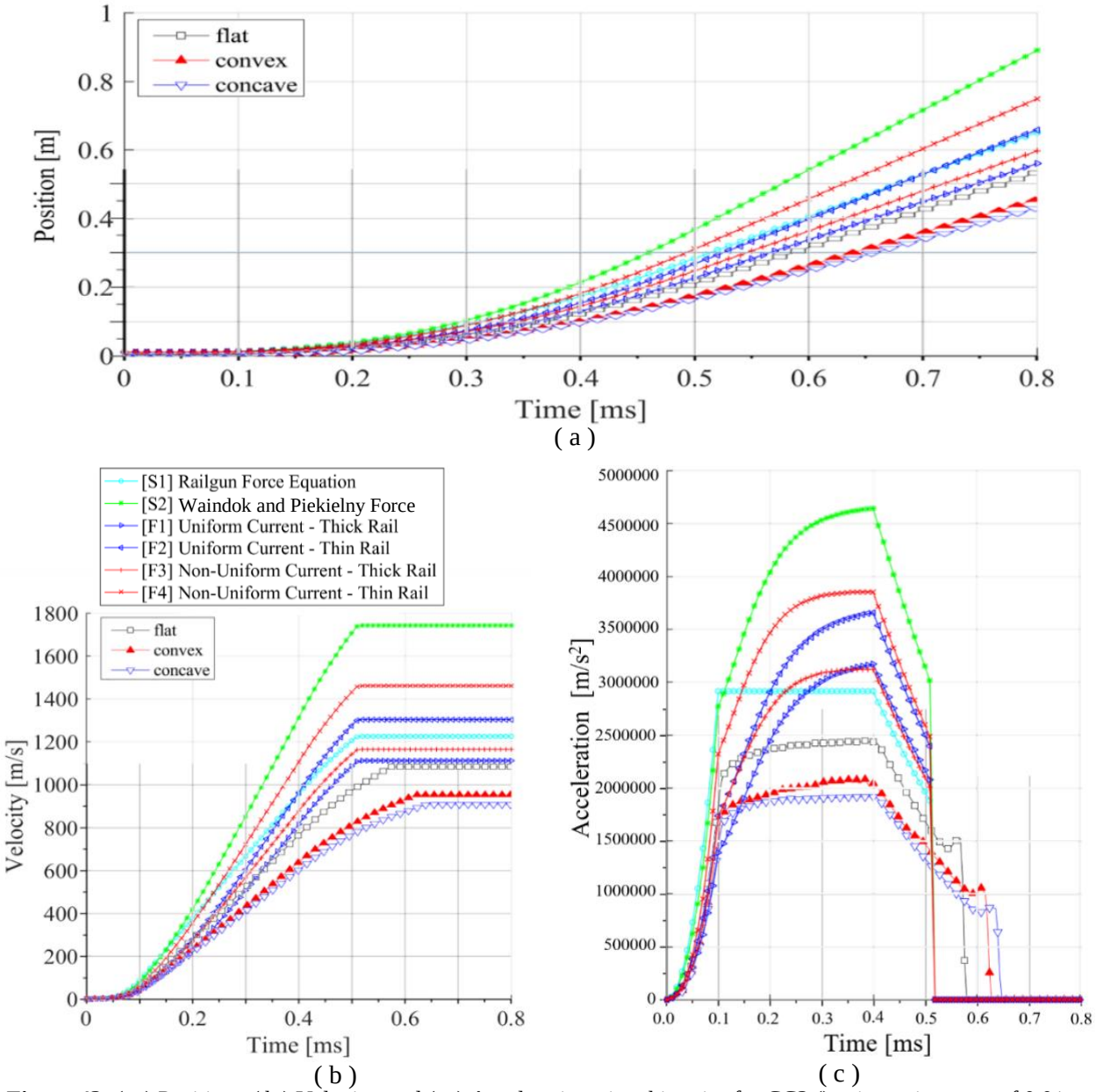

Figure 43: (a) Position, (b) Velocity, and (c) Acceleration time histories for CC3 () using a time step of 0.01 ms and grid elements 1 mm x 2.5 mm x 3 mm in size for models S1→F4. These are overlaid onto the same results from Jin et al. The legend applies to both plots. Uses an initial position of 0.01 m and initial velocity of 0 m/s.

Final velocities and maximum forces are compared in Table 17. Both the final velocity and the maximum force from the source article were obtained by reading the graphs. For the force, the peak value of the acceleration graph was read and multiplied by the armature mass.

	LS-DYNA (Jin et al. 2015)	S1	S2	F1	F2	F3	F4
Maximum Force [kN]	122.83	145.911	234.001	161.082	185.502	168.842	209.015
Force Error	~	18.79%	90.51%	31.14%	51.02%	37.46%	70.17%
Final Velocity [m/s]	1090	1225.76	1742.77	1143.981	1303.27	1164.79	1461.1
Velocity Error	~	12.46%	59.89%	4.95%	19.57%	6.86%	34.05%

Table 17: CC3 Results, force computed at l = 0.27 m and maximum current – grid elements 1 mm x 2.5 mm x 3 mm in size

Unlike the previous comparisons, the S2 method performs the worst in this case, significantly overestimating the LS-DYNA results from the source material, though this does maintain the trend that S2 produces a generally higher result than other methods. Also in keeping with previous trends, the thin rail methods (F2 and F4) produce larger results than the thick rail methods. In this case the effect is much more pronounced than the previous two. Interestingly, the best agreement in this case comes from the simple railgun equation, in both force and velocity. The S1, F1, and F3 methods agree with LS-DYNA final velocity well, but have significant errors in maximum force computation. The F1 and F3 methods get the closest to approximating final velocity correctly, but have much higher maximum force errors than the S1 method. This occurs because of the erroneous position dependence mentioned in the CC1 discussion. The input current is constant between 0.1 and 0.4 ms, however methods S2→F4 all gradually approach their maximum during this time, rather than holding constant like the S1 method (and the LS-DYNA results).

6.4 Comparison Case 4 (CC4) : Chen et al. (Chen 2015)

Physical Parameters	Symbol	Value	Value	Symbol	Electrical Parameters
Rail Length [m]	L	2	~	I_P	**Peak Current [kA]**
Rail Separation [m]	s	0.02	1.2	t_1	**Current Profile Rise Time [ms]**
Rail Width [m]	w	0.02	~	t_2	**Current Profile Decline Time [ms]**
Rail Height [m]	h	0.02	4.25	t_3	**Current Profile Total Time [ms]**
Inductance Gradient [μH/m]	L'	0.454	Value	Symbol	Material Parameters
Armature Width [m]	w_a	0.02	Cu	~	**Rail Material [~]**
Armature Height [m]	h_a	0.02	Al	~	**Armature Material [~]**
Armature Thickness [m]	t_a	0.005	$4\ E^{-8}$	ρ_a	**Armature Resistivity [Ω·m]**
Armature Mass [kg]	m	0.0192	$1.77\ E^{-8}$	ρ_r	**Rail Resistivity [Ω·m]**
Initial Velocity [m/s]	V_0	0			

Table 18: Parameters for the Chen et al. railgun (2015) where the time values are shown for experiment set A

Chen et al. performed and presented at least 19 experimental railgun shots in order to investigate the rate of wear and the effects of loading on armatures designed to make melt wear their only wear mechanism. Their investigation provided the approximate friction coefficient ($\mu_f = 0.11$) used here, values for contact resistance of some armatures, the wear rate of these armatures, and experimental velocity data. The specially designed armatures used by Chen et al. have small "feet" along the armature-rail interface which are intended to melt and wear down during the shot in order to more accurately measure the melt wear rate of armatures. One of these is shown in Figure 38 (b), and it can be seen that this is a "C" armature meaning there will be some discrepancy in modeling, as this geometry is not supported by the models developed here. It is assumed that the closest rectangular geometry is made by defining the thickness of the rectangular armature as the thickness of the contact feet. The data for this case was used before in the magnetic field section, but is replicated here in Table 18, and includes the dimensions of the rectangular armature used here. Since this was an experimental case, friction is considered in this analysis with the contact force defined by (73). For this case, $\theta_{ca} = 20°$ and $d = 0.0225\ m$.

Two sets of experiments were performed by Chen et al., and each used a different excitation current profile shape. As such, the original current profile recorded by Chen et al., and the current profile shapes used here are shown for both cases in Figure 44.

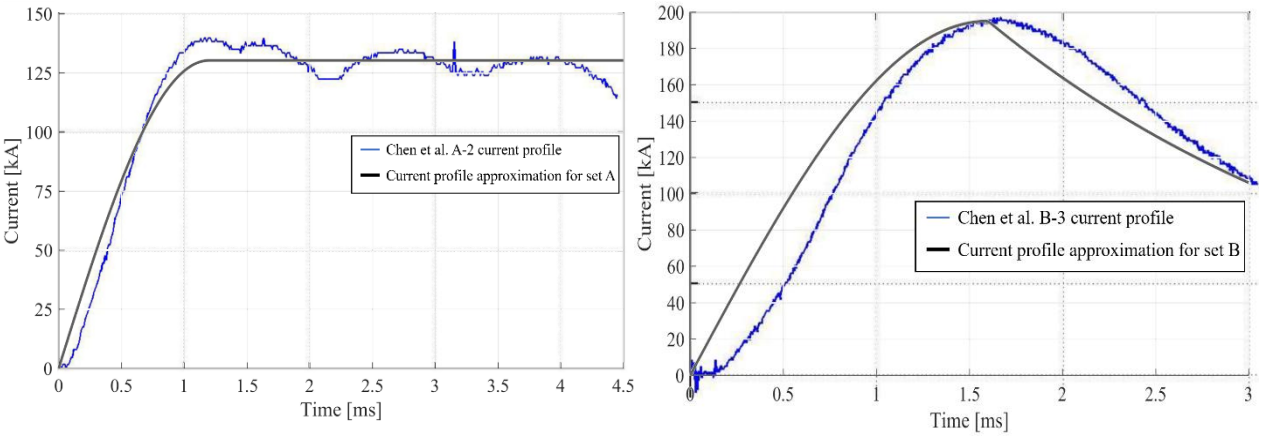

(a) (b)

Figure 44: Recorded current profile for (a) shot A-2 and (b) shot B-3 from Chen et al. (2015) overlaid with the approximated current profile used for each case in this analysis

While each set followed a general current profile, the magnitude and specific shape of each recorded profile is different, with maximum currents ranging from 112 to 240 kA. Since each profile is not presented, it is impossible to specify each profile precisely. However, general rules can be applied to the maximum currents to approximate each profile. From the profiles provided, it was determined that for the first set of experiments (set A) could be approximated as having a rise time of about 1.2 ms and holding constant at 92% of the maximum current until 4.5 ms. Only one profile from set *B* was presented. The maximum in this profile seemed to be accurate, the rise time was read as 1.6 ms, and the falloff is modeled as an exponential decrease which drops to 54% of the maximum current.

The results from this comparison are shown in Table 19 and Table 20 on the following pages. The results from the simulation models match the experimental velocity values with reasonable accurracy. The worst errors come from the F1 and F2 cases, with average errors ~120% for set A and ~50% for set B. Maximum errors for these cases reach over 200% in set A. Such overestimation is strange for these models, as they do not consider the current concentration along the armature rear face. This model has a very thin armature, so this effect is smaller than in most cases. But that still does not explain these models producing

higher force estimations than the F3 and F4 methods. The most complex cases have average errors around 68% for set A and under 20% for set B. The simple cases surprisingly perform the best, with errors around 40% for set A and 8% for set B. The relatively low values for S2 are inconsistent with earlier results that showed S2 predicting larger forces than the other methods.

Case	Excitation Current [kA]	Measured Velocity [m/s]	Computed Velocity [m/s]					
			S1	S2	F1	F2	F3	F4
A-1	128.8	520.8	638.3716	589.1806	958.6632	1012.714	735.5076	752.5738
A-2	128.8	543.5	638.3716	589.1806	958.6632	1012.714	735.5076	752.5738
A-3	138	500	732.8245	678.9103	1104.612	1166.914	836.2789	854.8925
A-4	139.84	450	752.4968	697.6106	1135.029	1199.051	857.0475	875.9712
A-5	151.8	543.5	863.5261	802.8323	1309.561	1383.755	973.0506	993.7328
A-6	103.04	378.8	408.5578	371.4427	604.5402	638.5568	481.7469	494.4985
A-7	103.04	297.6	325.6998	293.2866	477.4459	504.267	386.6123	397.5235
A-8	117.76	357	533.6266	489.8115	797.0445	841.9542	621.5017	636.7158
A-9	128.8	312.5	638.3716	589.1806	958.6632	1012.714	735.5076	752.5738
A-10	128.8	430	638.3716	589.1806	958.6632	1012.714	735.5076	752.5738
A-11	128.8	431	638.3716	589.1806	958.6632	1012.714	735.5076	752.5738
	Minimum Error		7.86%	1.45%	59.59%	68.57%	27.18%	30.54%
	Average Error		43.67%	32.99%	115.45%	127.60%	65.59%	69.49%
	Standard Deviation		28.51%	26.08%	43.81%	46.29%	31.71%	32.30%
	Maximum Error		104.28%	88.54%	206.77%	224.07%	135.36%	140.82%

Table 19: Comparison of the set A experiments from Chen et al. to force model results. Armature initial position set to 0.01 m and initial velocity set to 0 m/s. Grid element size and time step set to 1 mm x 1 mm x 0.5 mm and 0.5 ms respectively. Excitation current values shown are the result of multiplying the maximum current provided by Chen et al. by 0.92.

Since this comparison is done with experimental results, there are a number of factors that might be responsible for the errors seen here, and it remains possible that the good performance of the simple results is only by chance. First of all, none of the models here account for aerodynamic drag. An approximate drag calculation has been done using a drag coefficient of 1.28 (standard for a flat plate), standard air density, a velocity of 500 m/s, and the cross-sectional area of 0.02 m x 0.02 m gives force of 78.4 N. Since the applied force is around a few kN, this should not have a large impact on the final velocity, though it would serve to reduce the modeled velocity where the models consistently overpredict the experimental results.

Case	Excitation Current [kA]	Measured Velocity [m/s]	Computed Velocity [m/s]					
			S1	S2	F1	F2	F3	F4
B-1	180	480.8	490.1718	445.0704	724.0297	764.8901	569.114	583.4028
B-2	200	568	605.1504	554.0987	901.3553	952.2457	695.4525	711.8522
B-3	195	520.8	575.2711	525.7449	855.2383	903.5207	662.931	678.8026
B-5	210	625	667.1783	612.9976	997.1565	1053.464	762.3273	779.7844
B-6	200	568.2	605.1504	554.0987	901.3553	952.2457	695.4525	711.8522
B-7	155	403	363.4684	325.2676	529.2124	559.0434	425.7359	437.3904
B-8	150	417	340.3971	303.5113	493.8393	521.6656	399.0935	410.2216
		Minimum Error	1.95%	0.95%	18.43%	25.10%	4.29%	1.63%
		Average Error	8.63%	8.82%	48.77%	57.17%	17.49%	19.60%
		Standard Deviation	5.11%	10.33%	17.22%	18.20%	8.94%	10.45%
		Maximum Error	18.37%	27.22%	64.22%	73.49%	27.29%	30.34%

Table 20: Comparison of the set *B* experiments from Chen et al. to force model results. Armature initial position set to 0.01 m and initial velocity set to 0 m/s. Grid element size and time step set to 1 mm x 1 mm x 0.5 mm and 0.5 ms respectively. Excitation current values shown are the result of multiplying the maximum current provided by Chen et al. by 0.92.

Additionally, the approximated current profiles (for case A in particular) likely have some significant errors. The current profiles are nominally constant, but it can be seen in Figure 44 that the current drops thorughout the shot. For the purposes of this analysis, these drops and their magnitude are random since they are not predictable from the data given. Here, the profile is approximated by multiplying the maximum current by a factor of 92% to account for these drops. But this is only an approximation, and it is possible that further drops (or the lack of them) change the profile significantly. This would produce significant error, as the drops in Figure 44 can be 20 kA in magnitude, and can produce significantly less current. This type of significant variation is known to happen, as multiple cases using the same maximum current produce different final velocities in the experimental data. Shots A-1, A-2, A-9, A-10, and A-11 all have a maximum current of 140 kA, but produce velocities varying from 312.5 to 520.8 m/s. This error is somewhat random, as it is possible for these drops to not occur. But for shot A-2 the approximated profile matches fairly well, and shots A-9, A-10, and A-11 (which use the same profile) have final experimental velocities of 312.5, 430, and 431 respectively. These are some of the shots responsible for the most error, and shot A-9 is the soruce of the maximum error for all methods. It then seems likely that this factor generally serves to produce higher modeled velocity and lower experimental velocity. This idea is supported

by the fact that the set B results have significantly smaller errors, and the current profile definition has less ambiguity. In contrast to set A, two shots from set B which use the same maximum excitation current have nearly the exact same final velocity. One set of example time histories from set B (shot B-8) is shown in Figure 45.

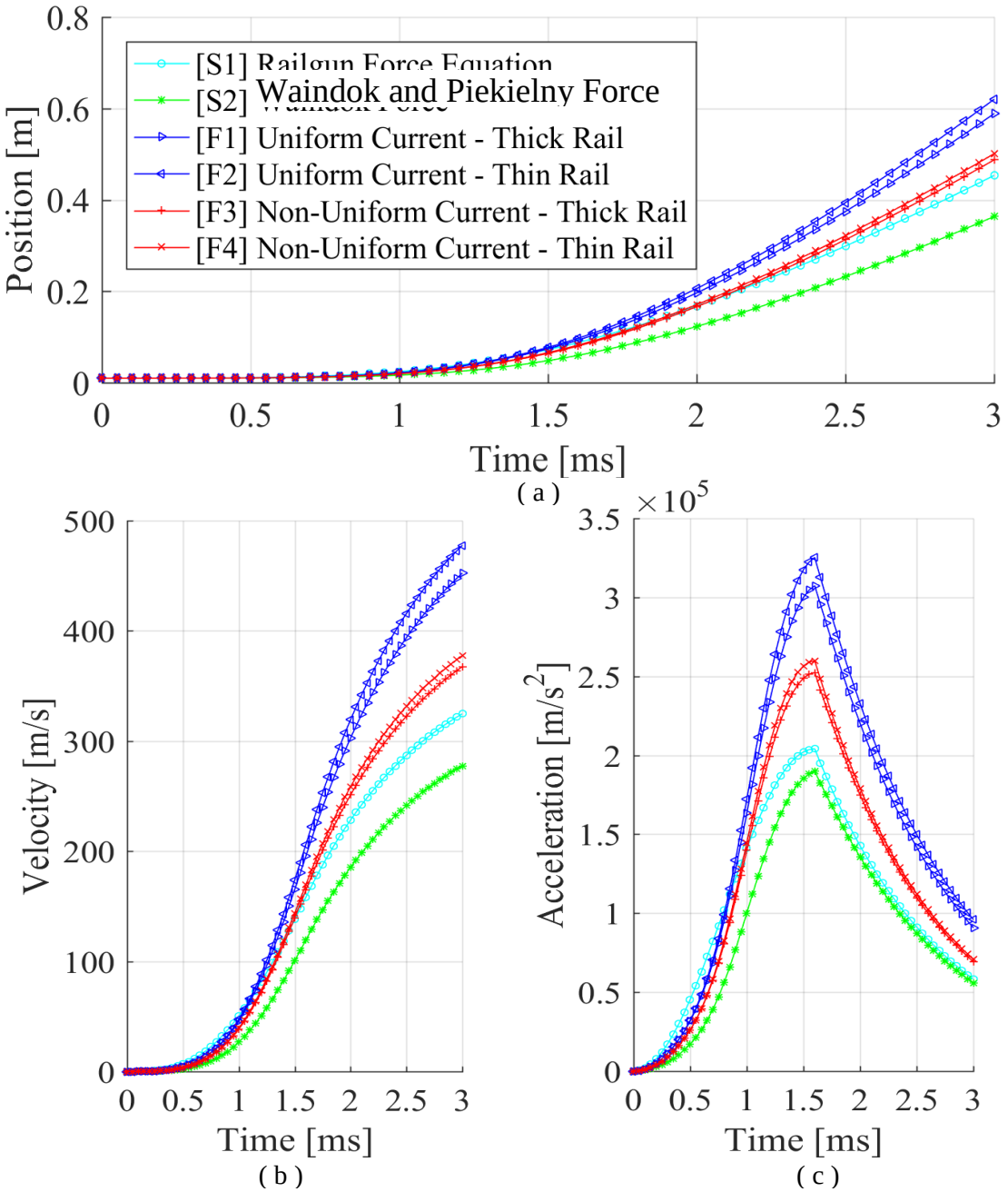

Figure 45: (a) Position, (b) Velocity, and (c) Acceleration time histories for CC4 (Figure 17) shot B-8 using a time step of 0.01 ms and grid elements 1 mm x 2.5 mm x 3 mm in size for models S1→F4. Initial position is set to 0.01 m and initial velocity is set to 0 m/s. The legend shown in (a) applies to all three plots.

Lastly, although the equation for contact force and the friction coefficient come from the same paper as the experimental results, this does not necessarily mean that it is entirely accurate. Whatever error this creates would exist in all cases, though it cannot be said if this error would make the results larger or smaller.

6.5 Force Comparison Conclusions

This chapter compares six different railgun force equations to determine if a more detailed formulation can produce accuracy gains over the the traditional railgun force equation. These equations are compared to three finite element solutions from the literature, and a series of experimental shots from the literature, a finite element solution defined here. A summary of these comparisons is shown in Table 21.

Comparison	S1	S2	F1	F2	F3	F4
ANSYS Maxwell	11.94%	9.21%	-44.66%	-41.17%	-9.84%	-5.87%
Waindok and Piekielny - ANSYS	-10.00%	-12.60%	-55.90%	-52.90%	-23.80%	-19.90%
Waindok and Piekielny - Analytic	-23.70%	-25.90%	-62.60%	-60.00%	-35.30%	-32.10%
Chengxue et al.	-39.09%	-4.59%	-26.01%	-18.64%	-27.20%	-19.67%
Jin et al.	12.46%	59.89%	4.95%	19.57%	6.86%	34.05%
Chen et al. – Case A	43.67%	32.99%	115.45%	127.60%	65.59%	69.49%
Chen et al. – Case B	8.63%	8.82%	48.77%	57.17%	17.49%	19.60%
Total Average	23.48%	24.20%	51.60%	53.31%	28.10%	30.18%

Table 21: Overview of force comparison results. Grey highlights show cases with error over 30%

Overall, these comparisons show that methods F1 and F2 can obtain results that are accurate to an order of magnitude, but nort much more. Methods F3 and F4 are quite accurate in some cases, but produce significant error in others. These methods are accurate to within under 10% of the ANSYS Maxwell 17.2 reslults modeled in this work, and this is the most reliable of the comparisons since there is no room for misinterpretation or uncertainty like in the other cases. Interestingly, method F4 (the method which uses a less accurate B field computation) commonly produces more accurate results than F3, though this is not always true, and in CC3 in particular shows F3 being much more accurate than F4. Thus, since the F3 method is much more computationally expensive than F4, using the F3 method may not be worth the run time. However, a significant issue exists with the F3 and F4 models in that their results are dependent on

the mesh size, and no bound of this effect has been seen. The same grid (and therefore roughtly the same grid element size) is used for the other cases above to retain consistency. Resolving this issue would be the most important objective future work on these models.

Methods S1 and S2, which are simple to apply, have been shown to be surprisingly accurate for the comparisons made, and also get errors of around 10% when compared to the Maxwell model developed in this work. But it is noteable that this accuracy, like for all of the methods, is not consistent across all of the comparison cases. Each method has at least one case where it produces errors significantly larger than the other methods. This could be due to uncertainty in the interpretation of the source articles, unreported differences in the specifics of the source article cases, or some larger more fundamental issue with comparing railgun models or performance.

For the cases compared in this investigation, the extra effort in model development and computation time needed for models F3 and F4 does not produce accuracy benefits over the more readily applied railgun force equation (S1) and the equation from Waindok and Piekielny (S2). However, since this trend does not hold for all cases investigated here, more analysis is needed to produce definitive conclusions. This inconsistency is particularly interesting, and determining consistent trends in literature models and experimental results would be another topic of future work.

Chapter 7: Heating

To complete the exploration of key railgun properties, railgun heating is investigated. Heating is also relevant to the current flow and thus the force definition since it increases electrical resistance. Though these effects are neglected in the force computations presented here, it is helpful to present the heating mechanisms, and heating approximation methods. To do this, a replication of an existing rail heating model is presented.

Again, the full computation of this effect requires the solution of a system of partial differential equations. Solving the system of PDE's is shown below in (74) → (77) allows for the computation of ohmic heating, (temperature rise that results from current flow) (Zhao et al. 2014). Equations (74) → (76) have been presented in the Current Distribution Section, along with a description of the assumptions made in defining them. For convenience, they are replicated here with the equation which allows for temperature computation (77).

(74) $$\boldsymbol{J} = \sigma\left(-\nabla\Upsilon - \frac{\partial \boldsymbol{A}}{\partial \mathrm{t}}\right)$$

(75) $$\sigma\frac{\partial \boldsymbol{A}}{\partial \mathrm{t}} + \frac{1}{\mu_0}[\nabla\times(\nabla\times\mathbf{A})\,] + \sigma\nabla\Upsilon = 0$$

(76) $$\nabla\cdot(\sigma\nabla\Upsilon) = 0$$

(77) $$\rho_d \cdot c_p \cdot \frac{\partial \mathrm{T}}{\partial \mathrm{t}} = \nabla\cdot(k\cdot\nabla T) + \frac{\vec{J}\cdot\vec{J}}{\sigma}$$

The ohmic heating (also called Joule heating) in the rails impacts them most near the breech, and least near the muzzle, since the rails near the breech are heated by the excitation current for the whole duration of the shot, and the muzzle is only heated by this current momentarily.

Ohmic heating is the main source of temperature change in railguns, but it is not the only source, as a significant amount of friction exists between the rail and armature. As described by Indranath Dutta in a study on armature melting and railgun wear, "It was established that Joule-heating, as opposed to friction, is largely responsible for the initiation of armature melting" (Persad and Satapathy 2007). In a comparison between these heating mechanisms done by Jin et. al., it was found that frictional heating accounts for about 10% of the heating in the armature (Jin et al. 2012). The impact of frictional heating on the rails is negligible

because it only applies to a given rail section for a very short period of time (on the order of 10's of μs). The impact on the rails is reduced even further because frictional heating is dependent on velocity, as shown in (78).

(78) $$q_f = \mu \cdot F_C \cdot V$$

This means the parts of the rail which heat the most (near the breech) see significantly less frictional heat than the parts of the rail which heat the least (near the muzzle) because the armature moves much more slowly near the breech than the muzzle. For these reasons, frictional heating in the rails is commonly neglected in the literature (Zhao et al. 2008) (McCorkle and Bahder 2010).

Since ohmic heating is the main cause of temperature rise in railguns, and it is largely dependent on current density, current concentrations result in excessive heating. Common locations of high current concentration can be at the points of actual contact between armature and rail (described in Figure 8), along the armature-rail interface in general (particularly along the rear edge), along the armature rear face, and at the top and bottom corners of the rail inner face for solid rails (since current concentrates along the rail faces for solid rails due to the AC skin effect). For more description of the mechanisms of current concentration see the current distribution section.

The impact of railgun heating can be severe. Heating in metals leads to higher resistance, which reduces current flow and decreases the force applied to the armature. Excessive heating also leads to rail damage, which means rails either need to be replaced (which is expensive and time consuming) or decreased performance due to uneven rail surfaces has to accepted. Uneven rail surfaces exacerbate the issue of current concentration near spot contacts between the rail and armature. Further, they imply that small gaps exist between the rail and armature, which can cause arcing and the creation of high-temperature plasma, which is referred to as "transition" in the literature. Overall, railgun heating serves to reduce railgun efficiency (whether operationally or programmatically).

A 2-D analytic formulation developed by McCorkle and Bahder (79) (McCorkle and Bahder 2010) can be used to obtain an approximate rail temperature profile.

(79) $$T(z,x,t_f) - T_0 = \frac{\mu \cdot m \cdot V^2}{\pi \cdot w^2 \cdot \rho_d \cdot c_p \cdot L' \cdot L} \cdot \Gamma\left(0\ ,\ \frac{\mu \cdot \sigma \cdot V \cdot x'^2}{4 \cdot L \cdot (1 - \sqrt{L \cdot z}}\right)$$

where Γ is the upper incomplete gamma function

This method reflects the affect mentioned above, whereby the rails heat up more near the breech than the muzzle. Because this method assumes solid rails, the rail inner face is shown to heat the most, and this falls off relatively quickly in the z direction. The 2-D nature of this method means that it does not show higher heating at the top and bottom of the rail inner face. Assumptions made in the development of this equation include:

- Current is constant over the time of the shot
- Frictional heating is negligible
- Current density is linearly related to the electric field: $J(z,x,t) = \sigma \cdot E(z,x,t)$
- The current only flows within the AC skin depth of the rail (described in the current distribution section)
- Current density in front of the leading edge of the armature is 0
- The latent heat of melting is neglected
- The armature is arbitrarily thin in the z direction
    - This is a significant assumption, and is expected to have corrections on the order of w_a/L
- The simple railgun force equation is used to solve for the time that the time the armature leaves the muzzle using the fact that the armature starts at $z = 0$ at $t = 0$, and ends at $z = L$ at $t = t_f$
    - $m \cdot \ddot{z} = \frac{L' \cdot I^2}{2} \rightarrow I = \sqrt{\frac{m}{L' \cdot L}}$, $t_f = \frac{2}{I} \cdot \sqrt{\frac{m \cdot L}{L'}}$

The temperature profile described by (79) above is computed, and the results produced by McCorkle and Bahder have been replicated. This analysis is done using the parameters in Table 22.

Physical Parameters	Symbol	Value	Value	Symbol	Material Parameters
Rail Length [m]	L	10	Cu	~	**Rail Material [~]**
Rail Width [m]	w	0.1	8960	ρ_d	**Rail Density [kg / m^3]**
Inductance Gradient [μH/m]	L'	0.46	4 E $^{-8}$	σ	**Rail Conductivity [1 / (Ω·m)]**
Launch Mass [kg]	m	20	1.77 E $^{-8}$	c_p	**Rail Specific Heat [J / (kg·C)]**
Launch Velocity [m/s]	V	3000			

Table 22: Railgun properties used to replicate the results of McCorkle and Bahder (2010)

Results of (79) are shown in Figure 46 and Figure 47. where Figure 46 demonstrates the accurate replication of results from McCorkle and Bahder. This plot shows the melting point of copper being well exceeded, but this does not necessarily imply molten copper will always be present at significant depths for this caliber of railgun since the rail only stays at this temperature for a very brief period of time. This model demonstrates the reduced impact of ohmic heating at the end of the rails, as a steady decrease in maximum temperature change is shown with rail length, and a sharp decrease is shown after 9.5 meters.

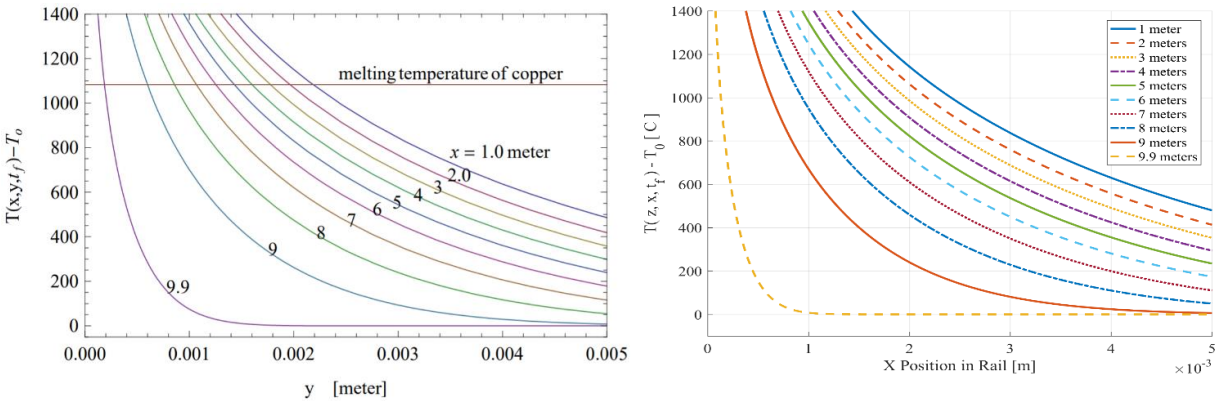

(a) (b)

Figure 46: Temperature profile in a railgun rail (a) as presented by McCorkle and Bahder and (b) as computed here

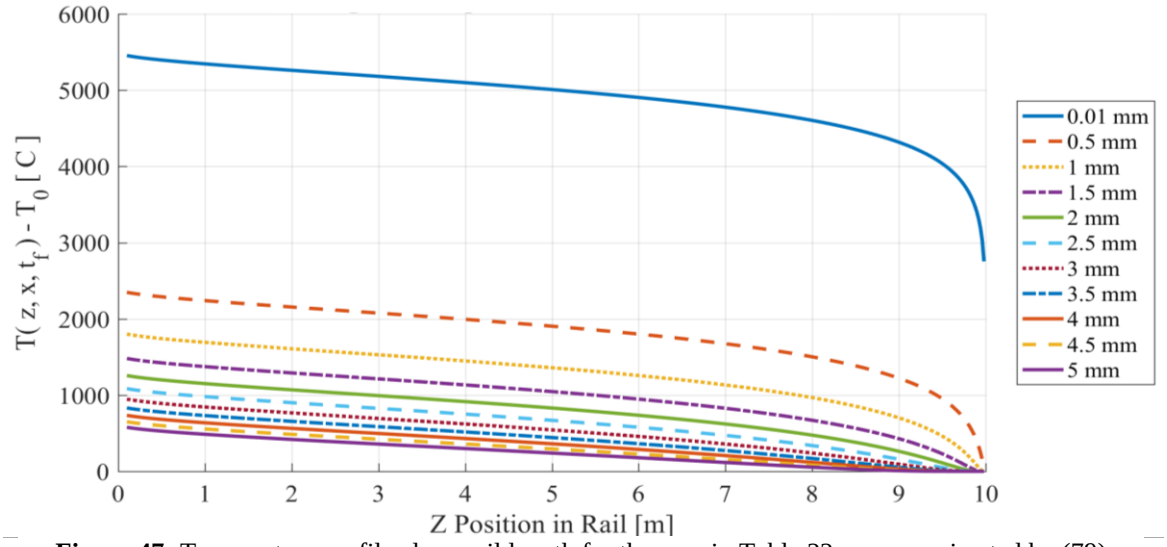

Figure 47: Temperature profile along rail length for the case in Table 22, as approximated by (79)

$$T(z,x,t_f) - T_0 = \frac{\mu \cdot m \cdot V^2}{\pi \cdot w^2 \cdot \rho_d \cdot c_p \cdot L' \cdot L} \cdot \Gamma\left(0\ ,\ \frac{\mu \cdot \sigma \cdot V \cdot x'^2}{4 \cdot L \cdot (1 - \sqrt{L \cdot z}}\right)$$

To find the depth of melted rail material, McCorkle and Bahder also present Equations(80) and (81), which can be used to find the thickness of the melted layer along the rail and inner face and armature rear face respectively.

(80) $$x_{melt\ Rail}(z) = \sqrt{\frac{8 \cdot l}{\mu \cdot \sigma \cdot V}} \cdot e^{-\frac{2 \cdot w^2 \cdot \rho_d \cdot L' \cdot L \cdot c_p \cdot (T_{melt} - T_0)}{\mu \cdot m \cdot V^2}} \cdot \left[1 - \sqrt{\frac{z}{L}}\right]$$

(81) $$z_{melt\ Armature}(0) = \sqrt{\frac{8 \cdot l}{\mu \cdot \sigma \cdot V}} \cdot e^{-\frac{2 \cdot w^2 \cdot \rho_d \cdot L' \cdot L \cdot c_p \cdot (T_{melt} - T_0)}{\mu \cdot m \cdot V^2}}$$

This chapter completes the review of main railgun factors, and successfully replicates the rail heating model presented by McCorkle and Bahder. This model allows for the integration of rail heating into other calculations. Namely, the excitation current profile should have some temperature dependence, and calculations of rail stress and bending (including critical velocity calculations) could account for the weakened rail strength at high temperatures.

Chapter 8: Conclusion

In this work a review of the main factors in railgun operation is presented. The main focus is on the computation of railgun force, and the factors that impact this calculation: current distribution and magnetic field. An effort is made to produce an accurate force calculation which avoids the solution of partial differential equations and the reliance on finite element or finite difference solutions. In doing this, simple railgun geometry is assumed, meaning the rails and armature are rectangular, and the armature is considered to be solid (no brush-contact or plasma armatures are considered).

First, an examination is done of the shape of railgun current profiles, which characterize the railgun input. Then the inductance gradient (L'), a railgun parameter that is key in simplifying analysis, is investigated. A comparison is done of three different methods used to compute L': the Kerrisk method, the Intelligent Estimation Method (IEM), and a regression analysis technique referred to here as the inductance gradient regression method (LRM). It is found that the Kerrisk method and LRM match FEM results over the largest range. The largest shortcoming of these methods is that they all depend on FEM computation being done first, and then determine equations which can compute L' for varying scales of a predetermined geometry.

The distribution of current in the rails and armature is investigated, and the main effects that impact current concentration are explained. It is generally assumed in this analysis that current distribution in the rails is uniform, since this is a reasonably accurate assumption for laminated rails. But a rudimentary method for modeling current distribution in rectangular rails and armatures is presented. The distribution of current in the armature is considered in two of the force computation methods.

The magnetic field is discussed and computed using the Biot-Savart law with two main models. The difference between them is that one assumes the rails are thin wires located along the center of the rail inner face, and the other accounts for the rail thickness. These models are compared to finite element results in both ANSYS Maxwell and the open-source software FEMM. Initial formulations of these models match finite element results well in terms of B field shape, but are reliably about (not exactly) ½ of the finite

element values. After seeing this reliably, a factor of 2 was then applied to the original formulation for the purpose of this analysis.

Six methods of computing railgun force are investigated with the aim of improving performance over the traditional railgun force equation. These are compared to an analytic model, finite element solutions, and experimental results from the literature. These models are also compared to ANSYS Maxwell results obtained by this investigator directly, and two of the models are subjected to a mesh refinement analysis. Overall, reasonably good agreement is seen between the outside sources and these models. Unfortunately, the two most in-depth models suffer from a mesh size dependency, and see increasing values for smaller mesh sizes. The simpler methods (the typical railgun force equation and an equation developed by Waindok and Piekielny) seem to perform surprisingly well compared to the more detailed equations presented here. This suggests that the added complexity is not worth the effort and computational time necessitated by the more detailed methods. However, errors in all of the methods examined are large (over 30%) for at least two comparisons. In fact, where the simple equations perform better than the more detailed analyses on average, the more detailed analyses perform significantly better than the simple ones. This inconsistency merits investigation on its own, but also means the results presented here are not definitive and it remains *possible* that the more detailed analyses are more accurate than the simple methods.

Lastly, to complete a review of the factors which most impact railguns, heating is investigated. This section briefly describes the main sources of railgun heating as ohmic and frictional (with ohmic heating being dominant), the main locations of excessive heating, the dangers of this, and a replication of approximations developed by McCorkle and Bahder which model the heating distribution and melt layer thickness for railguns with solid rails.

This investigation does not solve the partial differential equations necessary to analyze railguns to the highest level of accuracy. The aim is instead to provide an overview and an introduction to the analysis of all the main railgun factors, and present a comparison of railgun force comparison methods in order to inspire and facilitate further investigation in the field.

References

Bayati, M. S., and A. Keshtkar. “Study of the Current Distribution, Magnetic Field, and Inductance Gradient of Rectangular and Circular Railguns.” *IEEE Transactions on Plasma Science*, vol. 41, no. 5, 2013, pp. 1376–1381., doi:10.1109/tps.2013.2251477.

Bayati, M Sajjad, and Kambiz Amiri. “Study of Various C-Shaped Armatures in Electromagnetic Launcher .” *ACES JOURNAL*, vol. 30, no. 9, Sept. 2015.

Bayati, M. Sajjad, et al. “Transition Study of Current Distribution and Maximum Current Density in Railgun by 3-D FEM–IEM.” *IEEE Transactions on Plasma Science*, vol. 39, no. 1, 2011, pp. 13–17., doi:10.1109/tps.2010.2063040.

Behrens Jörg, et al. “Hypersonic and Electromagnetic Railgun Technology as a Future Alternative for the Launch of Suborbital Payloads 16th ESA Symposium on European Rocket and Balloon Programmes and Related Research, St. Gallen, CH, June 2 - 5, 2003.” ESA, *Hypersonic and Electromagnetic Railgun Technology as a Future Alternative for the Launch of Suborbital Payloads 16th ESA Symposium on European Rocket and Balloon Programmes and Related Research, St. Gallen, CH, June 2 - 5, 2003*, 2003.

Brady, James A. “Theoretical Design and Modeling of an Infantry Railgun Projectile.” *Naval Postgraduate School, December*, 2005.

Carey, W.j., et al. “An Electrolytic Capacitor Based Pulse Forming Network For Maximizing Peak Current In A Railgun Simulator.” *Eighth IEEE International Conference on Pulsed Power*, 1989, doi:10.1109/ppc.1991.733397.

Chen, Lixue, et al. “Experimental Study of Armature Melt Wear in Solid Armature Railgun.” *IEEE Transactions on Plasma Science*, vol. 43, no. 5, 2015, pp. 1142–1146., doi:10.1109/tps.2015.2418784.

Chen, Lixue, et al. “The Influence of Mechanical Preload on Muzzle Speed in Solid Armature Railgun.” *2014 17th International Symposium on Electromagnetic Launch Technology*, 2014, doi:10.1109/eml.2014.6920186.

Chengxue, Wang, et al. “Electromagnetic-Thermal Coupled Analysis of the Armature in the Electromagnetic Rail Launcher.” *2014 17th International Symposium on Electromagnetic Launch Technology*, 2014, doi:10.1109/eml.2014.6920628.

Coffo, Mieke. “Contribution to the Modeling, Design, and Experimental Study of an Augmented Railgun and Its Projectile.” *l'Univerite de Franche-Comte et de l'Ecole Royale Militaire*, L'Univerite De Franche-Comte Et De L'Ecole Royale Militaire, 2011.

D'aoust, J., et al. “Development of a Modular Electromagnetic Launcher System for the Air Force Armament Laboratory.” *IEEE Transactions on Magnetics*, vol. 20, no. 2, 1984, pp. 294–297., doi:10.1109/tmag.1984.1063062.

Freeman, Ronald H. “Understanding Space Launch Vehicle Complexity: A Case Study in Combustion Instabilities.” *Procedia Computer Science*, vol. 61, 2015, pp. 307–312., doi:10.1016/j.procs.2015.09.142.

Gao, Liang, et al. “The Modeling and Calculation on an Air-Core Passive Compulsator.” *IEEE Transactions on Plasma Science*, vol. 43, no. 3, 2015, pp. 864–868., doi:10.1109/tps.2015.2394352.

Goldman, E.b., et al. “Development of a Flux Compression Power Unit for Millisecond ETC Pulsed Power Applications.” *IEEE Transactions on Magnetics*, vol. 35, no. 1, 1999, pp. 340–345., doi:10.1109/20.738428.

Gradshteyn, I. S., et al. *Table of Integrals, Series, and Products*. 7th ed., AP, Academic Press/Elsevier, 2015.

Gully, J.h., et al. “Investigation of an Alternator Charged Pulse Forming Network with Flywheel Energy Storage.” *IEEE Transactions on Magnetics*, vol. 29, no. 1, 1993, pp. 969–974., doi:10.1109/20.195710.

Gully, J.h. “Power Supply Technology for Electric Guns.” *IEEE Transactions on Magnetics*, vol. 27, no. 1, 1991, pp. 329–334., doi:10.1109/20.101051.

Gully, J.h. “Power Supply Technology for Electric Guns.” *IEEE Transactions on Magnetics*, vol. 27, no. 1, 1991, pp. 329–334., doi:10.1109/20.101051.

He, Yong, et al. “Efficiency Analysis of an Electromagnetic Railgun With a Full Circuit Model.” *IEEE Transactions on Plasma Science*, vol. 38, no. 12, 2010, pp. 3425–3428., doi:10.1109/tps.2010.2082567.

Hebner, R E, et al. “Some Benefits of Pulsed Alternators as Electromagnetic Gun Power Supplies in Power Systems for Future Electric Ships.” *Engine as a Weapon II, London, UK, December 5-6.*, 2006.

Huerta, M.a., and J.c. Nearing. “Conformal Mapping Calculation of Railgun Skin Inductance.” *IEEE Transactions on Magnetics*, vol. 27, no. 1, 1991, pp. 112–115., doi:10.1109/20.101004.

Hundertmark, Stephan, and Daniel Lancelle. “A Scenario for a Future European Shipboard Railgun.” *IEEE Transactions on Plasma Science*, vol. 43, no. 5, 2015, pp. 1194–1197., doi:10.1109/tps.2015.2403863.

Jayawant, B.v., et al. “Electromagnetic Launch Assistance for Space Vehicles.” *IET Science, Measurement & Technology*, vol. 2, no. 1, Jan. 2008, pp. 42–52., doi:10.1049/iet-smt:20060145.

Jin, Long Wen, et al. “Comparison Simulation of Friction Heat and Joule Heat in Electromagnetic Railgun.” *Applied Mechanics and Materials*, vol. 203, 2012, pp. 401–405., doi:10.4028/www.scientific.net/amm.203.401.

Jin, Longwen, et al. “Electromechanical Performance of Rails With Different Cross-Sectional Shapes in Railgun.” *IEEE Transactions on Plasma Science*, vol. 43, no. 5, 2015, pp. 1220–1224., doi:10.1109/tps.2015.2413892.

Kerrisk, J.f. “Current Diffusion in Rail-Gun Conductors.” Jan. 1982, doi:10.2172/5222337.

Keshtkar, A. “Effect of Rail Dimension on Current Distribution and Inductance Gradient.” *IEEE Transactions on Magnetics*, vol. 41, no. 1, 2005, pp. 383–386., doi:10.1109/tmag.2004.838761.

Keshtkar, Asghar, et al. “Derivation of a Formula for Inductance Gradient Using Intelligent Estimation Method.” *2008 14th Symposium on Electromagnetic Launch Technology*, 2008, doi:10.1109/elt.2008.25.

Keshtkar, Asghar, et al. “Determination of Optimum Rails Dimensions in Railgun by Lagrange's Equations.” *2008 14th Symposium on Electromagnetic Launch Technology*, 2008, doi:10.1109/elt.2008.118.

Kim, Bok-Ki, et al. “A Three-Dimensional Finite Element Model for Thermal Effect of Imperfect Electric Contacts.” *IEEE Transactions on Magnetics*, vol. 35, no. 1, 1999, pp. 170–174., doi:10.1109/20.738397.

Lehmann, P., et al. “Acceleration of a Suborbital Payload Using an Electromagnetic Railgun.” *IEEE Transactions on Magnetics*, vol. 43, no. 1, 2007, pp. 480–485., doi:10.1109/tmag.2006.887666.

Lehmann, P. “Overview of the Electric Launch Activities at the French-German Research Institute of Saint-Louis (ISL).” *IEEE Transactions on Magnetics*, vol. 39, no. 1, 2003, pp. 24–28., doi:10.1109/tmag.2002.805917.

Li, Jun, et al. “Resistance Calculation of the Reusable Linear Magnetic Flux Compressor Coil.” *2004 12th Symposium on Electromagnetic Launch Technology, 2004.*, doi:10.1109/elt.2004.1398125.

Liang, Sizhuang, et al. “Simulation of an Electromagnetic Launcher With a Superconducting Inductive Pulsed Power Supply.” *IEEE Transactions on Applied Superconductivity*, vol. 26, no. 4, 2016, pp. 1–5., doi:10.1109/tasc.2016.2521427.

Liao, Sen-ben, et al. “Chapter 9: Sources of Magnetic Fields.” *Physics 8.02 Electricity and Magnetism at MIT Course Notes*, Massachusetts Institute of Technology, 2004.

Liu, Yi, et al. “Development of a Compact 450-KJ Pulsed-Power-Supply System for Electromagnetic Launcher.” *IEEE Transactions on Plasma Science*, vol. 39, no. 1, 2011, pp. 304–309., doi:10.1109/tps.2010.2050339.

Long, G.c., and W.f. Weldon. “Limits to the Velocity of Solid Armatures in Railguns.” *IEEE Transactions on Magnetics*, vol. 25, no. 1, 1989, pp. 347–352., doi:10.1109/20.22562.

Lou, Yu-Tao, et al. “Research on Proximity Effect of Electromagnetic Railgun.” *Defence Technology*, vol. 12, no. 3, 2016, pp. 223–226., doi:10.1016/j.dt.2016.01.010.

Lv, Qing-Ao, et al. “On Velocity Skin Effect — Part I: Physical Principle Analysis and Equivalent Models Simulation.” *2014 17th International Symposium on Electromagnetic Launch Technology*, 2014, doi:10.1109/eml.2014.6920157.

Marshall, R.a. “Railgunnery: Where Have We Been? Where Are We Going?” *IEEE Transactions on Magnetics*, vol. 37, no. 1, 2001, pp. 440–444., doi:10.1109/20.911872.

McCorkle, William C, and Thomas B Bahder. “Tradeoff between Efficiency and Melting for a High-Performance Electromagnetic Rail Gun.” *ARXIV*, Army Aviation and Missile Research, Development, and Engineering Center, 2010.

Mcfarland, J., and I.r. Mcnab. “A Long-Range Naval Railgun.” *IEEE Transactions on Magnetics*, vol. 39, no. 1, 2003, pp. 289–294., doi:10.1109/tmag.2002.805924.

Mcnab, Ian R. “Large-Scale Pulsed Power Opportunities and Challenges.” *IEEE Transactions on Plasma Science*, vol. 42, no. 5, 2014, pp. 1118–1127., doi:10.1109/tps.2014.2303884.

Mcnab, Ian R. “Progress on Hypervelocity Railgun Research for Launch to Space.” *2008 14th Symposium on Electromagnetic Launch Technology*, 2008, doi:10.1109/elt.2008.65.

Mcnab, Ian R. “Pulsed Power for Electric Guns.” *IEEE Transactions on Magnetics*, vol. 33, no. 1, 1997, pp. 453–460., doi:10.1109/20.560055.

Mcnab, I.r. “Launch to Space with an Electromagnetic Railgun.” *IEEE Transactions on Magnetics*, vol. 39, no. 1, 2003, pp. 295–304., doi:10.1109/tmag.2002.805923.

Meeker, David. “Finite Element Method Magnetics Version 4.2 User's Manual.” 25 Oct. 2015.

Meger, R A, et al. “Electromagnetic Railgun Barrel Damage Experiments.” *IEEE Transactions of Plasma Science*, vol. 41, no. 5, May 2013, pp. 1533–1537., doi:10.1109/TPS.2013.2250314.

Meinel, Carolyn. “For Love of a Gun.” *IEEE Spectrum*, vol. 44, no. 7, 2007, pp. 40–46., doi:10.1109/mspec.2007.376607.

Moghaddam, Asghar Keshtkar Elham Sharifi. “Effects of Shielding on Railgun Inductance Gradient.” *Proceedings. ICCEA 2004. 2004 3rd International Conference on Computational Electromagnetics and Its Applications, 2004.*, doi:10.1109/iccea.2004.1459285.

Murugan, R., and K. Udayakumar. “Effect of Rail Dimensions on Rail Gun Design Parameters.” *2005 Annual IEEE India Conference - Indicon*, doi:10.1109/indcon.2005.1590247.

Murugan, R, et al. “ESTIMATION OF INDUCTANCE GRADIENT EMPIRICAL FORMULA OF RAILS USING REGRESSION ANALYSIS TECHNIQUE.” *International Journal of Advanced Engineering Technology*, vol. 7, no. 1, 2016.

Nearing, J.c., and M.a. Huerta. “Skin and Heating Effects of Railgun Current.” *IEEE Transactions on Magnetics*, vol. 25, no. 1, 1989, pp. 381–386., doi:10.1109/20.22568.

Nearing, J.c., and M.a. Huerta. “Skin and Heating Effects of Railgun Current.” *IEEE Transactions on Magnetics*, vol. 25, no. 1, 1989, pp. 381–386., doi:10.1109/20.22568.

Pagnetti, Alberto, et al. “Evaluation of the Impact of Proximity Effect in the Calculation of the Internal Impedance of Cylindrical Conductors.” *2011 XXXth URSI General Assembly and Scientific Symposium*, 2011, doi:10.1109/ursigass.2011.6050734.

Poniaev, S.a., et al. “Laboratory Modelling of an Active Space Experiment Using Railgun as a Launch Device.” *Acta Astronautica*, vol. 135, 2017, pp. 63–68., doi:10.1016/j.actaastro.2016.10.014.

Pratap, S., et al. “A Compulsator Driven Rapid-Fire EM Gun.” *IEEE Transactions on Magnetics*, vol. 20, no. 2, 1984, pp. 211–214., doi:10.1109/tmag.1984.1063056.

Pratap, S.b., and M.d. Driga. “Compensation in Pulsed Alternators.” *IEEE Transactions on Magnetics*, vol. 35, no. 1, 1999, pp. 372–377., doi:10.1109/20.738434.

Rice, Eric E, et al. *PRELIMINARY FEASIBILITY ASSESSMENT FOR EARTH-TO-SPACE ELECTROMAGNETIC (RAILGUN) LAUNCHER*. United States, 1982, *PRELIMINARY FEASIBILITY ASSESSMENT FOR EARTH-TO-SPACE ELECTROMAGNETIC (RAILGUN) LAUNCHER*.

Satapathy, S., and C. Persad. “Friction and Wear Sciences for a Highly Durable Railgun Weapon.” *Institute for Advanced Technology - The University of Texas at Austin*, Oct. 2007, doi:10.21236/ada474864.

Schneider, M., et al. “The ISL Rapid Fire Railgun Project RAFIRA Part I: Technical Aspects and Design Considerations.” *IEEE Transactions on Magnetics*, vol. 45, no. 1, 2009, pp. 442–447., doi:10.1109/tmag.2008.2008468.

Schneider, M., et al. “The ISL Rapid Fire Railgun Project RAFIRA—Part II: First Results.” *IEEE Transactions on Magnetics*, vol. 45, no. 1, 2009, pp. 448–452., doi:10.1109/tmag.2008.2008533.

Sitzman, A., et al. “Design, Construction, and Testing of an Inductive Pulsed-Power Supply for a Small Railgun.” *IEEE Transactions on Magnetics* , vol. 43, no. 1, Jan. 2006, pp. 270–274., doi:10.21236/ada476726.

Spahn, E., and G. Buderer. “A Flexible Pulse Power Supply for EM- and ETC-Launchers.” *Digest of Technical Papers. 12th IEEE International Pulsed Power Conference. (Cat. No.99CH36358)*, 1999, doi:10.1109/ppc.1999.823778.

Stefani, Francis, et al. “Experiments With Armature Contact Claddings.” *IEEE Transactions on Magnetics*, vol. 43, no. 1, 2007, pp. 413–417., doi:10.1109/tmag.2006.887445.

Thomas, E. G., and Arthur J. Meadows. *Maxwell's Equations and Their Applications*. Adam Hilger Ltd., Bristol and Boston, 1985.

Turman, B. N., and R. J. Lipinski. “Electromagnetic Coilgun Launcher for Space Applications.” *AIP Conference Proceedings*, 1996, doi:10.1063/1.49932.

“U.S. Navy Efforts towards Development of Future Naval Weapons and Integration into an All Electric Warship (AEW).” The Electric Ships Office, 2011, mstcws.com/jlha/Publications/HerrenWhitePaper-AllElectricWarshipWeaponIntegration.pdf.

Waindok, Andrzej. “Calculation Models of the Electrodynamic Accelerator (Railgun).” *PrzeglÄ…d Elektrotechniczny*, vol. 1, no. 9, May 2016, pp. 248–251., doi:10.15199/48.2016.09.60.

Walls, W.a., et al. “Pulsed Rotating Machine Power Supplies for Electro-Thermal-Chemical Guns.” *IEEE Transactions on Magnetics*, vol. 33, no. 1, 1997, pp. 519–523., doi:10.1109/20.560066.

Watt, Trevor James. “The Onset of Gouging in High-Speed Sliding Contacts.” *The University of Texas at Austin*, 2011.

Xing, Yan-Chang, et al. “Analysis of Transient Current Distribution in Copper Strips of Different Structures for Electromagnetic Railgun.” *IEEE Transactions on Plasma Science*, vol. 43, no. 5, 2015, pp. 1566–1571., doi:10.1109/tps.2015.2414095.

Xu, Lizhong, and Yanbo Geng. “Forces of Rails for Electromagnetic Railguns.” *Applied Mathematical Modelling*, vol. 36, no. 4, 2012, pp. 1465–1476., doi:10.1016/j.apm.2011.09.036.

Xu, R., et al. “Effect of Geometrical Parameters on Inductance Gradient of Multiple Electromagnetic Railguns.” *2014 17th International Symposium on Electromagnetic Launch Technology*, 2014, doi:10.1109/eml.2014.6920623.

Ying, Wang, et al. “A Pulsed MHD Generator for Electric Launcher.” *2004 12th Symposium on Electromagnetic Launch Technology, 2004.*, doi:10.1109/elt.2004.1398086.

Zhang, Ya-Dong, et al. “Ablation and Geometry Change Study of Solid Armature in a Railgun.” *Chinese Physics B*, vol. 22, no. 8, 2013, p. 084102., doi:10.1088/1674-1056/22/8/084102.

Zhao, H, et al. “THERMAL MODEL FOR ELECTROMAGNETIC LAUNCHERS.” *Engenharia Térmica (Thermal Engineering)*, vol. 7, no. 2, Dec. 2008, pp. 59–64.

Zhao, Han, et al. “Three-Dimensional Launch Simulation and Active Cooling Analysis of a Single-Shot Electromagnetic Railgun.” *Simulation*, vol. 90, no. 12, 2014, pp. 1312–1327., doi:10.1177/0037549714553812.

Zuo, Peng, et al. “Characteristics of Current Distribution in Rails and Armature With Different Section Shape Rails.” *IEEE Xplore Document*, IEEE, May 2013, ieeexplore.ieee.org/lpdocs/epic03/wrapper.htm?arnumber=6488872.

Appendix

Appendix A: Inductance Gradient Tables

Rectangular Rails - Computed via FEA Simulation:

h(cm)	w = 1cm		w = 1.5cm		w = 2cm	
	L'	J_{max}	L'	J_{max}	L'	J_{max}
0.8	0.65757	54.480	0.64606	49.078	0.61017	45.673
1	0.65307	50.313	0.60882	45.637	0.57707	42.723
1.2	0.61460	46.977	0.57590	42.924	0.54804	40.316
1.4	0.58094	44.184	0.54681	40.601	0.52198	38.280
1.5	0.56570	42.947	0.53351	39.552	0.50993	37.355
1.6	0.55121	41.774	0.52079	38.566	0.49850	36.482
1.8	0.52453	39.662	0.49731	36.774	0.47722	34.881
2	0.50059	37.798	0.47601	35.164	0.45779	33.428
2.2	0.47886	36.119	0.45654	33.695	0.44000	32.117
2.5	0.44974	33.875	0.43037	31.747	0.41584	30.341

Figure 48: L' and Maximum Current Density (J_{max}) as Simulated by Keshtkar et al. (2009) with rail separation (s) of 2 cm

h=s=3.03 cm		w=s=3.03 cm		w=h=3.03 cm	
w (cm)	L' (μH/m)	h (cm)	L' (μH/m)	s (cm)	L' (μH/m)
3.03	0.45174	3.03	0.45174	3.03	0.54174
2.92	0.45437	2.85	0.46527	2.80	0.43374
2.80	0.45703	2.64	0.47950	2.57	0.41459
2.68	0.4598	2.42	0.49457	2.33	0.39420
2.57	0.4626	2.21	0.51058	2.10	0.37238
2.45	0.4656	2.00	0.52747	1.87	0.34893
2.33	0.4687	1.77	0.54676	1.63	0.32356
2.22	0.4719	1.56	0.56770	1.40	0.29589
2.10	0.4753	1.33	0.59060	1.17	0.26542
1.98	0.4789	1.11	0.61579	0.93	0.23144
1.87	0.4824	0.89	0.64381	0.70	0.19289
1.75	0.4863	0.67	0.67542	0.47	0.14810
1.63	0.4903	0.44	0.71212	0.23	0.09407
1.52	0.4946	0.11	0.75429		
1.40	0.4991				
1.28	0.5039				
1.17	0.5091				
1.05	0.5146				
0.93	0.5205				
0.82	0.5269				
0.70	0.5339				
0.58	0.5416				
0.47	0.5504				
0.35	0.5608				

Figure 49: L' as Simulated by Asghar Keshtkar (2005)

Sl.No.	S/H	W/H									
		0.1	0.2	0.3	0.4	0.5	0.6	0.7	0.8	0.9	1
1	1	0.558	0.5364	0.5194	0.5053	0.4933	0.4828	0.4736	0.4653	0.4585	0.4519
2	0.9	0.526	0.5057	0.4898	0.4766	0.4653	0.4554	0.4468	0.439	0.432	0.4251
3	0.8	0.491	0.4725	0.4577	0.4454	0.4349	0.4285	0.4177	0.4105	0.4041	0.3982
4	0.7	0.453	0.4364	0.4227	0.4114	0.4028	0.3934	0.3861	0.3795	0.3736	0.3682
5	0.6	0.413	0.3966	0.3843	0.3741	0.3643	0.357	0.3525	0.3453	0.3404	0.3352
6	0.5	0.366	0.3525	0.3416	0.3326	0.325	0.3184	0.3125	0.3074	0.3027	0.2985
7	0.4	0.315	0.3029	0.2937	0.286	0.2795	0.2739	0.269	0.2646	0.2607	0.2571
8	0.3	0.256	0.2463	0.2389	0.2328	0.2276	0.2231	0.2191	0.2157	0.2125	0.2097
9	0.2	0.187	0.1804	0.1751	0.1707	0.1669	0.1637	0.1609	0.1584	0.1562	0.1542
10	0.1	0.105	0.1015	0.0985	0.0961	0.0941	0.0923	0.0908	0.0894	0.0882	0.0871

Figure 50: L' as Simulated by Murugan et al. (2016)

Rectangular Rails - Computed with Simplified Equations:

	Inductance in μH/m					
	w/h					
s/h	0.1	0.5	1.0	3.0	6.0	10.0
0.08	0.08490	0.08176	0.08025	0.07741	0.07555	0.07416
0.1	0.10312	0.09863	0.09641	0.09235	0.08973	0.08779
0.2	0.18336	0.17097	0.16446	0.15327	0.14629	0.14131
0.5	0.36063	0.32456	0.30414	0.27006	0.24975	0.23589
1.0	0.55530	0.49073	0.45174	0.38601	0.34754	0.32199
1.5	0.68986	0.60697	0.55482	0.46513	0.41249	0.37786
3.0	0.94249	0.83183	0.75716	0.62161	0.53951	0.48549
5.0	1.13865	1.01296	0.92432	0.75573	0.64932	0.57818
7.5	1.29725	1.16299	1.06564	0.87383	0.74807	0.66221
10.0	1.41068	1.27183	1.16958	0.96355	0.82472	0.72823
12.0	1.48283	1.34161	1.23675	1.02276	0.87612	0.77297

Figure 51: L' as Computed with the Kerrisk Method (Kerrisk 1982)

	s/h					
	0.20	0.40	0.60	0.80	1.00	1.20
w/h						
0.10	.184	.308	.408	.488	.556	.916
0.50	.172	.280	.364	.432	.492	.540
1.20	.164	.260	.332	.384	.440	.484

Figure 52: L' as Computed with Conformal Mapping by Huerta and Nearing (1991)

Circular Rails – Computed via FEA Simulation:

S. No	T/S	S							
		10cm	9cm	8cm	7cm	6cm	5cm	4cm	3cm
1	1	0.3167	0.3205	0.3235	0.3271	0.3302	0.334	0.338	0.3442
2	0.9	0.3271	0.3304	0.3332	0.3368	0.34	0.3437	0.3481	0.3539
3	0.8	0.3384	0.3416	0.3444	0.348	0.351	0.3546	0.3591	0.3675
4	0.7	0.3516	0.3544	0.3574	0.3606	0.3638	0.3673	0.3718	0.378
5	0.6	0.3662	0.3693	0.3719	0.3759	0.3782	0.3818	0.3865	0.3932
6	0.5	0.3837	0.3861	0.389	0.3921	0.3953	0.399	0.404	0.4413
7	0.4	0.4044	0.4074	0.4099	0.4128	0.4162	0.4201	0.4253	0.4332
8	0.3	0.4309	0.4335	0.4361	0.4388	0.4425	0.4466	0.4522	0.4608
9	0.2	0.4648	0.467	0.4697	0.4728	0.4768	0.4814	0.4888	0.4976
10	0.1	0.5119	0.5147	0.517	0.5214	0.5251	0.5299	0.5353	0.5433

Figure 53: L' as Simulated by Murugan et al. (2016) for rails with an opening angle (θ) = 40°

S. No	T/S	S							
		10cm	9cm	8cm	7cm	6cm	5cm	4cm	3cm
1	1	0.1236	0.1249	0.1264	0.1277	0.1291	0.1314	0.1349	0.1399
2	0.9	0.1292	0.1304	0.1318	0.1329	0.1347	0.1371	0.1407	0.1459
3	0.8	0.1354	0.1367	0.1379	0.1396	0.1413	0.1437	0.1473	0.153
4	0.7	0.1428	0.1441	0.1455	0.147	0.1489	0.1516	0.1553	0.1613
5	0.6	0.1516	0.1528	0.1542	0.1559	0.1578	0.1609	0.1649	0.1714
6	0.5	0.1624	0.1636	0.1648	0.1671	0.1692	0.1725	0.1769	0.184
7	0.4	0.1758	0.1775	0.1793	0.1811	0.1838	0.1871	0.1919	0.1999
8	0.3	0.1943	0.1961	0.1979	0.2002	0.2029	0.2067	0.2122	0.2212
9	0.2	0.2203	0.2219	0.224	0.2266	0.2298	0.2341	0.2406	0.2507
10	0.1	0.2594	0.2615	0.264	0.267	0.2707	0.2754	0.2818	0.2916

Figure 54: L' as Simulated by Murugan et al. (2016) for rails with an opening angle (θ) = 10°

θ	d(cm)	R_i(cm)	R_o(cm)	$L'(\mu$H/m)
150°	1.0	0.210	2.63	0.2522
	0.9	0.442	2.66	0.2560
	0.8	0.592	2.68	0.2500
	0.6	0.814	2.75	0.2357
	0.4	1.000	2.81	0.2204
	0.2	1.160	2.87	0.2000
180°	1.8	0.314	2.41	0.2845
	1.2	0.948	2.57	0.2233
	0.9	1.158	2.66	0.1897
	0.6	1.347	2.75	0.1517

θ	d(cm)	R_i(cm)	R_o(cm)	$L'(\mu$H/m)
135°	1.7	0.6144	1.71	0.4834
	1.4	0.7986	1.7986	0.4545
	1.2	0.9085	1.8363	0.4347
	1	1.0124	1.8898	0.4147
	0.8	0.8	1.945	0.3944
	0.6	0.6	2.0317	0.3756
120°	1.6	0.3785	1.7344	0.4920
	1.2	0.7121	1.84	0.4672
	1	0.8407	1.8898	0.4432
	0.8	0.9587	1.9452	0.4254
	0.4	1.1768	2.0615	0.3874

Figure 55: L' as Simulated by Bayati and Keshtkar (2013) where d is equivalent to the "s" shown in Figure 30, R_i is the rail inner radius, and R_o is the rail outer radius

Appendix B: Inductance Gradient Result Replication

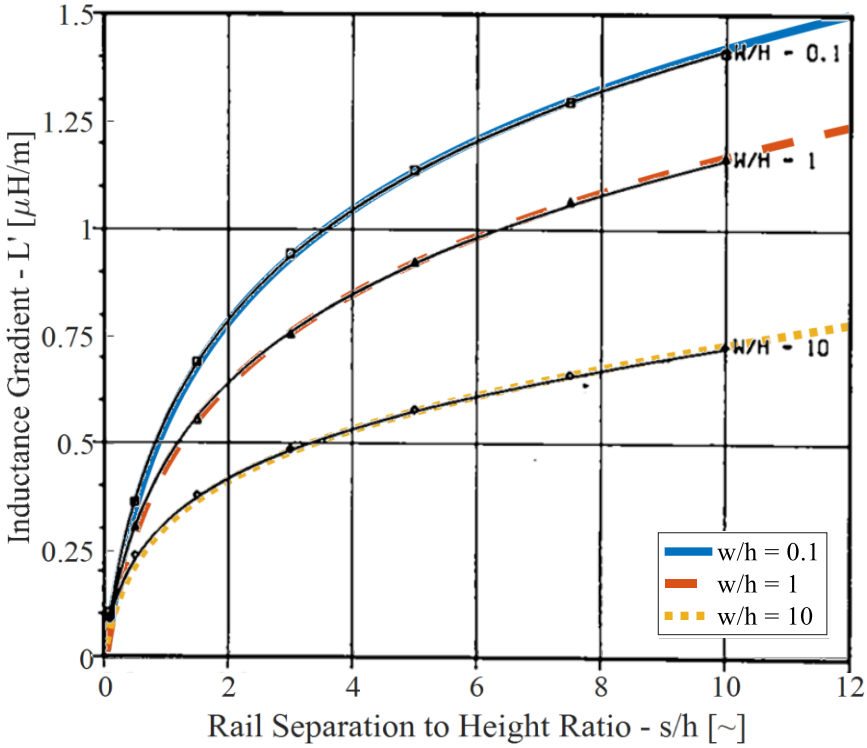

Figure 56: Replication of Figure 9 by Kerrisk (1982) where the black lines are the results produced by Kerrisk

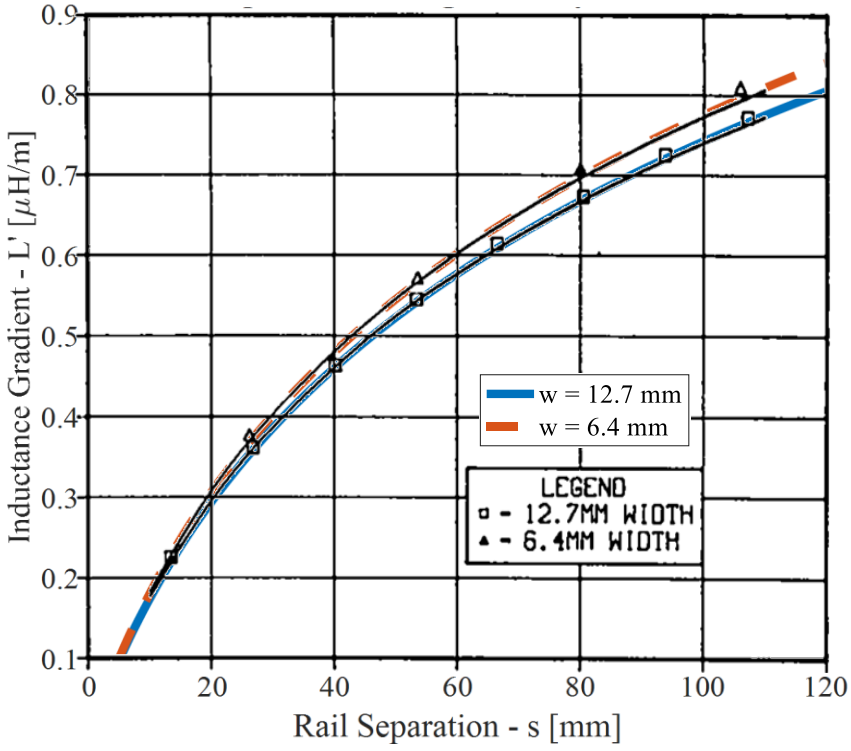

Figure 57: Replication of Figure 10 by Kerrisk (1982) where the black lines are the results produced by Kerrisk

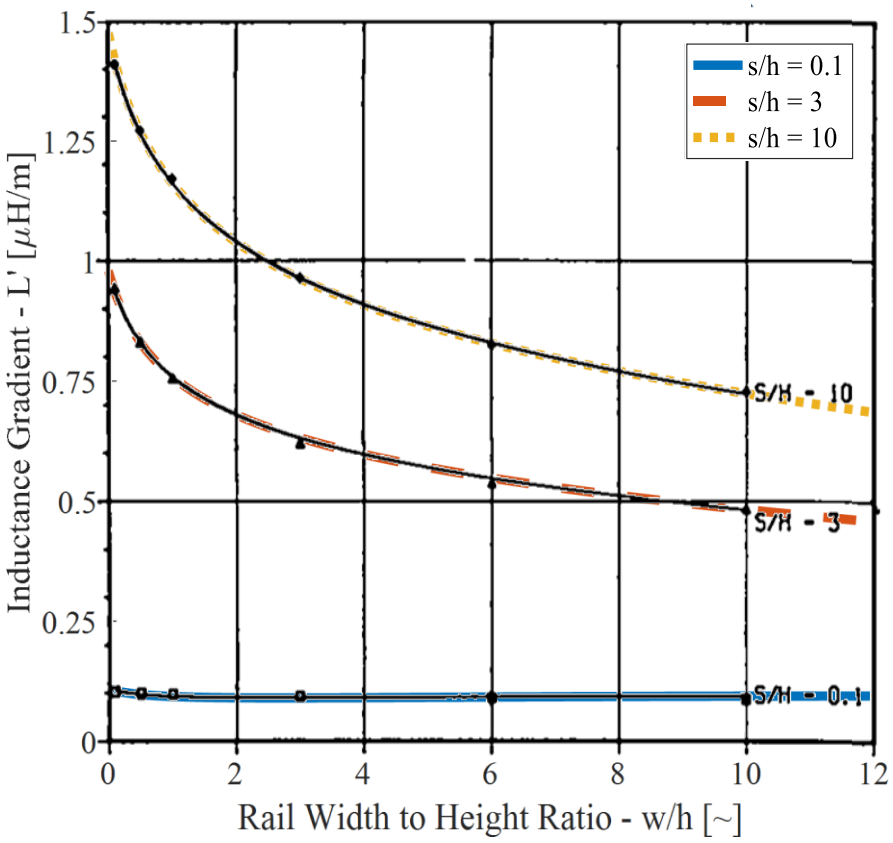

Figure 58: Replication of Figure 12 by Kerrisk (1982) where the black lines are the results produced by Kerrisk

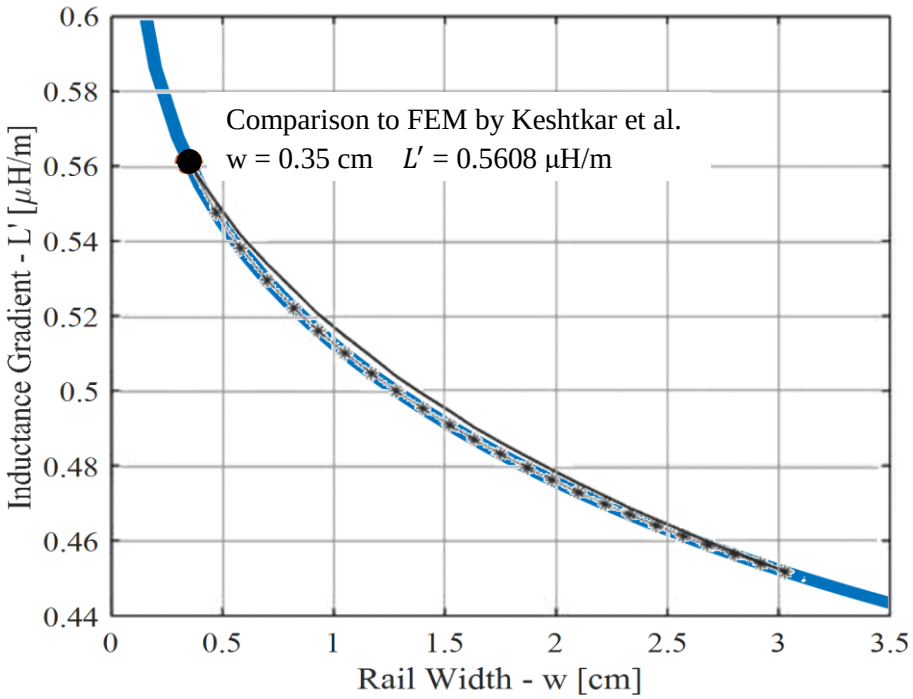

Figure 59: Replication of Figure 5 by Keshtkar, Bayati, and Keshtkar (2009) where the solid line is the FEM result and starred line is the IEM result produced by Keshtkar, Bayati, and Keshtkar for s = h = 3.03 cm

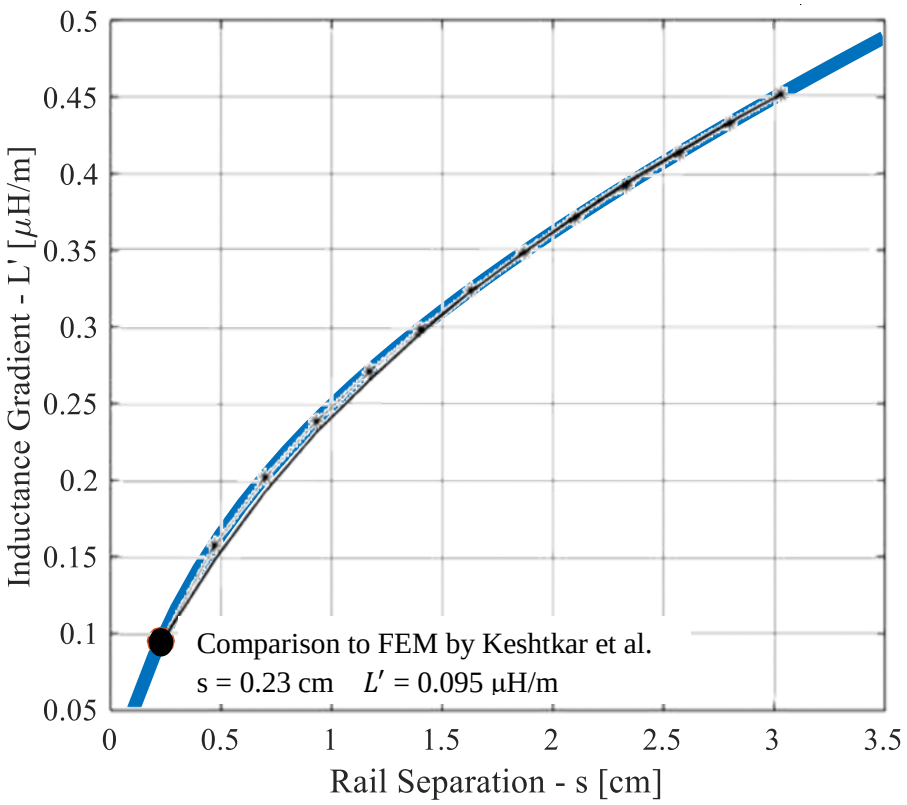

Figure 60: Replication of Figure 6 by Keshtkar, Bayati, and Keshtkar (2009) where the solid line is the FEM result and starred line is the IEM result produced by Keshtkar, Bayati, and Keshtkar for w = h = 3.03 cm

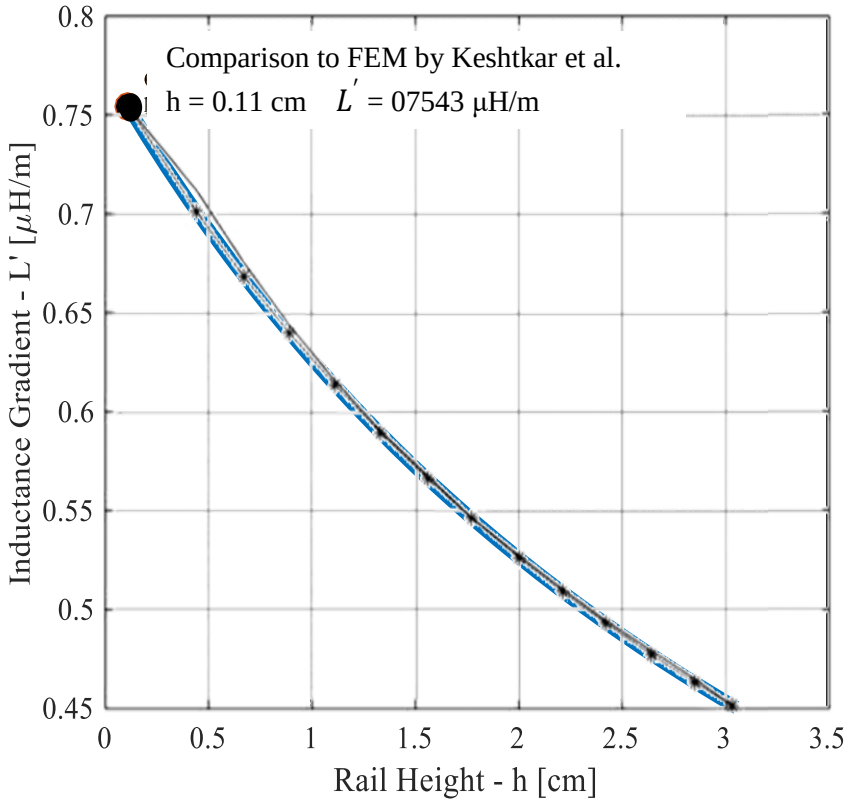

Figure 61: Replication of Figure 7 by Keshtkar, Bayati, and Keshtkar (2009) where the solid line is the FEM result and starred line is the IEM result produced by Keshtkar, Bayati, and Keshtkar for s = w = 3.03 cm